Practical Limitations of Low Mean Transverse Energy Metallic Photocathodes

by

Christopher John Knill

A Dissertation Presented in Partial Fulfillment
of the Requirement for the Degree
Doctor of Philosophy

Approved April 2023 by the
Graduate Supervisory Committee:

Siddharth Karkare, Chair
Jeffery Drucker
Robert Kaindl
Samuel Teitelbaum

ARIZONA STATE UNIVERSITY

May 2023

ABSTRACT

The performance of accelerator applications like X-ray free electron lasers (XFELs) and ultrafast electron diffraction (UED) and microscopy (UEM) experiments is limited by the brightness of electron beams generated by photoinjectors. In order to maximize the brightness of an electron beam it is essential that electrons are emitted from photocathodes with the smallest possible mean transverse energy (MTE). Metallic photocathodes hold the record for the smallest MTE ever measured at 5 meV from a Cu(100) single crystal photocathode operated near the photoemission threshold and cooled to 30 K. However such photocathodes have two major limitations: poor surface stability, and a low quantum efficiency (QE) which leads to MTE degrading non-linear photoemission effects when extracting large charge densities. This thesis investigates the efficacy of using a graphene protective layer in order to improve the stability of a Cu(110) single crystalline surface. The contribution to MTE from non-linear photoemission effects is measured from a Cu(110) single crystal photocathode at a variety of excess energies, laser fluences, and laser pulse lengths. To conclude this thesis, the design and research capabilities of the Photocathode and Bright Beams Lab (PBBL) are presented. Such a lab is required to develop cathode technology to mitigate the practical limitations of metallic photocathodes.

DEDICATION

To my loving fiancée Katie, my son Chris, and my baby daughter Madeleine

ACKNOWLEDGEMENTS

First and foremost I would like to thank my advisor Siddharth Karkare. I am truly grateful for the guidance and support you provided me with during the seemingly endless trials and tribulations that arose during my time at ASU. I would also like to thank the Center for Bright Beams and in particular those who have been a part of theme 1 over the last 5 years. The knowledge and advice that I have gained from attending theme 1 meetings has been invaluable to my growth during my PhD, and it is something that I will always be grateful for. I would like to thank my collaborators Hisato Yamaguchi and Nathan Moody. I would also like to thank my PhD supervisory committee Jeff Drucker, Robert Kaindl, and Sam Teitelbaum for your inputs during my PhD.

I am grateful to my fellow students at ASU who helped make my graduate studies significantly more successful and enjoyable. In particular I would like to thank the post-docs, grad students, and undergrads that I have had the pleasure of working with in the PBBL. To my fellow grad students Billy, Sam, Sean, and Shep we had some great times from camping in a blizzard on Mingus mountain, to soul-crushing hikes into the Grand Canyon. Thank you for always being open to an adventure, it made the endless stream of grad school stress infinitely more manageable.

I owe the biggest debt of gratitude to my family. To my brothers Michael and Cory, I think back to all the times you both have been there to support and encourage me, and I am just filled with immense gratitude. As Cory put it, I am especially grateful for the constant arguments we had growing up which provided us with the strong foundation needed to achieve success and nothing less. To my Mom, Anna Knill, and my Dad, Kevin Knill, you without doubt deserve the biggest thanks of all. You always believed in me and supported me no matter how crazy my dreams were. If I can amend a quote from Sir Isaac Newton, "If I have achieved so much it is by

standing on the shoulders of Giants". Thank you for being the Giants in my life. This PhD would not have been possible without you.

To my fiancée Katie, my son Chris, and my baby daughter on the way Madeleine, I would not have been able to finish my PhD without your constant love and support. This dissertation is dedicated to you.

Finally, I would like to acknowledge the funding support from the U.S. National Science Foundation, the Center for Bright Beams, and the Department of Energy.

TABLE OF CONTENTS

CHAPTER Page

CHAPTER Page

LIST OF TABLES

Table Page

LIST OF FIGURES

Figure Page

Figure Page

Figure Page

Figure Page

Figure Page

Chapter 1

INTRODUCTION

1.1 Photocathodes

Photocathodes are materials that use the photoelectric effect to generate electrons from incident light. In linear accelerators the photocathode is placed in a chamber (called photoinjectors) with a high DC or RF electric field. Illuminating the photocathode with a pulsed laser generates electron bunches which are then accelerated by the electric field to create an electron beam.

Electron beams are used in a variety of linear accelerator applications like X-ray free electron lasers (XFELs) and ultrafast electron diffraction (UED) and microscopy (UEM) experiments. The performance of these applications is directly limited by the brightness of the electron beam. The brightness of an electron beam is a quantity that characterizes the phase space density of the beam and is represented by:

$$B_{6D} \propto \frac{N}{\epsilon_x \epsilon_y \epsilon_z} \tag{1.1}$$

where N is the number of electrons which can range from 1 to 10^{10} depending on the application, and ϵ_i for $i = x, y, z$ is a quantity known as the emittance and it describes the RMS area in the x-, y-, and z- phase space planes. For linear accelerators the electron beam undergoes incompressible flow due to Liouville's theorem which states for a Hamiltonian system the phase space density remains constant. Hence, the maximum brightness of the electron beam occurs at the photocathode. Therefore, maximizing the beam brightness from the photocathode is essential to generating the highest quality electron beam.

For high peak charge density applications like XFELs and single-shot UED, the maximum beam brightness scales according to the following relation:

$$B \propto \frac{E^n}{\text{MTE}} \tag{1.2}$$

where E is the accelerating electric field, n is a real number between 1 and 2 where the value depends on the design of the photoinjector, and MTE is the mean transverse energy of the electrons emitted from the photocathode. For low charge density applications like stroboscopic UED, the brightness is inversely proportional to the MTE as well as the emission area on the cathode (Musumeci *et al.* (2018)). The MTE can be related to the intrinsic emittance (ϵ_x) from the photocathode as:

$$\epsilon_x = \sigma_x \sqrt{\frac{\text{MTE}}{m_e c^2}} \tag{1.3}$$

where σ_x is the RMS emission area, m_e is the mass of the electron, and c is the speed of light. From Eq. 1.2 and Eq. 1.3 the critical figure of merit in increasing the brightness for linear electron accelerators is the MTE and it is equivalent to the temperature of the electrons in vacuum (Bazarov *et al.* (2009)). Hence great efforts have gone into understanding and minimizing the MTE in order to maximize the brightness of electron beams. In general the MTE is limited by operating parameters like the irradiating excess energy (Dowell and Schmerge (2009)), the temperature of the photocathode (Cultrera *et al.* (2015); Feng *et al.* (2015)), and the laser pulse energy (Bae *et al.* (2018); Maxson *et al.* (2017)), as well as photocathode properties like surface nonuniformities (Karkare and Bazarov (2015); Feng *et al.* (2017)) and the band structure (Karkare *et al.* (2017)).

Excess energy is defined as the difference between the photon energy and the work function. Typically a fraction of the excess energy is converted into the transverse energy during emission. Using Spicer's 3-step model, Dowell and Schmerge (Dowell

and Schmerge (2009)) first explained the relationship between MTE and excess energy by the following equation:

$$\text{MTE} = \frac{E_{excess}}{3} \tag{1.4}$$

where E_{excess} is the excess energy. However this model was based on several unrealistic assumptions like a constant density of states at zero temperature and the conservation of transverse momentum, which does not hold for disordered surfaces. Recently Saha *et al* proposed a simpler explanation of the relationship between MTE and excess energy (Saha *et al.* (2023a)). Assuming that the electrons are uniformly distributed into the free electron parabola and that upon excitation they do not scatter before emission, the MTE is given by Eq. 1.4. For low or negative excess energies the electron emission occurs from the tail of the Fermi distribution and the MTE approaches the thermal limit of k_BT where k_B is the Boltzmann constant and T is the temperature of the electron distribution. For small laser fluences the temperature of the electron distribution is in thermal equilibrium with the lattice, and therefore the temperature T is the temperature of the photocathode. At room temperature the thermal limit is 25 meV, a result that has been demonstrated experimentally from Sb thin films (Feng *et al.* (2017)) and Cu single crystals (Karkare *et al.* (2020); Knill *et al.* (2023)).

By cooling down the photocathode to cryogenic temperatures, sub-25 meV MTEs have been demonstrated from several systems like 22 meV from thin films of alkali-antimonide at 90 K (Cultrera *et al.* (2015)), 5 meV from a Cu(100) single crystal at 30 K (Karkare *et al.* (2020)), and 9 meV from a graphene-coated Cu(110) single crystal at 77 K (Knill *et al.* (2023)). However at cryogenic temperatures it becomes increasingly difficult to reach the thermal limit. One factor that increases the MTE above the thermal limit is the surface non-uniformities of physical and chemical roughness (Karkare and Bazarov (2015); Feng *et al.* (2017)). These non-uniformities lead to localized transverse electric fields that can increase the MTE by several factors. To

minimize the contribution to MTE from surface non-uniformities, it is critical that electrons are emitted from atomically ordered single crystalline surfaces (Karkare *et al.* (2017)). For single crystalline surfaces the transverse momentum is conserved during photoemission. Hence by selecting photocathode materials that allow photoemission from low transverse energy states the MTE can be reduced. By minimizing the effects of excess energy and by emitting from a small transverse momentum state, a record low MTE of 5 meV was demonstrated from an atomically pristine Cu(100) single crystal when operated near zero excess energy and cooled down to 30 K (Karkare *et al.* (2020)). Space charge effects can degrade the brightness set by the photocathode. However the maximum brightness in a photoinjector is inversely proportional to the MTE as shown in Eq. 1.2 (Bazarov *et al.* (2009)). Although this 5 meV MTE is significantly lower than the 100 - 500 meV MTEs that are typically found in modern photoinjectors, it comes with two main drawbacks which prevents its widespread use: poor surface stability, and low quantum efficiency (QE) which can lead to non-linear photoemission effects.

1.2 Photocathode Stability

In order to operate in photoinjectors, single crystalline metallic photocathodes need to be able to maintain their low MTE for long periods of time. Photoemission is a surface sensitive process so any damage to the surface will affect the MTE. In a photoinjector the photocathode is subjected to high electric fields and high laser fluence conditions. Operating in such conditions can lead to surface degradation from various mechanisms like chemical poisoning from residual gas (Chanlek *et al.* (2014)), laser heating (Anisimov *et al.* (1974)), and ion back-bombardment (Aulenbacher (2011)).

Recent investigations have looked at the efficacy of capping photocathode surfaces with a thin film to improve their stability under vacuum conditions without

negatively impacting their photoemission properties. One such investigation showed that capping a Cu(110) single crystal with a monolayer of graphene can significantly improve the stability of the cathode surface and preserve the quantum efficiency (QE) at atmospheric conditions (Liu *et al.* (2017)). Another investigation showed that a graphene coated Cu(110) single crystal can achieve MTEs right at the thermal limit for room temperature, and in the sub-10 meV range for cryogenic temperatures (Knill *et al.* (2023)). In addition the MTE was shown to be stable near the thermal limit for 7 days indicating that it improved the stability of the MTE (Knill *et al.* (2022)).

1.3 Non-linear Photoemission

Quantum efficiency is a material property that is equal to the ratio of the number of emitted electrons per number of incident photons on the photocathode surface. Low-MTE Cu single crystals have an extremely low QE of 10^{-7} at room temperature (Dowell *et al.* (2010)) and as low as 10^{-9} at liquid nitrogen temperatures (Ch. 2) when operating near threshold. In order to extract high charge densities from these low QE photocathodes, a very a high laser fluence >10 mJ/cm^2 is required at room temperature which is on the order of the damage threshold of Cu (10s of mJ/cm^2. At these high laser fluences, the non-linear photoemission effects of multi-photon emission and electron heating begin to dominate the photoemission process and limit the minimum achievable MTE (Maxson *et al.* (2017); Bae *et al.* (2018)).

Multi-photon emission occurs when an electron absorbs more than one photon in order to emit into vacuum and it can be categorized into two regimes: below threshold multi-photon emission and above threshold multi-photon emission. Below threshold multi-photon emission occurs at negative excess energies, and therefore the electron needs to absorb at least two photons in order to have sufficient energy to overcome the work function and emit to vacuum. Above threshold multi-photon emission occurs at

positive excess energies under a high laser fluence. At laser fluences larger than 10^{-4} mJ/cm^2 the photoemission process transitions from purely single-photon emission to a mix of single- and multi-photon emission (Bae *et al.* (2018)). In both regimes the MTE can increase significantly as the electron can be emitted with very large excess energies. However it is the second regime that is relevant to low-QE single crystal photocathodes as there is a trade off that must be made between extracting large current densities and achieving a small MTE.

Electron heating occurs when high laser fluences are delivered to the photocathode surface by ultrafast (sub-10-ps) laser pulses which causes the temperature of the electron distribution to increase to several thousand Kelvin. For sub-10-ps timescales the electron distribution is thermally isolated from the lattice due to small electron-phonon coupling, and the difference in heat capacities between the lattice and the electron distribution leads to the electron heating effect (Anisimov *et al.* (1974); Elsayad-Ali *et al.* (1987); Hohlfeld *et al.* (2000)). It has been shown theoretically that at high laser fluences near threshold this effect plays a large role in limiting the minimum achievable MTE (Maxson *et al.* (2017)).

The non-linear processes of multi-photon emission and electron heating have been the focus of their own individual theoretical investigations (Maxson *et al.* (2017); Bae *et al.* (2018)), and they have briefly been studied experimentally (Pasmans *et al.* (2016); An *et al.* (2018)). One experiment focused on below threshold multi-photon emission from polycrystalline Cu at low laser fluences (An *et al.* (2018)). As mentioned above, this regime is not of particular interest to utilizing low-QE photocathodes for high charge density applications. Another experiment measured the emittance of two-photon photoemission from polycrystalline Cu in a UED beamline (Pasmans *et al.* (2016)). In this work emittance measurements were taken from high charge density beams above threshold and across a large range of laser fluences. While this excess

energy and fluence regime is of interest to low-QE photocathodes, it was not possible to clearly distinguish what portion of the emittance growth was due to two-photon emission or due to space charge effects (Coulomb repulsion). Recently an investigation measured the contribution that non-linear photoemission effects have on the MTE of a graphene coated Cu(110) single crystal over a wide range of laser fluences, excess energies, and laser pulse lengths (Ch. 3). Using the measured data an extrapolation technique was devised which investigated non-linear effects at high charge densities for photocathodes with QEs as high as 10^{-4} at threshold. The results show that in order to achieve the thermal limit at large charge densities (10^{-4} pC/mm^2), the photocathode must have QEs larger than 10^{-4} at threshold.

1.4 High Quantum Efficiency Photocathodes

While we have investigated the two main challenges with low-MTE metallic photocathodes, the results point to the need for further research into high QE photocathodes for high charge density applications. Such photocathodes need to be able to achieve the thermal limit at high charge densities, and maintain a low MTE for long operational times. There are several possible candidates like low electron affinity semiconductors, nanotechnology photocathodes, and materials that allow electron emission from low transverse energy states. Below we discuss each of these photocathodes in detail.

1.4.1 Low Electron Affinity Semiconductors

Electron affinity is defined as the difference between the conduction band minima and the vacuum level. Low electron affinity materials are those in which the electron affinity is smaller than the band-gap. For low electron affinity materials the QE is much higher compared to high electron affinity materials like metals due to

the suppression of electron-electron scattering (Musumeci *et al.* (2018)). For these photocathodes the dominant electron scattering mechanism is with phonons which causes electrons to lose energy slowly in comparison to electron-electron scattering (Spicer and Herrera-Gomez (1993)). Since the work function is close to the band-gap, a large fraction of electrons excited to near-bad-gap energies get emitted which results in higher QEs.

Alkali-antimonide thin films are a family of low electron affinity semiconductor photocathodes that are commonly used in photoinjectors for high brightness and high charge density applications (Vecchione *et al.* (2011); Dunham *et al.* (2013); Schmeißer *et al.* (2018)). At threshold ($\sim$ 1.9 eV) alkali-antimonides like Cs_3Sb, K_2CsSb, and Na_2KSb have QEs as high as 10^{-1} at room temperature and 10^{-4} when cryo-cooled down to 90 K (Dowell *et al.* (2010); Cultrera *et al.* (2015)). However they have typically been grown as polycrystalline thin films with very rough surfaces which prevents them from reaching thermal limit MTEs. Within the last year the first ever epitaxial growth of a $Cs_3Sb(001)$ single crystal was demonstrated (Parzyck *et al.* (2022)). While this represented a major advancement towards achieving thermal limit MTEs at high charge densities, there are still several issues that need to be addressed.

First, while it was expected that these photocathodes will achieve the thermal limit when illuminated with near threshold light, when MTE measurements were first performed the thermal limit was not obtained (Cultrera *et al.* (2015)). Initially surface non-uniformities were thought to be the cause of this. However recent measurements have shown that that the threshold is significantly smaller than what was previously thought to be the case, and only very recently have near-threshold measurements been performed (Saha *et al.* (2023b)). Second alkali-antimonide surfaces are extremely sensitive to the vacuum conditions in RF guns. Since achieving the thermal limit requires atomically clean and ordered surfaces, steps need to be taken to make alkali-

antimonides more robust before they can be utilized in RF guns. Graphene protective layers have been investigated on polycrystalline alkali-antimonides in order to make the surface more robust (Yamaguchi *et al.* (2017, 2018); Liu *et al.* (2022)), but as of yet no attempts have been made to grow graphene on alkali-antimonide single crystals. Lastly, the response time of these surfaces is relatively unknown. In general the response time is affected by the absorption depth of photons as well as the excess energy. Due to the small thickness of these thin films it is expected to be around 1 ps, but precise response time measurements are still needed. Hence alkali-antimonide single crystals still need to be subjected to thorough characterization and testing before they will realistically be considered for use in photoinjectors.

1.4.2 Nanotechnology

Recent advancements in nanotechnology has lead to a lot of interest in investigating these areas as novel photocathode technologies. In particular, photonic-integrated photocathodes and plasmonic-enhanced photocathodes are being investigated as potential options for photoinjectors. It has been proposed that using photonic structures like waveguides on photocathodes can enhance photoemission by simultaneously emitting electrons with low MTEs ($\sim$30 meV), high QE (1-10%), and fast response times (0.2-1 ps) making them suitable for a wide variety of applications (Blankemeier *et al.* (2019)). Engineering these structures remains technologically challenging and therefore investigations are in the early stages. Recently an experiment was performed as a proof-of-principle which demonstrated photoemission confined by a waveguide on a 40 nm thick Cs activated GaAs photocathode (Kachwala *et al.* (2022)). However further studies are needed to simultaneously demonstrate low MTE, high QE, and prompt response times.

Plasmonic-enhanced photocathodes utilize a nano-sized plasmonic structure which

can greatly increase the electron yield for a resonant wavelength (Perchec *et al.* (2008)). By creating nanosized rectangular grooves arranged in a sub-wavelength array on the photocathode, the grooves act as surface plasmon resonance cavities which trap the incident laser light and dramatically increase the electron yield for a resonant wavelength. The resonant wavelength can be selected by adjusting the width and depth of the grooves as well as the separation distance between neighboring grooves. Recently by designing a nano-structured array with a resonant wavelength of 720 nm, a group was able to demonstrate an increase in electron yield by 6 orders of magnitude for 800 nm laser light (Polyakov *et al.* (2013)).

1.4.3 Low Transverse Energy States

Since the transverse momentum is conserved during photoemission from single crystalline surfaces, materials that allow electron emission from low transverse energy states can be selected to achieve low MTEs and high QEs simultaneously. Such materials will typically have narrow energy dispersion bands with low effective masses localized around Γ (q=0) (Musumeci *et al.* (2018)). For example using the low effective mass of the surface state of Ag(111), low MTEs near 25 meV and high QEs of 10^{-4} were demonstrated near threshold (Karkare *et al.* (2017)).

On the extreme end, novel materials like topological insulators and Dirac semimetals have a Dirac cone at the Gamma point which makes the effective mass of any electrons emitted from the Dirac point nearly zero. Therefore they are expected to yield very low MTEs (sub-10 meV) even when operating with excess energies as large as 0.25 eV (Pan *et al.* (2011); Liu *et al.* (2014a,b); Xu *et al.* (2017); Tian *et al.* (2018)).

While all of these high QE materials have the potential of achieving low MTEs at high charge densities, they still require detailed characterization and testing before

they can be considered realistic options for use in photoinjectors. In Ch. 4 we outline a lab which has been designed to address the outstanding challenges of characterizing and testing such materials.

1.5 Thesis Outline

Chapter 1 and Ch. 5 of this thesis provide an introduction and summary of practical limitations of low mean transverse energy metallic photocathodes respectively. In Ch. 2 and Ch. 3 we discuss the two main challenges of low MTE metallic photocathodes: stability and non-linear photoemission. In Ch. 4 we present an introductory review of photocathode physics and the design of the Photocathode and Bright Beams Lab (PBBL). Such a lab is needed to investigate technologies to mitigate the practical limitations of metallic photocathodes.

In Ch. 2, we investigate the impact that a graphene protective coating has on the MTE from a photocathode. In particular we present MTE and QE measurements from a graphene coated Cu(110) single crystalline photocathode at photon energies near the photoemission threshold for both room and cryogenic temperatures. The MTE is measured over a period of a week after surface preparation to test the stability of the photocathode. We perform a surface preparation technique that only requires a low temperature anneal and not the usual Ar ion bombardment and high temperature anneal combination that is typically needed for single crystalline surfaces. To test the success of this reduced surface preparation technique LEED was used to characterize the crystal structure of the photocathode.

In Ch. 3 we investigate non-linear photoemission from a graphene-coated Cu(110) single crystalline photocathode over a wide range of laser fluences, excess energies, and laser pulse lengths. We measure the total energy and transverse momentum distributions to provide deeper insights into the non-linear photoemission process.

An extrapolation technique is presented which allows us to obtain the effects of non-linear photoemission on MTE at charge densities relevant to photoinjectors.

In Ch. 4 we provide an introductory review of photocathode physics and the brightness limiting factors that are relevant to photocathodes. We discuss the need for photocathode research facilities to test a wide variety of outstanding challenges with photocathodes. Lastly we present the design and research capabilities of the newly commissioned Photocathode and Bright Beams Lab (PBBL) at ASU. The PBBL is built to address the practical limitations of metallic photocathodes. In addition the PBBL provides a test facility that can investigate a wide variety of photocathode materials and technologies that go beyond the practical limitations posed by metallic photocathodes.

Chapter 2

NEAR-THRESHOLD PHOTOEMISSION FROM GRAPHENE-COATED CU(100)

This chapter was originally published as Knill *et al.* (2023).

2.1 Abstract

The brightness of electron beams emitted from photocathode sources plays a critical role in determining the performance of X-ray free electron lasers (XFELs) and ultrafast electron diffraction (UED) applications. In order to achieve the maximum brightness, the electrons need to be emitted from a photocathode with the lowest possible mean transverse energy (MTE). Recent investigations have shown that capping a Cu(110) photocathode with a monolayer of graphene can protect the quantum efficiency (QE) from long term exposure to varying vacuum conditions. However, there have been no studies that investigate the effects that a monolayer of graphene has on the MTE. Here we report on measurements of a graphene coated Cu(110) single crystal near the photoemission threshold for room, and liquid nitrogen, temperatures. At room temperature, a minimum MTE of 25 meV was measured at 295 nm. At liquid nitrogen temperatures, a minimum MTE of 9 meV was measured at the photoemission threshold of 290 nm.

2.2 Introduction

The performance of accelerator applications like X-ray free electron lasers (XFELs) and ultrafast electron diffraction (UED) (Siwick *et al.* (2002); Ischenko *et al.* (2017); Chatelain *et al.* (2012)) and microscopy (UEM) experiments largely depends on the brightness of pulsed electron beams generated from photoinjectors. For XFELs, an

increase in brightness will lead to an increase in both the maximum X-ray lasing energies, and the X-ray pulse energies (Ferrario (2015)). In addition, brighter electron beams are crucial for developing smaller, and more accessible, university-scale XFELs (Rosenzweig *et al.* (2020)). For single shot UED, the brightness of existing electron beams typically limits studies to crystals with a lattice constant of 1 nm. The transverse coherence lengths can be increased allowing studies of crystals with larger lattice sizes by using a pinhole at the cost of the bunch charge and poorer signal-to-noise ratio. Increasing the brightness of electron beams, will increase the transverse coherence length and allow for the study of larger crystals without compromising the signal-to-noise ratio (Musumeci *et al.* (2010)). For high repetition rate stroboscopic UED/UEM applications, a brighter electron beam will increase the signal relative to the noise as well as reduce the data acquisition time (Ji *et al.* (2019)). Signal-to-noise is critical for these applications and limits their resolution as shown by Bryan et al (Bainbridge *et al.* (2016)).

For applications that require a high peak charge density from the cathode, like XFELs and single shot UED, the maximum beam brightness scales according to the following relation:

$$B \propto \frac{E^n}{\mathrm{MTE}} \tag{2.1}$$

where E is the accelerating electric field, n is a real number between 1 and 2 where the value depends on the design of the photoinjector, and MTE is the mean transverse energy of the electrons emitted from the cathode, and is equivalent to the temperature of the electrons in vacuum (Bazarov *et al.* (2009)). For applications that require only a few electrons per pulse, like stroboscopic UED/UEM (Barwick *et al.* (2008); Carbone *et al.* (2009); da Silva *et al.* (2018); Ji *et al.* (2019); Aseyev *et al.* (2020)) the brightness is inversely proportional to the MTE as well as the emission area on the cathode (Musumeci *et al.* (2018)). MTE is related to the intrinsic cathode emittance

($\epsilon_{n,x}$) as

$$\epsilon_{n,x}/\sigma_x = \sqrt{MTE/m_e c^2} \tag{2.2}$$

where σ_x is the rms emission spot size on the cathode, m_e is the rest mass of the electron, and c is the speed of light. Thus, understanding and minimizing the MTE is crucial to achieving the brightest possible beams from photocathodes for all photoinjectors.

By combining Spicer's three-step model of photoemission and Sommerfeld's free electron gas theory in solids, Dowell and Schmerge showed that for typical metallic cathodes the MTE is roughly equal to $E_{excess}/3$, where the excess energy (E_{excess}) is defined as the difference between the photon energy ($\hbar\omega$) and the work function (ϕ) of the photocathode (Dowell and Schmerge (2009)). This theory was based on several assumptions like a nearly free electron gas model, parabolic dispersion relations, conservation of transverse momentum, constant density of states, and zero lattice temperature. While many of these assumptions are unrealistic, the MTE predicted in this theory has been verified experimentally (Feng *et al.* (2017)). For low or negative excess energy, the emission occurs from the tail of the Fermi distribution and the MTE reaches the thermal limit of $k_b T$, where k_b is the Boltzmann constant, and T is the temperature of the electrons in the crystal (Vecchione *et al.* (2013)). For small laser fluences, the electrons are in equilibrium with the lattice and thus, the temperature of the electrons is equivalent to the temperature of the cathode. For a room temperature cathode the thermal limit is 25 meV, a result that has been demonstrated experimentally from polycrystalline Sb (**?**). It has also been shown experimentally that by cryogenically cooling the cathode, the thermal limit decreases, and sub-25 meV MTEs can be achieved (Cultrera *et al.* (2015); Karkare *et al.* (2020)). As the temperature reaches cryogenic temperatures, it becomes increasingly difficult to reach the thermal limit. One factor that leads to a small increase in MTE above the

thermal limit is the low transmission probability for low kinetic energy electrons near the photoemission threshold (Schroeder and Adhikari (2019); Karkare *et al.* (2020)). Another factor that can significantly increase the MTE above the thermal limit is the surface non-uniformities of physical roughness and work function variations (Karkare and Bazarov (2015); **?**). These non-uniformities can lead to transverse electric fields that can increase the the MTE by several factors (Gevorkyan *et al.* (2018)). To minimize the MTE degrading effects of surface nonuniformities, it is crucial to emit electrons from an atomically ordered single crystalline surface (Karkare *et al.* (2017)).

For single crystalline ordered surfaces, the transverse momentum is conserved during photoemission. In order to achieve a minimum MTE, it is essential that the emission does not occur from electronic states with a large transverse momentum. Hence selecting single crystal cathodes with a band structure that allows emission from low transverse momentum states is crucial to minimizing the MTE (Karkare *et al.* (2017)).

The 5 meV Cu photocathode is an ideal candidate for applications that do not require large charge densities like stroboscopic UED/UEM. However, the low quantum efficiency (QE) of Cu, typically on the order of 10^{-8} when operating at 35 K and with near-threshold photon energies, makes it unsuitable for high charge density applications like XFELs and single-shot UED experiments. For those applications, a large laser fluence is required to extract the desired beam current. At these large laser fluences, the MTE becomes limited by the non-linear photoemission effects of multi-photon emission (Bae *et al.* (2018); Knill *et al.* (2021)) and electron heating (Maxson *et al.* (2017)), and small MTEs are no longer attainable. To alleviate the effects of non-linear photoemission, high quantum efficiency and low electron affinity semiconductors like Alkali-antimonides are used as photocathodes (Dunham *et al.* (2013); Musumeci *et al.* (2018)). For such photocathode surfaces, the QE is large

enough where the desired charge density can be extracted at lower laser fluences where the non-linear photoemission effects do not significantly impact the MTE. However, such cathodes are extremely sensitive to vacuum conditions making their use technologically complicated and expensive. Capping of such cathodes with a robust protective 2D layer that doesn't affect the photoemission properties of QE and MTE adversely is being investigated (Yamaguchi *et al.* (2017, 2018); Liu *et al.* (2022)).

Recent investigations have looked at the efficacy of capping photocathode surfaces with a thin film to increase their stability without negatively impacting their photoemission properties. One such investigation showed that capping a Cu(110) single crystal with a monolayer of graphene can significantly improve the stability of the cathode surface and preserve the quantum efficiency at atmospheric conditions (Liu *et al.* (2017)). While these results were promising, there still remained the question of whether or not these cathodes could be used to achieve a brighter electron beam. Hence reliable MTE measurements are necessary to complete the investigation of the effects that a graphene coating has on the photoemission properties.

In this chapter we investigate the effects that a graphene coating has on the MTE of a Cu(110) single crystal. We measure the MTE at photon energies near threshold at both room temperature and at liquid nitrogen temperatures to confirm that a graphene coating does not impact the ability to achieve MTEs close to cryogenic thermal limits. Our measurements show that the MTE reaches the thermal limit of 25 meV at room temperature, and 9 meV when cooling down to liquid nitrogen temperatures and are very much in-line with the well established theoretical model for MTE and QE first put forth by Dowell and Schmerge (Dowell and Schmerge (2009)). Additionally, attaining these low MTEs required minimal surface preparation in comparison to the Cu(100) surface which has previously demonstrated similar,

record low MTEs (Karkare *et al.* (2020)). The sample required a single anneal at 345°C to achieve these low MTEs. This is in contrast to a non-graphene-coated Cu sample which requires several cycles of ion bombarding and annealing up to 600°C to achieve an atomically ordered and smooth surface and the low MTEs. The MTE was measured over a period of a week after surface preparation to test the stability of the cathode. During this time, the thermal limit of 25 meV was consistently measured indicating an extremely stable cathode (Knill *et al.* (2022)). This demonstrates that a monolayer of graphene grown on a single crystal can be a useful step to improve the stability of a cathode with no discernible negative effects on the photoemission properties.

2.3 Experimental Setup

For this work a commercially available, mirror-polished, Cu(110) single crystal was purchased from Princeton Scientific and sent to the Global Innovation Center at Kyushu University in Japan for graphene growth. Graphene was grown using chemical vapor deposition using the following recipe. First, the Cu(110) substrate was annealed in a 500 sccm continuous flow of mixed hydrogen (2%) and argon (98%) in a tube furnace at 1000°C for 1 hour at atmospheric pressure. This high anneal removed any oxide layer that may have been present on the Cu substrate, and ensured that the graphene was grown on a pure, contaminant free surface. Then the tube furnace was ramped to 1075°C, and the growth cycle was completed by flowing methane gas continuously for 3 hours to achieve a methane concentration of 10 ppm (Ago *et al.* (2013)). Then the sample was forced to cool to room temperature and transported to Arizona State University under atmospheric conditions. After several weeks of exposure to atmospheric conditions, the sample was loaded into a UHV preparation chamber where it was annealed at 345°C for 3 hours with a base pressure of 5 $\times$

10^{-10} Torr. It was then allowed to cool for 2 hours before being loaded into the UHV connected analysis chamber which has a base pressure of 1×10^{-10} Torr. The analysis chamber houses the electron energy analyzer as well as low energy electron diffraction (LEED) and Auger electron spectroscopy (AES) experiments. An Auger spectrum showed the presence of only carbon and copper peaks. Figure 2.1 shows a higher order LEED pattern that was collected at 155 eV with a sharp pattern that is in agreement with previously measured LEED patterns from graphene coated Cu(110) by other groups (Wilson *et al.* (2013)). This indicates that the sample had a contaminant free, atomically ordered single crystalline surface. Once the sample was determined to be an atomically pristine surface, it was positioned in front of the electron energy analyzer for MTE measurements.

The electron energy analyzer is a time-of-flight based detector comprising of a sample and delayline detector arranged approximately 4 cm $\pm$ 0.1 cm apart in a parallel plate configuration. A sub-picosecond pulsed laser was focused down to the sample to a sub-100 μm spot size, and the emitted electrons were accelerated towards the detector by an accelerating voltage of 72 V. The delayline detector measures the transverse positions of the electrons as well as their time of flight from the sample to the detector. And from that, the transverse energies and momenta can be calculated trivially. Further details of the electron energy analyzer can be found here (Karkare *et al.* (2019)).

For this work a 130 fs pulse width, 500 kHz repetition rate, laser was used along with a tunable wavelength optical parametric amplifier (LightConversion Orpheus pumped by the LightConversion Pharos). Neutral density filters were used to keep the laser intensity low enough to ensure that the photoemission was purely linear, and so that at most one electron was emitted per pulse. The sample was irradiated with photons ranging from 260 nm (4.77 eV) to 300 nm (4.13 eV) in increments of 5 nm.

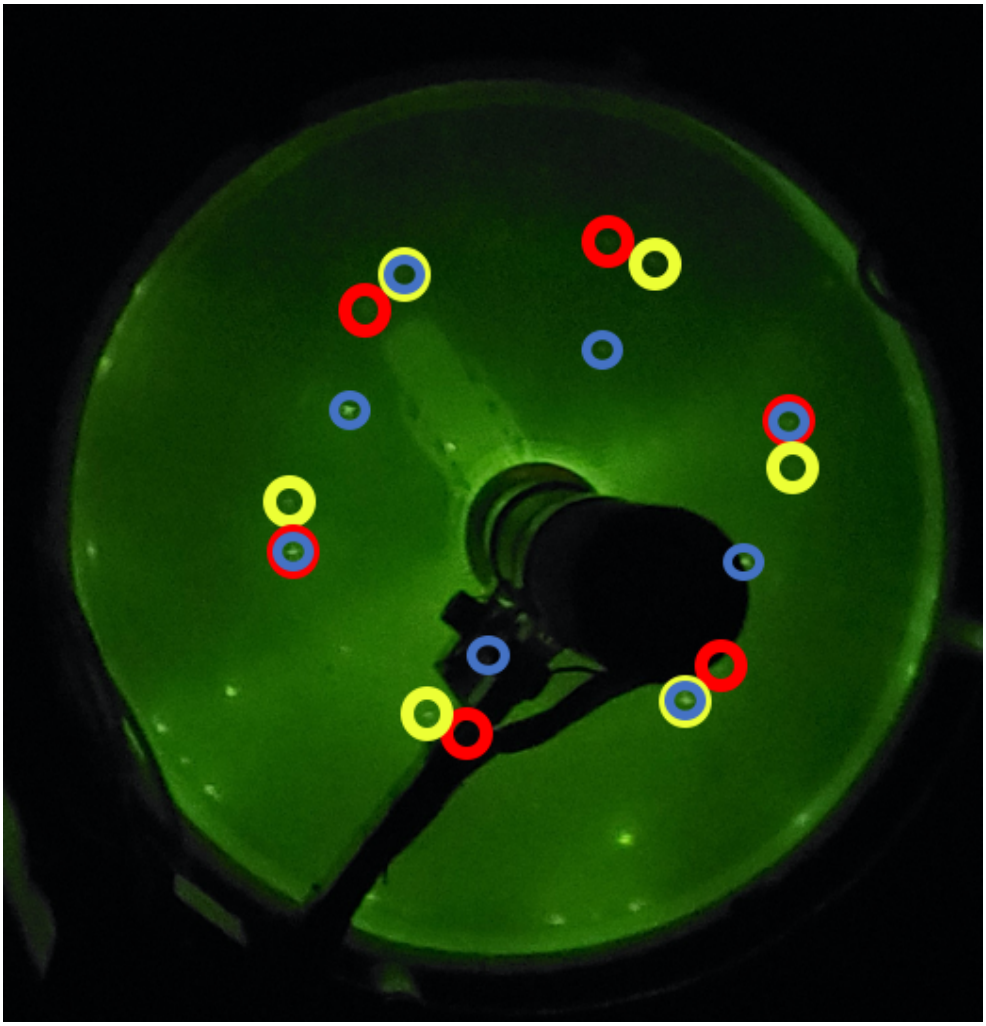

Figure 2.1: LEED Pattern Collected at 155 eV for Graphene-Coated Cu(110). The Blue Circles Show the Rectangular Pattern That is Associated With a Cu(110) Single Crystal. The Red and Yellow Circles Show a Hexagonal Pattern That is Associated With a Monolayer of Graphene, with the Graphene Growth Determined by the Underlying Cu. Despite the Difference Between the Hexagonal and Rectangular Patterns of Graphene and Cu, They Share a Common Periodicity. In This Case There are Two Preferred Growth Orientations, Hence There are Two Hexagonal Patterns. This Pattern is in Agreement With Previously Measured LEED Patterns From Graphene-Coated Cu(110) By Other Groups (Wilson *et al.* (2013)).

The laser was p-polarized and incident at an angle of 50° with respect to the normal, and the laser was focused down to between 60 and 80 μm. While the laser spot size changed slightly from each measurement, the emission occurred from the same central location on the cathode. The measurements were taken at room temperature (300 K) and at colder temperatures of 100 K and 77 K. The colder temperatures were achieved using a continuous flow liquid helium cryostat that was connected to the sample.

2.4 Theoretical Comparison

In order to test the accuracy of our experimental results with theory, our measurements were compared with a model of photoemission from single crystalline cathodes by Vecchione et al. This model shows that for a given temperature T, the MTE and QE can be expressed by Eq. (3) and Eq. (4) respectively (Vecchione *et al.* (2013)).

$$\mathrm{MTE} = kT\frac{\mathrm{Li}_3\{-\exp[\frac{e}{kT}(\hbar\omega-\phi)]\}}{\mathrm{Li}_2\{-\exp[\frac{e}{kT}(\hbar\omega-\phi)]\}} \tag{2.3}$$

$$\mathrm{QE} = S_{12}\frac{\mathrm{Li}_2\{-\exp[\frac{e}{kT}(\hbar\omega-\phi)]\}}{\mathrm{Li}_2\{-\exp[\frac{e}{kT}\mu]\}} \tag{2.4}$$

where Li_n is a polylogarithm function defined as

$$\mathrm{Li}_n(z) = \frac{(-1)^{n-1}}{(n-2)!}\int_0^1 \frac{1}{t}\log(t)^{n-2}\log(1-zt)\mathrm{d}t. \tag{2.5}$$

2.5 Experimental Results

2.5.1 Mean Transverse Energy

Figure 2.2 shows the measured MTE at wavelengths at, and above, threshold for three temperatures along with theoretical MTE curves that were calculated using

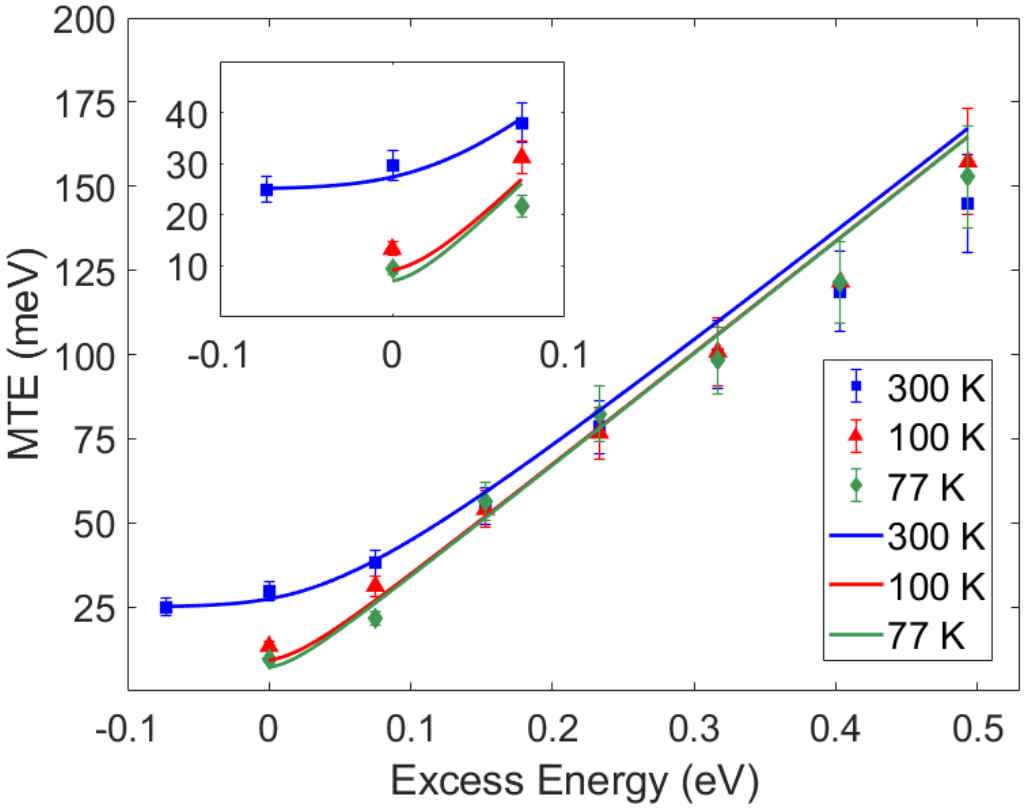

Figure 2.2: Measured Data Points and Theoretical Curves of MTE for 300 K, 100 K, and 77 K Between E_{excess} = -0.1 eV and E_{excess} = 0.5 eV. The Theoretical MTE Curves Were Calculated Using Eq. 2.3. For 100 K and 77 K It Was Not Possible to Obtain Linear Photoemission Data at E_{excess} = -0.1 eV. The Error in the Measurement Was Estimated to Be 10% Due to Measurement Systematics.

Eq. 2.3. The experimental data for all three temperatures is in good agreement with the MTE predicted by Eq. 2.3. Looking at the experimental results from E_{excess} = 0.49 eV (260 nm) to E_{excess} = 0.15 eV (280 nm), the MTE is roughly the same for all three temperatures. In this wavelength region, the excess energy is large enough that the emission does not occur from the tail of the Fermi distribution, and the MTE is roughly equal to $E_{excess}/3$ as predicted by Dowell and Schmerge (Dowell and Schmerge (2009)). As we get closer to the photoemission threshold of 4.28 eV (290 nm), or equivalently as the excess energy approaches zero, the emission occurs more from the Fermi tail, and we see a reduction in MTE with decreasing temperature. At room temperature, the smallest MTE measured was the thermal limit of 25 meV at E_{excess} = -0.08 eV (295 nm). For the cryo-cooled measurements it was not possible to measure linear emission at E_{excess} = -0.08 eV due to a very small QE that is less than 10^{-9}. Instead the minimum MTE for the cryo-cooled measurements occurred at the photoemission threshold of 290 nm, where we measured 13 meV and 9 meV for 100 K and 77 K respectively. While these MTE measurements are small, it does not reach the thermal limit at 100 K and 77 K due to the low transmission probability of low energy electrons near the photoemission threshold (Schroeder and Adhikari (2019); Karkare *et al.* (2020)).

2.5.2 Quantum Efficiency

Figure 2.3 shows the QE measurements and theoretical curves for the various excess energies and temperatures. The current was determined by treating each count measured by the delayline detector as one electron, and from that the QE was calculated. However this method does not account for every electron emitted from the cathode, and instead puts a lower limit on the current. Therefore the QE measured is some unknown factor lower than the actual QE. We expect this factor to

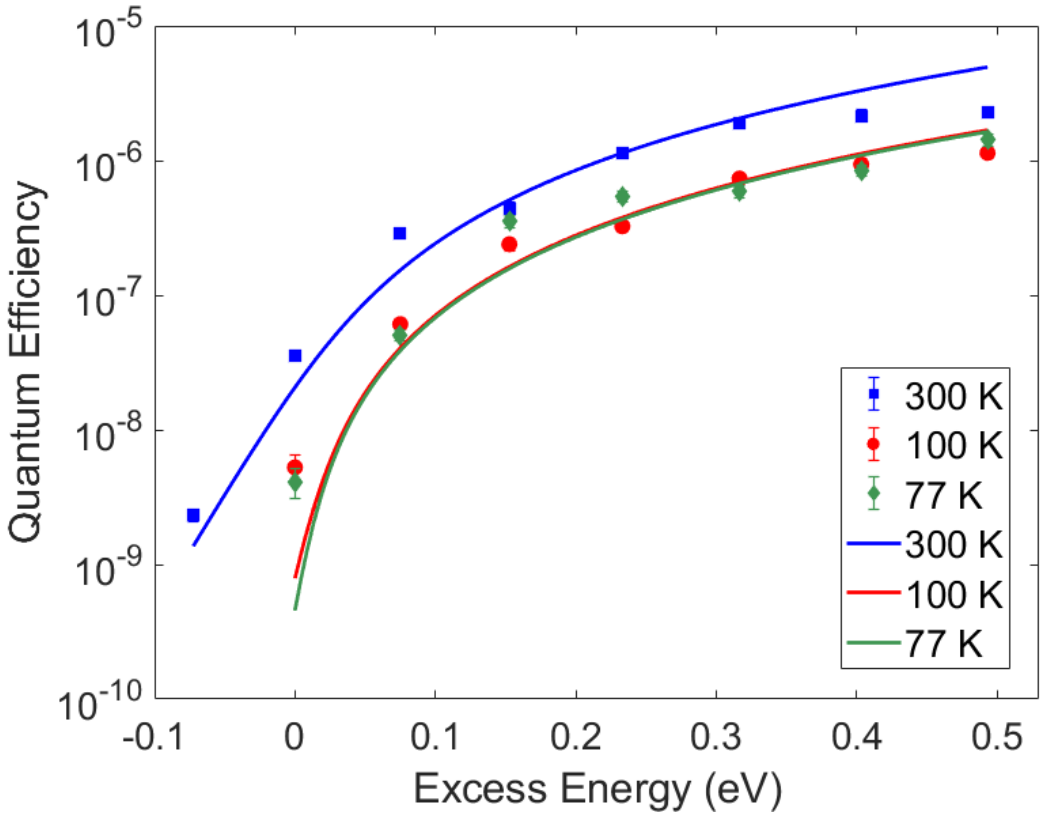

Figure 2.3: Measured Data Points and Theoretical Curves of the QE for 300 K, 100 K and 77 K Between E_{excess} = -0.1 eV and E_{excess} = 0.5 eV. The Theoretical QE Curves Were Calculated From Eq. 2.4. The Current Measured Represented Only a Fraction of the Actual Current Emitted, and so the QE Is Some Unknown Factor Lower Than the Actual QE. For 100 K and 77 K It Was Not Possible to Obtain Linear Photoemission Data at E_{excess} = -0.1 eV. The Error In the Measurement Was Estimated to Be 10% Due to Measurement Systematics.

be of the order of unity. With this unknown factor in mind we can still compare the experimental and theoretical results, and we can see that the QE is in good agreement the trend predicted by Eq. 2.4. For 100 K and 77 K, the measured QE decreases by an order of magnitude near the photoemission threshold. In spite of this drop in QE, it is still sufficient for stroboscopic UED/UEM experiments that require a few or single electron per pulse (Bainbridge *et al.* (2016)). For high charge density applications like XFELs and single shot UED experiments, a large laser fluence is required to extract the necessary current. At these large laser fluences, the non-linear photoemission effects limit the MTE and Cu cathodes are no longer suitable options (Maxson *et al.* (2017); Bae *et al.* (2018); Knill *et al.* (2021)).

2.5.3 Cathode Stability

While the graphene coated Cu(110) single crystal gives MTE very much comparable to the bare non-graphene coated Cu(100) (Karkare *et al.* (2020)), it does significantly improve the stability and makes the sample preparation process significantly easier. In order to achieve sub-10 meV MTEs, bare Cu single crystals require repeated ion sputtering and high temperature (600°C) annealing cycles in-situ to achieve the atomically ordered pristine surface. While for the graphene coated Cu, the atomically ordered single crystalline surface is achieved during the graphene growth, and can be performed off site and transported in atmosphere over several weeks. Then a simple 345°C anneal for 3 hours is performed to remove any oxide layer and get the cathode ready for operation. Current photoinjectors do not have the in-situ surface preparation techniques that are necessary to achieve a well ordered single crystalline surface, and so polycrystalline cathodes are typically used. In order to use single crystal cathodes to achieve the brightest possible beams, photoinjectors would require significant, and costly, modifications. Adding the capability to perform the 345°C anneal needed

for the graphene coated Cu requires much less modification, and is significantly less costly than adding the surface preparation techniques required for bare single crystals. Thus making graphene coated single crystals promising cathodes for current and future photoinjectors.

2.6 Conclusion

In conclusion, we present MTE measurements for a graphene coated Cu(110) single crystal at room, and cryogenic, temperatures. Our results show that a graphene coating does not negatively impact the MTE, and that a sub-10 meV MTE can be measured from a cryogenically cooled graphene coated Cu(110) single crystal. The thermal limit of 25 meV at room temperature was consistently measured for 7 days, indicating that the cathode was extremely stable (Knill *et al.* (2022)). Furthermore the graphene coating significantly simplifies the in-situ surface preparation that is required to achieve a well ordered single-crystal, thus making graphene coated single crystals a viable option for current and future photoinjectors.

2.7 References

Ago, H., K. Kawahara, Y. Ogawa, S. Tanoue, M. A. Bissett, M. Tsuji, H. Sakaguchi, R. J. Koch, F. Fromm, T. Seyller, K. Komatsu and K. Tsukagoshi, "Epitaxial growth and electronic properties of large hexagonal graphene domains on Cu(111) thin film", Appl. Phys. Exp **6**, 075101 (2013).

Aseyev, S. A., E. A. Ryabov, B. N. Mironov and A. A. Ischenko, "The development of ultrafast electron microscopy", Crystals **10(6)**, 452 (2020).

Bae, J. K., I. Bazarov, P. Musumeci, S. Karkare, H. A. Padmore and J. Maxson, "Brightness of femtosecond nonequilibrium photoemission in metallic photocathodes at wavelengths near the photoemission threshold", J. Appl. Phys. **124**, 244903 (2018).

Bainbridge, A. R., C. W. B. Myers and W. A. Bryan, "Femtosecond few-to single-electron point-projection microscopy for nanoscale dynamic imaging", Struct. Dyn. **3**, 023612 (2016).

Barwick, B., H. S. Park, O.-H. Kwon, J. S. Baskin and A. H. Zewail, "4D imaging

of transient structures and morphologies in ultrafast electron microscopy", Science **322**, 1227 (2008).

Bazarov, I. V., B. M. Dunham and C. K. Sinclair, "Maximum achievable brightness from photoinjectors", Phys. Rev. Lett. **102**, 104801 (2009).

Carbone, F., O. Kwon and A. H. Zewail, "Dynamics of chemical bonding mapped by energy-resolved 4d electron microscopy", Science **325**, 181 (2009).

Chatelain, R. P., V. R. Morrison, C. Godbout and B. J. Siwick, "Ultrafast electron diffraction with radio-frequency compressed electron pulses", Appl. Phys. Lett. **101**, 081901 (2012).

Cultrera, L., S. Karkare, H. Lee, X. Liu, I. Bazarov and B. Dunham, "Cold electron beams from cryocooled, alkali antimonide photocathodes", Phys. Rev. ST Accel. Beams **18**, 113401 (2015).

da Silva, N. R., M. Moller, A. Feist, H. Ulrichs, C. Ropers and S. Schafer, "Nanoscale mapping of ultrafast magnetization dynamics with femtosecond lorentz microscopy", Phys. Rev. X **8**, 031052 (2018).

Dowell, D. H. and J. Schmerge, "Quantum efficiency and thermal emittance of metal photocathodes", Phys. Rev. ST Accel. Beams **12**, 074201 (2009).

Dunham, B., J. Barley, A. Bartnik, I. V. Bazarov, L. Cultrera, J. Dobbns, G. Hoffstaetter, B. Johnson, R. Kaplan, S. Karkare, V. Kostroun, Y. Li, M. Liepe, X. Liu, F. Loehl, J. M. Maxson, P. Quigley, J. Reilly, D. Rice, D. Sabol, E. Smith, K. Smolenski, M. Tigner, V. Vesherevich, D. Widger and Z. Zhao, "Record high-average current from a high-brightness photoinjector", Appl. Phys. Lett. **102**, 034105 (2013).

Feng, J., S. Karkare, J. Nasiatka, S. Schubert, J. Smedley and H. A. Padmore, "Near atomically smooth alkali antimonide photocathode thin films", J. Appl. Phys. **121**, 044904 (2017).

Ferrario, M., "Overview of FEL injectors", Proceedings of EPAC, Edinburgh, Scotland (2015).

Gevorkyan, G., S. Karkare, S. Emamian, I. V. Bazarov and H. A. Padmore, "Effects of physical and chemical surface roughness on the brightness of electron beams from photocathodes", Phys. Rev. ST Accel. Beams **21**, 093401 (2018).

Ischenko, A. A., P. M. Weber and R. J. D. Miller, "Capturing chemistry in action with electrons: Realization of atomically resolved reaction dynamics", Chem. Rev. **117**, 11066 (2017).

Ji, F., D. Durham, A. Minor, P. Musumeci, J. Navaroo and D. Filippetto, "Ultrafast relativistic electron nanoprobes", Nat. Comm. Phys. **2**, 54 (2019).

Karkare, S., G. Adhikari, W. A. Schroeder, J. K. Nangoi, T. Arias, J. M. Maxson and H. A. Padmore, "Ultracold electrons via near-threshold photoemission from single-crytal Cu(100)", Phys. Rev. Lett. **125**, 054801 (2020).

Karkare, S. and I. Bazarov, "Effects of surface nonuniformities on the mean transverse energy from photocathodes", Phys. Rev. Appl. **4**, 024015 (2015).

Karkare, S., J. Feng, X. Chen, W. Wan, F. J. Palomares, T.-C. Chiang and H. A. Padmore, "Reduction of intrinsic electron emittance from photocathodes using ordered crystalline surfaces", Phys. Rev. Lett. **118**, 164802 (2017).

Karkare, S., J. Feng, J. Maxson and H. A. Padmore, "Development of a 3-D energy-momentum analyzer for mev-scale energy electrons", Rev. Sci. Instrum. **90**, 053902 (2019).

Knill, C. J., H. A. Padmore and S. S. Karkare, "Near-threshold nonlinear photoemission from Cu(100)", Proceedings of the 12th International Particle Accelerator Conference, Sao Paulo, Brazil p. WEPAB099 (2021).

Knill, C. J., H. Yamaguchi, K. Kawahara, G. Wang, E. Batista, P. Yang, H. Ago, N. Moody and S. Karkare, "Near-threshold photoemission from graphene-coated Cu(110)", Phys. Rev. Appl. **19**, 014015 (2023).

Knill, C. J., H. Yamaguchi, K. Kawahara, G. Wang, E. Batista, P. Yang, H. Ago, N. A. Moody and S. S. Karkare, "Near threshold photoemission from graphene coated cu single crystals", Proceedings of the 3rd North American Particle Acclerator Conference, **WEPA66** (2022).

Liu, F., L. Guo, J. DeFazio, V. Pavlenko, M. Yamamoto, N. A. Moody and H. Yamaguchi, "Photoemission from bialkali photocathodes through an atomically thin protection layer", ACS Appl. Mater. Inter. **14**, 1710 (2022).

Liu, F., N. A. Moody, K. L. Jensen, V. Pavlenko, C. W. N. Villarrubia, A. D. Mohite and G. Gupta, "Single layer graphene protective gas barrier for copper photocathodes", Appl. Phys. Lett. **110**, 041607 (2017).

Maxson, J. M., P. Musumeci, L. Cultrera, S. Karkare and H. A. Padmore, "Ultrafast laser pulse heating of metallic photocathodes and its contribution to intrinsic emittance", Nucl. Instrum. Meth. A **865**, 99 (2017).

Musumeci, P., J. T. Moody, C. Scoby, M. S. Gutierrez, H. A. Bender and N. S. Wilcox, "High quality single shot diffraction patterns using ultrashort mega-electron volt electron beams from a radio frequency photoinjector", Rev. Sci. Instrum. **81**, 013306 (2010).

Musumeci, P., J. Navarro, J. az. Rosenzweig, L. Cultrera, I. Bazarov, J. Maxson, S. Karkare and H. Padmore, "Advances in bright electron sources", Nucl. Instrum. Meth. A **907**, 208 (2018).

Rosenzweig, J. B., N. Majernik, R. R. Robles, G. Andonian, O. Camacho, A. Fukasawa, A. Kogar, G. Lawler, J. Miao, P. Musumeci, B. Naranjo, Y. Sakai, R. Candler, B. Pound, C. Pellegrini, C. Emma, A. Halavanau, J. Hastings, Z. Li, M. Nasr, S. Tantawi, P. Anisimov, B. Carlsten, F. Krawczyk, E. Simakov, L. Faillace, M. Ferrario, B. Spataro, S. Karkare, J. M. Maxson, Y. Ma, J. Wurtele, A. Murokh, A. Zholents, A. Cianchi, D. Cocco and S. B. van der Geer, "An ultra-compact x-ray free electron laser", New J. Phys. **22**, 093067 (2020).

Schroeder, W. A. and G. Adhikari, "Evaluation of photocathode emission properties in an electron gun: one-step photoemission from bulk band to vacuum states", New J. Phys. **21**, 033040 (2019).

Siwick, B. J., J. R. Dweyer, R. E. Jordan and R. J. D. Miller, "Ultrafast electron optics: Propagation dynamics of femtosecond electron packets", J. Appl. Phys. **92**, 1643 (2002).

Vecchione, T., D. Dowell, W. Wan, J. Feng and H. A. Padmore, "Quantum efficiency and transverse momentum from metals", Proceedings of FEL2013, Geneva, Switzerland p. 424 (2013).

Wilson, N. R., A. J. Marsden, M. Saghir, C. J. Bromley, R. Schaub, G. Costantini, T. W. White, C. Partridge, A. Barinov, P. Dudin, A. M. Sanchez, J. J. Mudd, M. Walker and G. R. Bell, "Weak mismatch epitaxy and structural feedback in graphne growth on copper foil", Nano. Res. **6(2)**, 99 (2013).

Yamaguchi, H., F. Liu, J. DeFaxio, M. Gaowei, C. W. N. Villarrubia, J. Xie, V. Pavlenko, K. L. Jensen, J. Smedley, A. D. Mohite and N. A. Moody, "Free-standing bialkali photocathodes using atomically thin substrates", Adv. Mater. Inter. **5**, 1800249 (2018).

Yamaguchi, H., F. Liu, J. DeFaxio, C. W. N. Villarrubia, D. Finkenstadt, A. Shabaev, K. L. Jensen, V. Pavlenko, M. Mehl, S. Lambrakos, G. Gupta, A. D. Mohite and N. A. Moody, "Active bialkali photocathodes on free-standing graphene substrates", npj 2D Mater. Appl. **1**, 12 (2017).

Chapter 3

EFFECTS OF NON-LINEAR PHOTOEMISSION ON MTE FROM METAL PHOTOCATHODES

3.1 Abstract

In order to improve the performance of linear accelerator applications like X-ray free electrons lasers (XFELs) and ultrafast electron diffraction (UED) and microscopy (UEM) experiments, it is essential that electrons are emitted from photocathodes with the smallest possible mean transverse energy (MTE). Metallic photocathodes are popular due to their relatively low MTE, quick response time, and robustness under varying vacuum conditions. However they typically have a very low quantum efficiency (QE) which requires a large laser fluence in order to extract the desired charge density for applications like XFELs and single-shot UED/UEM experiments. At these large laser fluences the non-linear photoemission effects of multi-photon emission and electron heating begin to dominate the photoemission process. Several recent theoretical investigations have shown that these non-linear effects can increase the MTE dramatically. However there has not been a detailed experimental study of these non-linear effects, and such an investigation is necessary to allow for a well-developed theory of non-linear photoemission. Here we report on measurements of non-linear near-threshold photoemission from a graphene coated Cu(110) photocathode at laser pulse lengths of 130 fs, 1 ps and 10 ps. We extrapolate our measured data to find the ideal irradiating photon energy that results in a minimum MTE from a Cu photocathode for charge densities relevant to photoinjectors, and specify quantum efficiency requirements to obtain the thermally limited MTE at these charge

densities.

3.2 Introduction

The brightness of ultrafast electron pulses generated by photoinjectors is crucial to the performance of linear accelerator applications like X-ray free electron lasers (XFELs) and single-shot ultrafast electron diffraction (UED) and microscopy (UEM) experiments. For XFELs, a brighter electron beam will increase both the X-ray pulse energy and maximum lasing energies (Ferrario (2015)). This will enable investigations into the atomic structure of materials and lead to the production of molecular movies of chemical and biological processes (Minitti *et al.* (2015)). In addition, a brighter beam will enable the construction of smaller, university-scale XFELs which will significantly increase the accessibility of these experiments to the scientific community (Rosenzweig *et al.* (2020)). For single-shot UED/UEM experiments a brighter electron beam will increase the transverse coherence length and thus the spatial-temporal resolution (Musumeci *et al.* (2010)). This will enable the study of larger lattice sizes like proteins and macromolecular assemblies.

For the above applications the maximum beam brightness occurs at the photoemission source, or photocathode, and is given by the following relation:

$$B \propto \frac{E^n}{\mathrm{MTE}} \tag{3.1}$$

where E is the accelerating electric field; n is a real number between 1 and 2 which depends on the design of the photoinjector; and MTE is the mean transverse energy of the photocathode (Bazarov *et al.* (2009)). The MTE is also related to the intrinsic emittance $\epsilon_{n,x}$ of the photocathode as:

$$\epsilon_{n,x}/\sigma_x = \sqrt{\mathrm{MTE}/m_e c^2} \tag{3.2}$$

where σ_x is the rms laser spot size; m_e is the mass of the electron; and c is the speed

of light. The MTE is the key figure of merit in determining the brightness of the electron beam and it is equivalent to the temperature of the electrons in vacuum (Bazarov *et al.* (2009)). Hence understanding and minimizing the MTE is necessary to achieving the brightest possible electron beams for linear accelerator applications.

Using Spicer's 3-step model of photoemission, Dowell and Schmerge demonstrated that for typical metallic photocathodes the MTE roughly obeys

$$\text{MTE} = \frac{E_{excess}}{3} \tag{3.3}$$

where E_{excess} is the excess energy and is defined as the difference between the photon energy ($\hbar\omega$) and the work function (ϕ) (Dowell and Schmerge (2009)). For small or negative excess energies the electrons are emitted from the tail of the Fermi-Dirac distribution and the MTE approaches the thermal limit k_BT where k_B is the Boltzmann constant and T is the temperature of the electron distribution in the lattice (Vecchione *et al.* (2013)). At room temperature the thermal limit is 25 meV, a result that has been experimentally verified from several systems like thin Sb films (Feng *et al.* (2017)), Cu(100) (Karkare *et al.* (2020)), and graphene coated Cu(110) (Knill *et al.* (2023)). For small laser fluences, the electron distribution is essentially in equilibrium with the lattice and therefore the temperature of the electron distribution is equivalent to the temperature of the photocathode. Hence the thermal limit can be reduced below 25 meV by cooling the photocathode to cryogenic temperatures. By cryogenically cooling the photocathode below liquid nitrogen temperatures (77 K), sub-10 meV MTEs have been measured from well ordered single crystalline surfaces of Cu and graphene coated Cu when operating near zero excess energy (Karkare *et al.* (2020); Knill *et al.* (2023)). In order to achieve these low MTEs it is necessary that the photocathode is a well ordered single crystal, as such surfaces minimize the MTE-degrading surface nonuniformities of physical and chemical roughness (Karkare

and Bazarov (2015); Karkare *et al.* (2017); Gevorkyan *et al.* (2018)). While these low MTEs represent a significant improvement on the 100 - 500 meV MTEs typically found in photoinjectors today, they come at the expense of an extremely low quantum efficiency, or QE. In particular, the QE of Cu is 10^{-7} at room temperature (Dowell *et al.* (2006)) and as low as 10^{-9} at liquid nitrogen temperatures (Knill *et al.* (2023)) when operating near zero excess energy. In order to extract the large current densities necessary for XFELs and UED, a high laser fluence >10 mJ/cm^2 is required at room temperature for such photocathodes. However at these high laser fluences the non-linear photoemission effects of multi-photon emission and electron heating begin to dominate the photoemission process and limit the minimum achievable MTE (Maxson *et al.* (2017); Bae *et al.* (2018)).

When considering photon energies close to the work function, two regimes related to the multi-photon emission phenomenon exist. The first is at negative excess energies where the energy of the photon is less than the work function and therefore an electron typically requires at least two photons to overcome the photoemission threshold. At negative excess energies near the photoemission threshold it is still possible for single-photon emission to occur from the tail of the Fermi-Dirac distribution. However this process represents only a small fraction of the total electron emission and most electrons are emitted via the multi-photon process. The second regime occurs at positive, but small, excess energies under a large laser fluence. In this regime, at laser fluences higher than 10^{-3} mJ/cm^2 multi-photon emission dominates the photoemission process and significantly increases the MTE (Bae *et al.* (2018)). It is this second regime that is relevant to photoinjectors as there is a trade off between extracting large current densities and achieving small a emittance.

Electron heating occurs when high laser fluences around 10 mJ/cm^2 are delivered to a sample by ps or sub-ps pulses and heat the electrons to several thousand Kelvin.

At sub-ps timescales the electron distribution is essentially thermally isolated from the lattice due to small electron-phonon coupling. And the difference in heat capacities between the electron distribution and lattice leads to a heating effect of the electrons. The electron distribution and the lattice then reach an equilibrium on ps-timescales due to electron-phonon scattering (Anisimov *et al.* (1974); Elsayad-Ali *et al.* (1987)). A recent theoretical investigation looked at the impact that electron heating has on the MTE, and showed that at high laser fluences and small excess energies the minimum achievable MTE is limited by electron heating (Maxson *et al.* (2017)). It was also shown that partial mitigation of electron heating can be achieved by irradiating the photocathode with pulse lengths on the order of 10 ps.

While the non-linear processes of multi-photon emission and electron heating have been the focus of their own individual theoretical investigations (Maxson *et al.* (2017); Bae *et al.* (2018)), their relative strengths are not well understood. Experimentally non-linear effects have been briefly investigated, although many of these investigations were performed under certain experimental conditions that did not allow for a complete measurement of non-linear effects. One such experiment measured multi-photon photoemission from polycrystalline copper (An *et al.* (2018)). However these measurements only investigated multi-photon emission at negative excess energies and did not investigate the non-linear effects above threshold that emerge at high laser fluences. Another experiment measured the emittance of two-photon photoemission from polycrystalline copper in a UED beamline using the waist scan technique (Pasmans *et al.* (2016)). In this work measurements were taken at a single positive excess energy and across a large range of laser fluences. By varying the laser fluence they observed a transition from single- to two-photon photoemission with increasing fluence. However these higher laser fluences extracted large charge densities which lead to space charge effects. Hence it was not possible to clearly distinguish what

portion of the emittance growth was due to two-photon emission or due to space charge effects. Lastly, an experiment was performed which was the prelude to this investigation (Knill *et al.* (2021)). In this work the MTE of non-linear photoemission from a single crystalline Cu cathode coated in a layer of oxide was measured for a 130 fs laser pulse length. All the above measurements were performed for short 100 fs scale lase pulses. Photoinjectors often use longer 10 ps scale laser pulses followed by bunch compression to mitigate effects of space charge. Theoretically, longer pulse lengths are expected to reduce the probability of non-linear emission and mitigate its effects on MTE. However, this regime has never been studied experimentally with regards to effects on MTE.

In this chapter we experimentally investigate the contribution that non-linear photoemission effects have on the MTE of a graphene coated Cu(110) single crystal over a wide range of laser fluences, excess energies and laser pulse lengths. We use this data to extrapolate the results to realistic photoinjector fluence and charge density conditions for a range of laser pulse lengths from 130 fs to 10 ps. In Sec. 3.3 we describe the experimental setup. In Sec. 3.4 we present detailed measurements that were performed. In particular we present measurements of MTE at positive and negative excess energies, at a variety of laser fluences, and at laser pulse lengths of 130 fs, 1 ps, and 10 ps to investigate the impact that these various parameters have on non-linear photoemission. In addition we present measurements of the total energy and transverse momentum distributions in order to provide deeper insights into the photoemission process. Lastly, in Sec. 3.5 we discuss an extrapolation technique that allows us to obtain the affects that non-linear photoemission has on MTE at charge densities relevant to photoinjectors. Our results show that non-linear effects play a dominant role when trying to reduce the MTE by lowering the excess energy, and that high QE photocathodes will be essential for mitigating these effects.

3.3 Experimental Setup

For this work a graphene layer was grown on a commercially purchased Cu(110) single crystal according to the recipe found in Knill *et al.* (2023). After growth the cathode was transported in air into our UHV analysis chamber for surface and photoemission measurements. The UHV chamber has a base pressure of 2×10^{-10} torr. The sample was annealed to 345°C for 2 hours to produce a well ordered atomically clean surface of graphene coated Cu(110) as evidenced by low-energy-electron-diffraction (Knill *et al.* (2023)).

The energy and transverse momentum distributions were measured using a time-of-flight based analyzer (Karkare *et al.* (2019)). It consists of the photocathode and a delay-line detector arranged in a parallel plate configuration and separated by ~ 4 cm. A short laser pulse is focused down to a sub-50 μm spot size on the photocathode and the emitted electrons are accelerated towards the detector by a voltage of 72 V. The relatively large accelerating voltage of 72 V compared to the 4 V used for previous high resolution studies is essential to measure the large MTE contributions from multi-photon effects. However, this causes the energy resolution of the measurement to be worse than 100 meV (Karkare *et al.* (2019)). The delay-line detector measures the time of flight of the electrons as well as their x and y positions on the detector. From that the transverse and longitudinal energies and momenta can be calculated. The delay-line detector can detect at most one electron per pulse, and so neutral densities filters are used to reduce the incident laser power and ensure that we are operating within that regime. While this step is necessary for the correct operation of the delay-line detector, it also ensured that our measurements are free of any space charge effects.

Tunable wavelength UV light was generated using an optical parametric amplifier

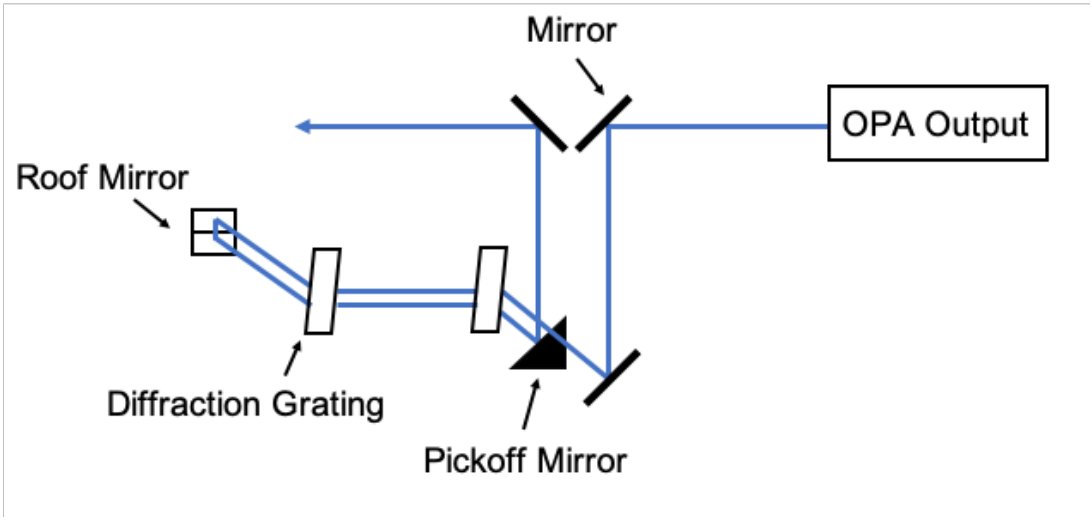

Figure 3.1: The Schematic of an In-house Pulse Stretcher That Was Built Using a Pair of Transmission Diffraction Gratings. By Fixing One Diffraction Grating and Moving the Other We Can Set the Correct Distance According To Eq. 3.4, and Stretch the Pulse to Lengths Ranging from 1 and 10 ps for Photon Energies Between 3.70 eV and 4.77 eV.

(LightConversion ORPHEUS) pumped by a 130-fs-pulse-width 500 kHz repetition-rate laser (LightConversion PHAROS). The sample was irradiated with photon energies ranging from 3.70 eV to 4.35 eV. The laser is p polarized and is incident at an angle of 50° with respect to the normal, and it was focused down to a spot size between 30 μm and 40 μm. While the spot size changed slightly, the location of the electron emission on the sample remained the same. MTE measurements were performed at 130 fs, which is the natural pulse-width of the laser, as well as at the stretched pulse lengths of 1 ps and 10 ps. The spot size was measured using a beam profiler used as a virtual cathode for all pulse lengths and photon energies. This spot size along with the pulse energy was used to calculate the fluence. All spot sizes quoted in this chapter are measured as full width half max.

The pulse was stretched from from 130 fs to 1 ps and 10 ps using a pair of transmission diffraction gratings (Akturk *et al.* (2006)) as shown in the schematic in Fig 3.1. The diffraction gratings are made from fused silica and have an efficiency between 70% and 90% in our operating photon energy range (Ibsen (2022)). This gives the pulse stretcher an overall efficiency of 15% to 39% in our photon energy range. From the schematic in Fig 3.1 it can be seen that the laser is diverted from its original path and sent to the pulse stretcher where it passes through the first diffraction grating whose position is fixed. After it passes through the first diffraction grating it is directed towards the second grating which is mounted to a 50 cm linear translator stage. The linear translator sets the distance between the two diffraction gratings so that the desired pulse length can be achieved for a wide range of photon energies according to:

$$L = \tau \cdot \frac{c[1 - (10^{-6}d \cdot \lambda - \sin\,\alpha)^2]^{3/2}}{2(10^{-6}d)^2\lambda \cdot \Delta\lambda} \tag{3.4}$$

where L is the distance between diffraction gratings, τ is the pulse length of the stretched pulse, d is the line density, λ is the center wavelength of the laser, $\Delta\lambda$ is the bandwidth, α is the angle of incidence, and c is the speed of light (Zhong *et al.* (2020)). After passing through the second diffraction grating the beam hits a roof mirror which sends the beam back through both diffraction gratings at a slightly lower height. At this lower height the beam hits the pickoff mirror and exits the pulse stretcher and continues on its original path. The pulse duration was measured with a commercial autocorrelator (APE (2023)) and the measured pulse length matched the expected pulse length calculated from Eq 3.4.

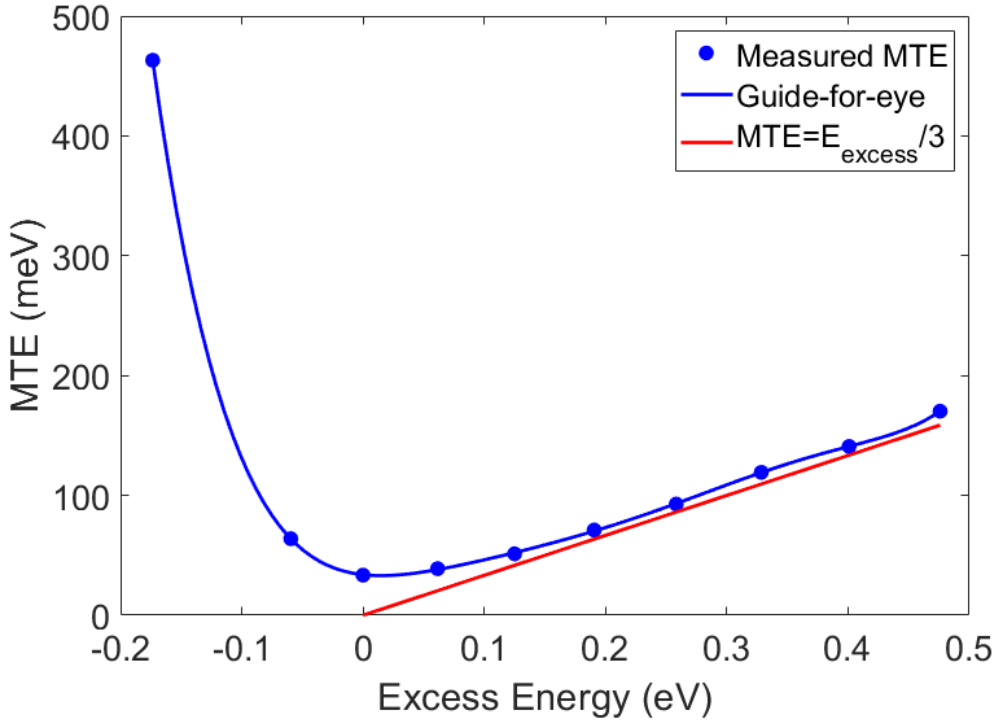

Figure 3.2: Measured Data Points for a 130 fs Pulse Length with a Line That Is Included as a Guide for the Eye. At Large Excess Energies, the Emission Process Is Dominated by Single-photon Emission and the MTE Is Roughly Equal to $E_{excess}/3$. At Negative Excess Energies the MTE Increases Significantly Due to Non-linear Photoemission Effects. The Error in the Measurement Was Estimated to Be 10%.

3.4 Experimental Results

The data was collected with photon energies ranging from 3.70 eV to 4.35 eV for 130 fs, 1 ps, and 10 ps pulse lengths. The QE and MTE measurements in the linear regime show the experimental work function of this photocathode to be 3.88 eV. With this work function the photon energy range of 3.70 eV to 4.35 eV corresponds to -0.18 eV to 0.47 eV of excess energy. In this section we present the MTE, QE and energy distribution measurements at various photon energies and fluences for the 3 pulse

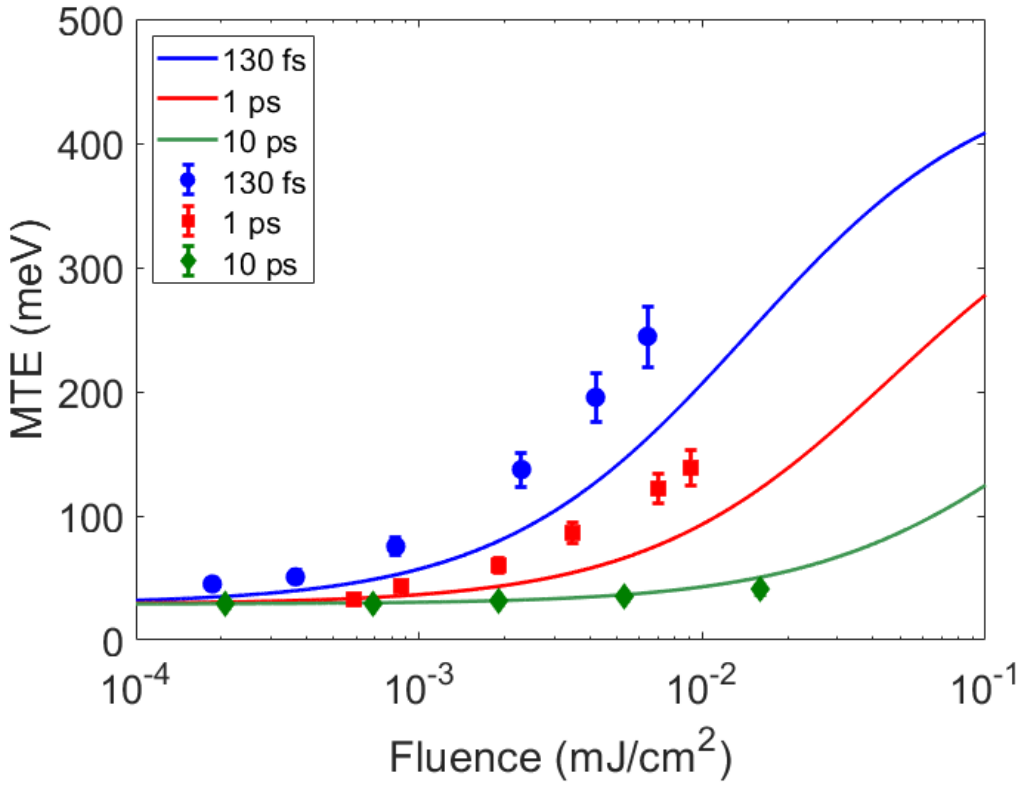

Figure 3.3: Measured Data Points at -0.06 eV Excess Energy for 130 fs, 1 ps, and 10 ps Pulse Lengths. At This Excess Energy You See a Significant Increase in MTE for the Shorter Pulse Lengths Due to Non-linear Effects. While the Increase at the Longer 10 ps Pulse Length Is Only a Few meV. Furthermore the Increase in MTE Appears Quadratic Indicating That the MTE Is a Function of the Square of Laser Fluence as Expected. The Solid Lines Are Obtained from the Extrapolation Technique Described In Sec. 3.5. From This Plot We See That Our Extrapolation Technique Provides a Lower Limit on The MTE. The Error in the Measurement Was Estimated to Be 10%.

lengths.

3.4.1 Mean Transverse Energy

Figure 3.2 shows MTE measurements taken between -0.18 eV excess energy and 0.47 eV excess energy for a 130 fs pulse length at a small enough fluence to keep the emission above threshold fully linear. From this plot we see that the minimum MTE occurs at zero excess energy which corresponds to the photoemission threshold of 3.88 eV. For excess energies between between 0.2 eV and 0.476 eV the MTE is approximately equal to one-third of the excess energy as predicted by Eq. 3.3. As the positive excess energy approaches 0 eV the MTE begins to deviate from Eq. 3.3 as it gets limited by the thermal limit to 25 meV. Below the photoemission threshold the MTE increases dramatically as the non-linear photoemission effects begin to dominate the MTE.

In order to investigate the impact that a changing laser fluence has on non-linear photoemission effects, detailed measurements were performed right below the photoemission threshold for various laser fluences. At -0.06 eV excess energy we can observe a transition between photoemission dominated by single-photon emission from the tail of the Fermi-Dirac distribution, to photoemission dominated by non-linear effects. Figure 3.3 shows our measured data for the three pulse lengths at laser fluences between 10^{-4} mJ/cm^2 and 10^{-1} mJ/cm^2. For the 130 fs pulse length we see that the MTE begins to increase at 10^{-4} mJ/cm^2 due to non-linear effects, and that it increases by an order of magnitude at 10^{-2} mJ/cm^2 laser fluences. For the 1 ps data the non-linear effects begin to impact the MTE at 10^{-3} mJ/cm^2, and at 10^{-2} mJ/cm^2 the MTE is roughly a factor of 2 smaller than the 130 fs data. At 10 ps pulse lengths the MTE only begins increasing slightly at 10^{-2} mJ/cm^2. As the delay-line-detector cannot measure more than one electron per shot, we are unable to perform any direct

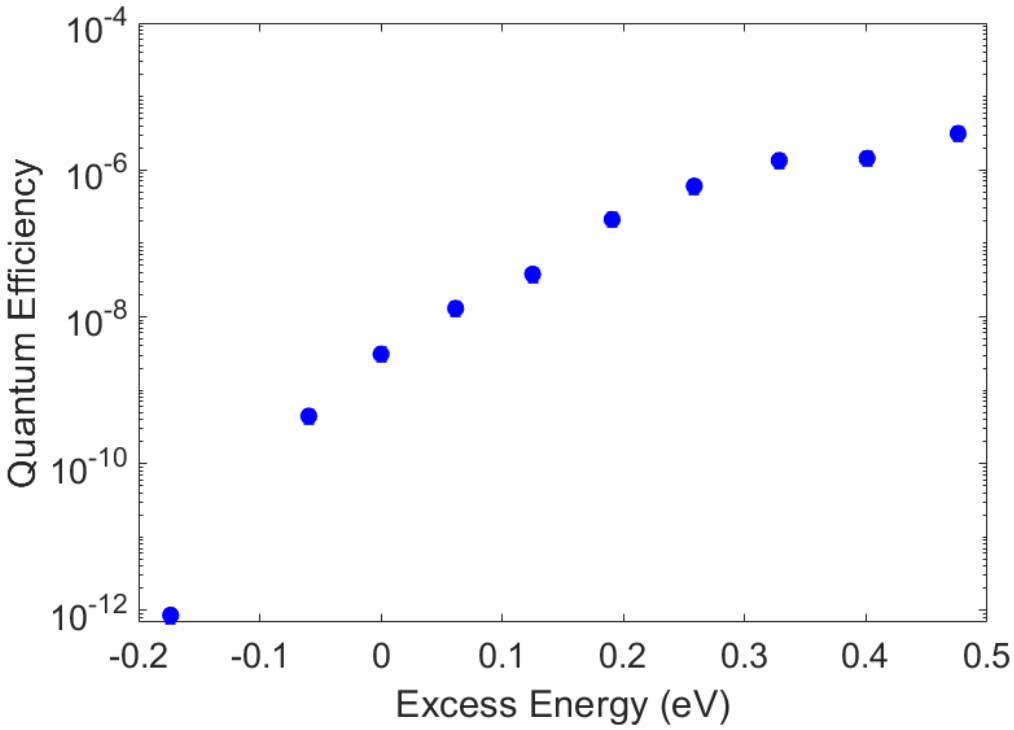

Figure 3.4: Measured Quantum Efficiency for 130 fs. The Current Was Measured from Electron Counts on the Detector and Therefore Represents Only a Fraction of the Actual Current Emitted. Hence the Measured QE Is Some Unknown Factor, on the Order of Unity, Lower than the Actual QE. The Error in the Measurement Was Estimated to Be 20%.

measurements beyond this laser fluence.

3.4.2 Quantum Efficiency

Figure 3.4 shows the measured QE that corresponds to the data points from Fig. 3.2. For this experiment the QE is determined by treating each count measured by the detector as one electron. The detector efficiency may be less than one and hence this is only a lower estimate of the QE. From previous calibrations we expect the detector efficiency to be a large fraction and hence the QE measurement is still

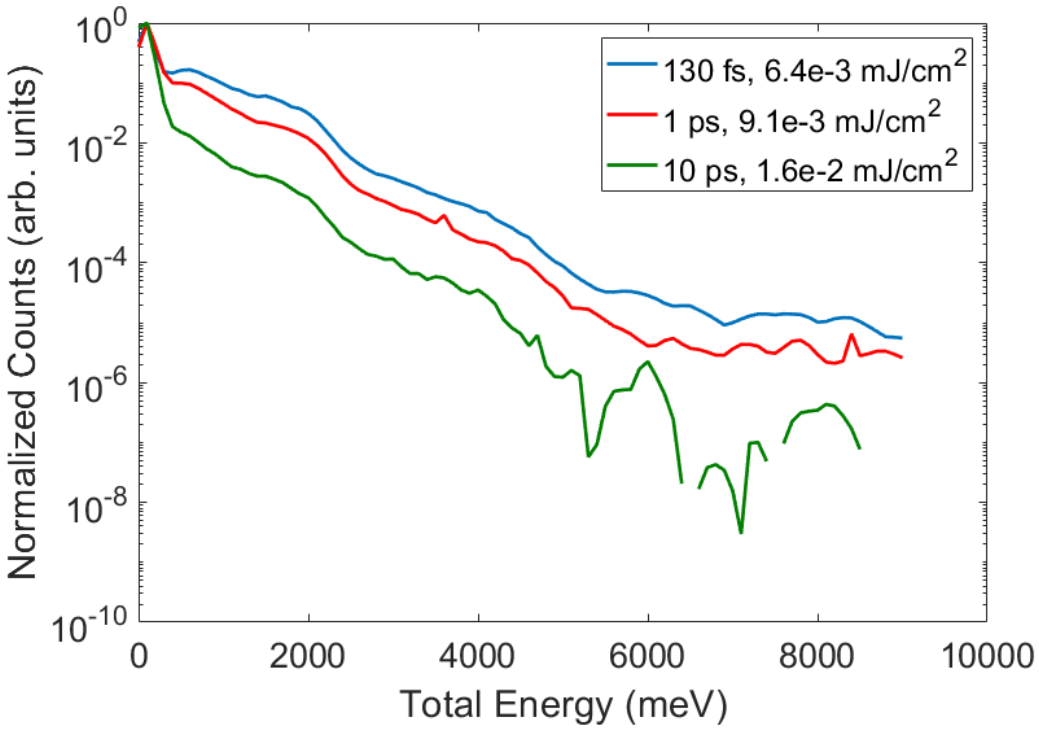

Figure 3.5: Total Energy Distribution at 325 nm (-0.06 eV Excess Energy) for 130 fs, 1 ps, and 10 ps. For the 10 ps Data We See That Multi-photon Emission Is Significantly Reduced and the Number of Electrons Emitted from a Single Photon Is Increased. This Reduction of Multi-photon Emission Shows That Multi-photon Emission Can Be Significantly Mitigated by Operating at 10 ps Pulse Lengths.

accurate within the order of magnitude. From Fig. 3.4 we see that the QE is 10^{-9} at zero excess energy. This QE is very low compared to other metal photocathodes like bare polycrystalline copper which often exhibit a QE of 10^{-7} at zero excess energies (Dowell *et al.* (2006)). All values presented in Fig. 3.4 are measured keeping the fluence small enough to be in the linear range.

3.4.3 Total Energy Distribution

Figure 3.5 shows the normalized total energy distribution for the three different pulse lengths at a photon energy of 3.82 eV (excess energy of -0.06 eV). These total energy curves correspond to the largest fluence measurements from Fig. 3.3 for each pulse length. This corresponds to a fluence of 6.4×10^{-3} mJ/cm^2 for the 130 fs curve, 9.1×10^{-3} mJ/cm^2 for the 1 ps curve, and 1.6×10^{-2} mJ/cm^2 for the 10 ps curve. The initial drop from 0 to $\sim$100 meV corresponds to single-photon emission from the Fermi tail. As expected this initial drop is largest for the 10 ps data which indicates that the fraction of electrons emitted via single-photon emission is largest for 10 ps. From 100 meV to 4000 meV we see two-photon emission for all three pulse lengths. Around 2000 meV we see a similar feature in all three curves. Looking at the density of states of Cu, there is an increased number of electrons at -2000 meV corresponding to the d-band (Bunau and Joly (2009)). Hence it is possible that this feature at 2000 meV can be attributed to the d-band. Beyond 4000 meV we see the presence of three-photon emission for the 130 fs and 1 ps data while the 10 ps shows mostly noise. Comparing the three curves we see that the drop between 130 fs and 1 ps is significantly smaller than the drop between 1 ps and 10 ps suggesting a significant change in the photoemission process at the 10 ps time scales.

3.4.4 Transverse Momentum Distribution

Figure 3.6 shows the $k_x = 0$ slice of the energy integrated transverse momentum distribution on a log scale for the same photoemission conditions shown in Fig. 3.5. All three curves fall sharply till 0.25 1/Å, beyond which the emission is dominated by the two-photon process. The sharp drops beyond 0.25 1/Å correspond to the emission of d-band electrons and the three-photon process respectively just like in Fig. 3.5.

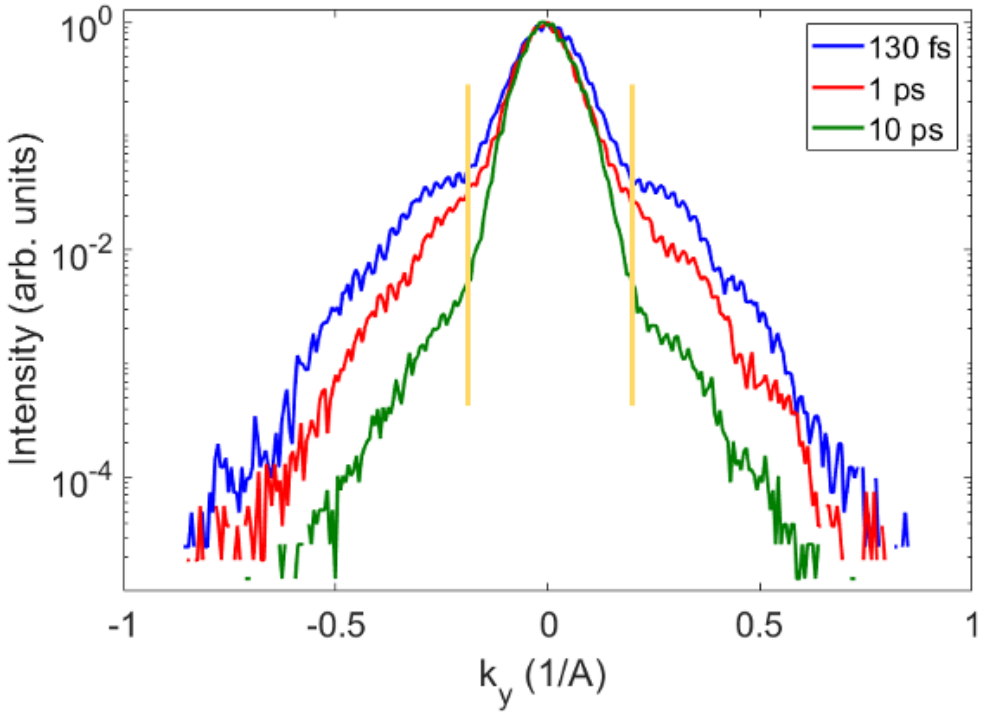

Figure 3.6: The $k_x = 0$ Slice of the Energy Integrated Transverse Momentum Distribution on a Log Scale for 130 fs, 1 ps, and 10 ps under the Same Photoemission Conditions as Shown In Fig. 3.5. Between 0 1/Åand The Yellow Vertical Lines We See the Presence of Single-Photon Emission. Beyond the Yellow Vertical Lines We See the Presence of Multi-Photon Emission and Emission From the D-band. The Small Wiggles In the Curves Are an Artifact of a Mesh Grid Placed at the Entrance of the Detector.

3.5 Extrapolation Method

While the data presented in the previous section gives a much needed starting point for the contribution of non-linear photoemission on the MTE, it does not provide us measurements at laser fluences and excess energies that are typically used in photoinjectors. For that we would need to measure the MTE at laser fluences between 0.1 mJ/cm^2 and 4 mJ/cm^2 and at excess energies in the range of 0-1 eV. However for the smallest laser spot size achievable in the energy analyzer, this range of fluence and excess energies leads to more than one electron being emitted per shot and hence cannot be measured by the delay-line detector. Hence, to estimate the MTE in the fluence and excess energy range typically used in photoinjectors, we have used the measurements presented in section 3.4 and devised an extrapolation scheme based on the extended Fowler-Dubridge theory.

From the extended Fowler-Dubridge theory for non-linear photoemission, the total photo-current density can be expressed as a sum of the partial current densities for n-photon emission (J_n) according to the following relation:

$$J = \sum_{n=0}^{\infty} J_n = \sum_{n=0}^{\infty} \sigma_n I^n \tag{3.5}$$

where J is the total photo-current density, σ_n is the expansion coefficient, I is intensity of the irradiating laser, and n is an integer corresponding to n-photon emission (Ferrini *et al.* (2009)). For our extrapolation we have considered only single- and two-photon emission and represented the MTE as a sum of partial MTEs. With such an extrapolation the MTE can be given as a function of the fluence F as:

$$\mathrm{MTE} = \frac{1}{N}\left(\frac{N_L \cdot \mathrm{MTE}_L}{F_L/F} + \frac{N_{NL} \cdot \mathrm{MTE}_{NL}}{(F_{NL}/F)^2}\right) \tag{3.6}$$

where $N_{L,NL}$ is the number of electron counts per second, $\mathrm{MTE}_{L,NL}$ is the MTE, $F_{L,NL}$ is the laser fluence, and the subscripts L and NL represent the linear and

non-linear contributions respectively. N is calculated according to:

$$N = \frac{N_L}{F_L/F} + \frac{N_{NL}}{(F_{NL}/F)^2} \tag{3.7}$$

Since linear emission does not change significantly across the three pulse lengths, we have taken one data set that was collected at 130 fs and used it as the linear contribution for all three pulse lengths. For the non-linear contribution we have taken measurements at -0.18 eV excess energy for each pulse length. The specific linear and non-linear data sets used are shown in Table 3.1.

This extrapolation technique assumes that the contribution of non-linear effects to the MTE does not change significantly from -0.18 eV to other excess energies, and does not change significantly at laser fluences larger than 10^{-2} mJ/cm^2. Our technique also assumes only 2nd order photoemission effects and ignores any high order effects as well as the effects of electron heating. Due to these assumptions, our extrapolation technique only provides a lower limit for the MTE.

Table 3.1: A Table Showing the Data Used in the Extrapolation Technique. The Data Set Titled "Linear" Is Used in the Extrapolation for All Three Pulse Lengths As the Linear Contribution. While the Non-linear Contributions Are Titled "130 fs", "1 ps", And "10 ps" For the Respective Pulse Lengths.

Data	MTE (meV)	N (counts/s)	F (mJ/cm^2)
Linear	29	850	1.9e-4
130 fs	463.12	6700	4.6e-3
1 ps	394.87	14000	1.2e-2
10 ps	306.55	2000	7.3e-3

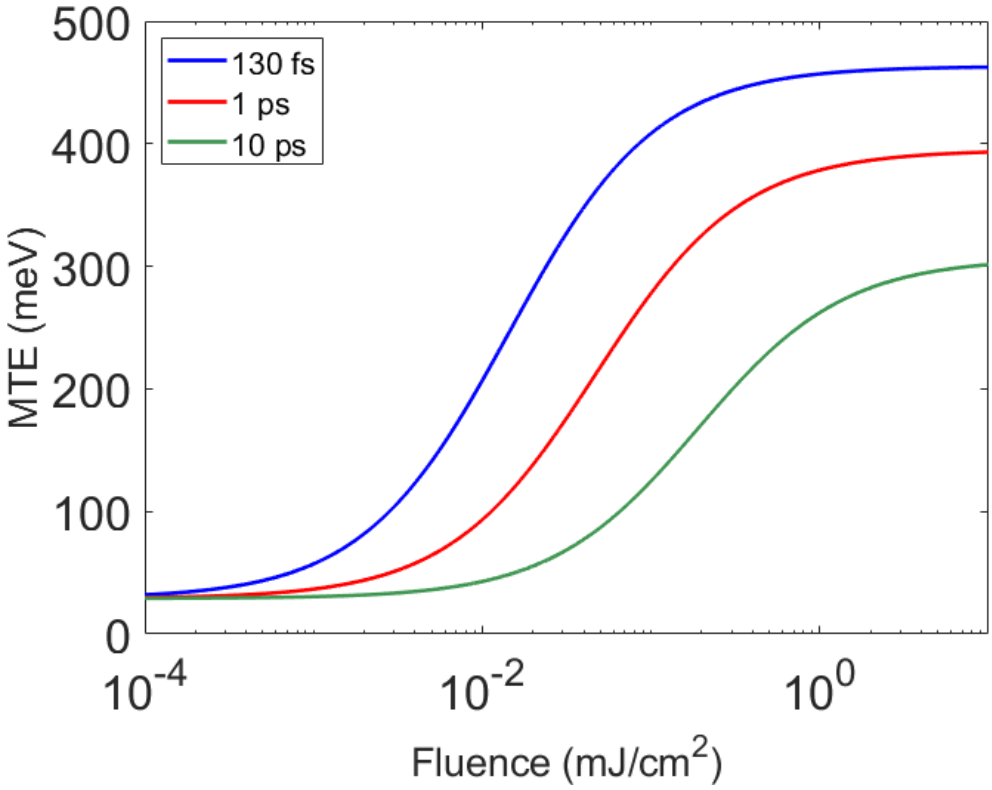

Figure 3.7: MTE vs Fluence Curves for 130 fs, 1 ps, and 10 ps Pulse Lengths Calculated From Eq. 3.6. Although the Curves Plateau at Higher Fluences, This is an Artifact of Not Including Beyond 2nd Order Photoemission in the Extrapolation Technique. In Practice We Would Expect the Curves to Continue Rising with Fluence Due to 3rd Order, and Higher, Photoemission Effects.

3.5.1 Mean Transverse Energy and Laser Fluence

In order to check the accuracy of our extrapolation we have compared it with our measured data as shown in Fig. 3.3. We can see that the extrapolation curves are in good agreement with the measured data for all the pulse lengths. In addition we see that all extrapolated values are smaller than the measured data. This is expected because the extrapolation only gives a lower limit for the MTE.

Figure 3.7 shows the extrapolation over the 10^{-4} mJ/cm^2 to 10^{0} mJ/cm^2 fluence range. We see that non-linear effects begin to contribute to the MTE at laser fluences as low as 10^{-4} mJ/cm^2 for 130 fs pulse lengths and at 10^{-2} mJ/cm^2 for 10 ps pulse lengths. This is as expected since the two orders of magnitude difference between pulse lengths is compensated by the two orders of magnitude difference in laser fluence. Lastly, we see in Fig. 3.7 that at higher fluences the curves begin to plateau. This is a limitation of the extrapolation due to considering only effects of 2nd order photoemission and ignoring higher order emissions and not something we expect to occur at these higher laser fluences. Instead we expect the MTE to continue to rise as the laser fluence increases.

3.5.2 Mean Transverse Energy and Charge Density

While the above plots provide us with some insight into the fluence range where non-linear effects begin to impact the MTE, we are more interested in the MTE we can expect at various charge densities that are relevant to photoinjectors. In particular we want to identify the ideal operating excess energy that results in the minimum MTE for a given charge density per bunch. For that we have calculated the charge density as a function of the fluence (F) and excess energy as:

$$\mathrm{CD} = \frac{N \cdot q}{A \cdot f} \tag{3.8}$$

where N is the number of electrons calculated from Eq. 3.7, q is the charge of the electron, A is the emission spot area, and f is the repetition rate of our laser (500 kHz). In this case we used the data from Fig. 3.3 for positive excess energies as the linear contribution to Eq. 3.6. Then we plotted the extracted charge density and MTE as a function of the fluence for various excess energies. By checking over all of the measured excess energies we were able to identify the minimum MTE that we can

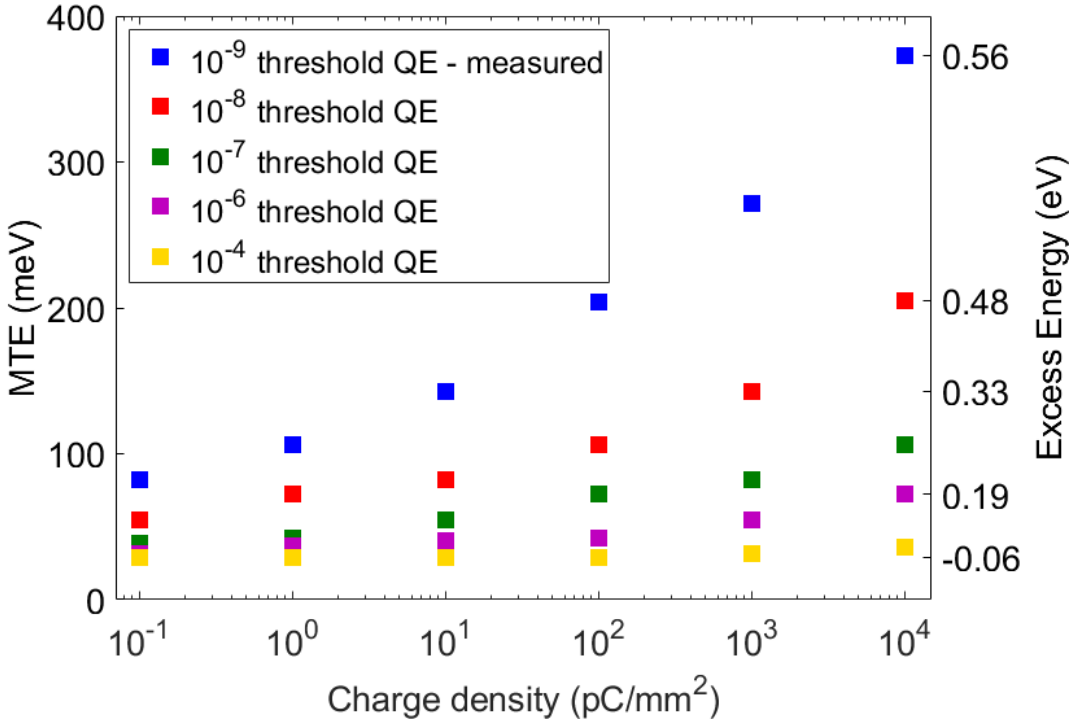

Figure 3.8: Minimum Contribution to the MTE From Non-linear Effects as Calculated From Eq. 3.8 for Charge Densities Ranging From 10^{-1} and 10^{4} pC/mm^2 For a 130 fs Pulse Length. The Calculation Was Performed for the Measured QE Data as Well as Higher QEs.

expect for a given charge density, and the excess energy where this minimum occurs.

The plots in Fig. 3.8, Fig. 3.9, and Fig. 3.10 show the minimum MTEs at various charge densities for pulse lengths of 130 fs, 1 ps, and 10 ps respectively. They also give the excess energy at which the minimum occurs on the right y-axis. These three plots also show curves for the minimum MTE obtained by scaling the measured linear QE by 10 to 10^5 times. We plot this for charge density ranges that are often used in DC and RF photoinjectors.

From Fig. 3.8, Fig. 3.9, and Fig. 3.10 we see that for for all three pulse lengths the measured 10^{-9} QE data set has an MTE that increases significantly with increasing

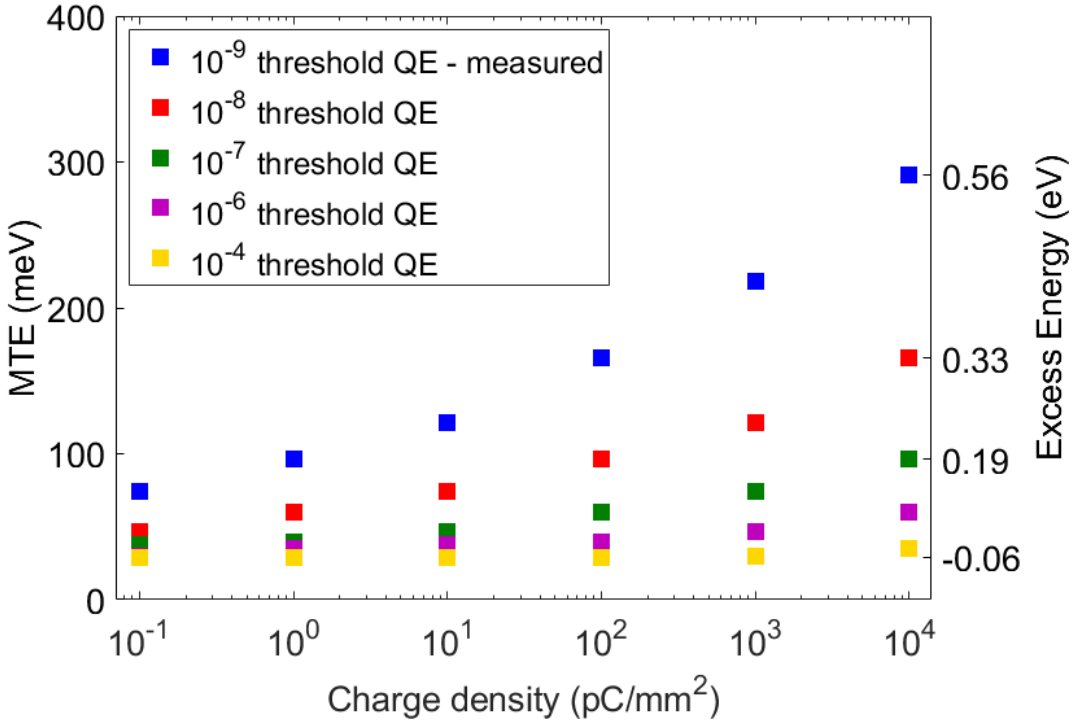

Figure 3.9: Minimum Contribution to the MTE From Non-linear Effects as Calculated From Eq. 3.8 for Charge Densities Ranging From 10^{-1} and 10^{4} pC/mm^2 For a 1 ps Pulse Length. The Calculation Was Performed for the Measured QE Data as Well as Higher QEs.

charge density. We also see that for all charge densities the minimum MTE occurs at excess energies greater than 0.19 eV. This shows that for very low QE photocathodes there needs to be a balance between contributions to the MTE from excess energy and from non-linear effects in order to achieve the minimum MTE at these charge densities. Furthermore we see that the minimum MTE is approximately a factor of 2 larger than the thermal limit at 10^{-1} pC/mm^2 for all three plots. Hence our measured 10^{-9} QE data set is not suitable for operating at these high charge densities and is really only suitable for applications that require single-to-few electrons per pulse.

In general the 10^{-9} QE, 10^{-8} QE, and 10^{-7} QE data sets correspond to QEs of

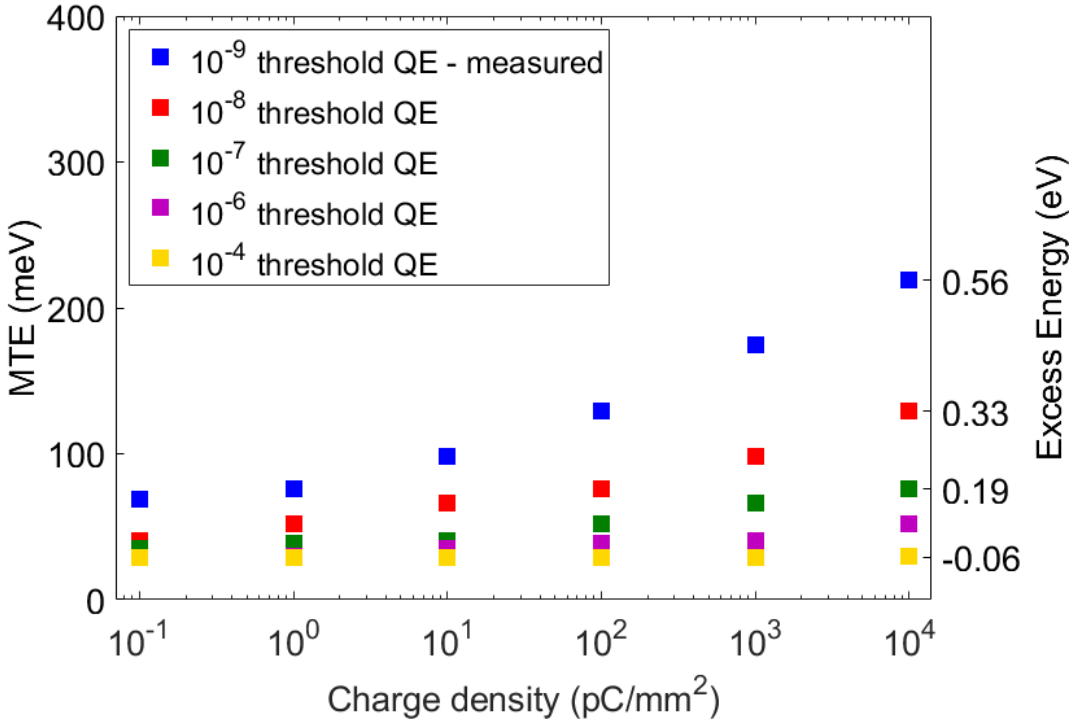

Figure 3.10: Minimum Contribution to the MTE From Non-linear Effects as Calculated From Eq. 3.8 for Charge Densities Ranging From 10^{-1} and 10^{4} pC/mm^2 For a 10 ps Pulse Length. The Calculation Was Performed for the Measured QE Data as Well as Higher QEs.

metallic photocathodes. While the 10^{-9} QE and 10^{-8} QE data sets show a significant increase in MTE at high charge densities, at 10^{-7} QE we see that it is possible to obtain sub-100 meVs even at these high charge densities for all three plots.

Looking at the 10^{-4} QE data in all three plots we see that for the entire range of charge densities the minimum MTE is at or near the thermal limit of 25 meV and the excess energy is near zero. This indicates that there is no contribution to the MTE from non-linear photoemission effects. Therefore to achieve MTEs near the thermal limit at charge densities as high as 10^{4} pC/mm^2 it is essential high QE photocathodes like low-electron affinity semiconductors are used.

3.6 Conclusion

In conclusion we present MTE measurements of non-linear photoemission from a graphene coated Cu(110) photocathode above and below the photoemission threshold for pulse lengths of 130 fs, 1 ps, and 10 ps. Our results show that for a given laser fluence, the contribution to the MTE from non-linear effects can be significantly reduced by using longer pulse lengths. At longer pulse lengths the total energy and transverse momentum distributions show that the fraction of electrons emitted via single-photon emission is significantly larger in comparison to shorter pulse lengths. In addition we extrapolate our data to identify the minimum MTE that can be achieved at charge densities ranging from 10^{-1} to 10^{4} pC/mm^2 for QEs ranging from 10^{-9} to 10^{-4} at the photoemission threshold. We see that when using lower QE photocathodes to obtain high charge densities, a balance between non-linear effects and excess energy is necessary in order to achieve the minimum MTE. In addition we see that low MTEs near the thermal limit are not attainable in this range and hence these low QE photocathodes are only practical for single-to-few electron per pulse applications. For photocathodes with QEs greater than 10^{-7} at threshold we see that while a balance must be found between non-linear effects and excess energies, sub-100 meV MTEs can be attained at all charge densities. Lastly, for photocathodes with QEs greater than 10^{-4} at threshold we see no significant contribution to the MTE from non-linear effects for all pulse lengths and charge densities. Hence is essential that high QE photocathodes like low-electron affinity semiconductors are used for high charge density applications.

Chapter 4

PHOTOCATHODE AND BRIGHT BEAMS LABORATORY

4.1 Abstract

The performance of linear accelerator applications like X-ray free electron lasers (XFELs) and ultrafast electron diffraction (UED) and microscopy (UEM) experiments is determined by the brightness of the electron beam. For linear accelerators the electron beam is never brighter than it is at the emission source, or photocathode. Hence identifying photocathode materials that generate the brightest possible electron beams is critical to the advancement of linear accelerator technology. In this chapter we present an introductory review of photocathode materials as well the factors that limit the brightness of electron beams. In addition we present the research capabilities of the recently commissioned Photocathode and Bright Beams Lab (PBBL) at Arizona State University (ASU). The PBBL has been designed to be a comprehensive photocathode research facility equipped to tackle many outstanding challenges in photocathode characterization and development.

4.2 Introduction

The brightness of ultrafast electron beams generated by a photoinjector play a critical role in determining the performance of linear accelerator applications like X-ray free electron lasers (XFELs) (Akre *et al.* (2008); Emma *et al.* (2010)) and ultrafast electron diffraction (UED) (Ruan *et al.* (2001); Siwick *et al.* (2002); Ischenko *et al.* (2017)) and microscopy (UEM) (Lobastov *et al.* (2005); Armstrong *et al.* (2007)) experiments. For XFELs the beam brightness limits the ability to lase at higher photon

energies and with higher X-ray pulse energies (Ferrario (2015)). For example the proposed Linear Coherent Light Source II High Energy Upgrade (LCLS II-HE) at Stanford Linear Accelerator Center (SLAC) will produce X-ray energies above 5 keV. By increasing the electron beam brightness by a factor of 10, or a factor of 3-4 reduction of normalized transverse emittance, the LCLS II-HE could reach X-ray energies of 20 keV (DOE (2016)). These hard X-rays are necessary for producing real time movies of various chemical and biological processes as well as probing the electronic and atomic structure of materials (Minitti *et al.* (2015)). In addition increasing the beam brightness is essential to the development of smaller university-scale XFELs (Rosenzweig *et al.* (2020)). The LCLS is on average 400% oversubscribed and therefore the development of university-scale XFELs will greatly improve the accessibility of these devices to users who do not require the maximum X-ray energies produced by the LCLS (SLAC (2012)).

UED and UEM experiments can be classified into two main operating modes: single-shot mode and stroboscopic mode. Single-shot mode utilizes a large number of electrons to probe irreversible processes in materials and biology. For single-shot experiments increasing the electron beam brightness can increase the transverse coherence length without compromising the signal-to-noise ratio, thus enabling the study of larger lattice sizes (Musumeci *et al.* (2010)). For example existing single-shot experiments have a small electron transverse coherence length which limits the study of crystals with $\sim$1 nm lattice sizes. By increasing the beam brightness, we can investigate lattice sizes that are several nm long like proteins and macromolecular assemblies. In addition, one can access correlation lengths of longer than 1 nm in materials if the coherence length of the electron beam is longer than the correlation length. Stroboscopic mode uses single-to-few electrons per pulse with high repetition rates to probe a wide range of processes like laser-induced phase transitions (Grinolds *et al.*

(2006)), magnetization dynamics (Silva *et al.* (2018)), and reversible morphological changes to thin films (Barwick *et al.* (2008)). Stroboscopic mode offers an advantage in that the small number of photo-electrons results in negligible coulomb repulsion, known as space charge effects, which allows for both atomic-scale spatial resolution and sub-ps temporal resolution (Aseyev *et al.* (2020)). For these stroboscopic mode applications, an increase in beam brightness will reduce the data acquisition time as well as increase the signal relative to the noise (Ji *et al.* (2019)).

High brightness electron sources are also of importance to particle colliders used for nuclear physics and high energy physics applications (Filippetto *et al.* (2022)). Brighter electron sources can result in novel ways of efficiently cooling hadron beams using electrons, and enable higher luminosity and cheaper designs of high energy electron colliders.

In general the brightness of an electron beam characterizes the phase space density of the electron beam and is represented by:

$$B_{6D} \propto \frac{N}{\epsilon_x \epsilon_y \epsilon_z} \tag{4.1}$$

where N represents the total number of electrons which ranges from 1 to 10^{10} depending on the application, and $\epsilon_{x,y,z}$ is the emittance and it describes the RMS area of the electron beam in the x-, y-, and z-planes of the phase space. For the linear accelerator applications described above the electron beam is never brighter than it is at the source, or photocathode. Hence maximizing the beam brightness from the photocathode is essential to generating the highest quality electron beam. For the majority of applications the transverse and longitudinal emittances are decoupled and the 4D beam brightness given by:

$$B_{n,4D} = \frac{m_e c^2 \epsilon_0 E}{2\pi \mathrm{MTE}} \tag{4.2}$$

becomes an important figure of merit (Musumeci *et al.* (2010)). For high charge density applications like XFELs and single-shot UED/UEM experiments the maximum charge density that can be extracted is limited by the accelerating electric field E at the cathode surface, and hence the maximum possible 4D beam brightness scales according to the following relation:

$$B \propto \frac{E^n}{\mathrm{MTE}} \tag{4.3}$$

Here, MTE is the mean transverse energy of the emitted electron and can be related to the normalized transverse emittance as:

$$\epsilon_x = \sigma_x \sqrt{\frac{\mathrm{MTE}}{m_e c^2}} \tag{4.4}$$

where σ_x is the RMS emission area, m_e is the mass of the electron, and c is the speed of light.

For low charge density applications like stroboscopic UED and UEM the number of photoemitted electrons is small and hence the repulsive force is negligible compared to the force of the applied field. For such applications the brightness at the photocathode is inversely proportional to the square of the intrinsic emittance of the photocathode (ϵ_x) (Musumeci *et al.* (2018)). Thus, for such applications, brightness can be increased by reducing the emission area (often limited by the diffraction limit of the laser spot size) or reducing the MTE.

For all of the aforementioned linear accelerator applications the key figure of merit in determining the beam brightness is the MTE, and it is equivalent to the temperature of the emitted electrons in the vacuum (Bazarov *et al.* (2009)). Hence a lot of effort has gone into understanding and minimizing the MTE in order to maximize the beam brightness. Several theoretical and experimental investigations have shown that there are a variety of photocathode properties that affect the MTE like the band

structure (Karkare *et al.* (2017)) and surface nonuniformities (Karkare and Bazarov (2015); Feng *et al.* (2017); Gevorkyan *et al.* (2018)), as well as operating parameters like the temperature of the photocathode (Cultrera *et al.* (2015); Feng *et al.* (2015)), the irradiating excess energy (Dowell and Schmerge (2009)), and the laser pulse energy (Maxson *et al.* (2017); Bae *et al.* (2018a)). Thus it is critical that we have a deep understanding of photocathodes and the photoemission process in order to generate the brightest possible electron beams.

In this chapter we present an introductory review of photocathode physics and the factors that limit beam brightness for linear accelerators. With this discussion in mind, we then present the design of the Photocathode and Bright Beams Lab (PBBL) at Arizona State University (ASU). This is a unique photocathode lab that has been built to grow, characterize, and test a wide variety of photocathode materials and technologies for use in current and next generation photoinjectors. The organization of this chapter is as follows. Section 4.3 summarizes several photocathode and photoemission properties that limit the brightness of electron beams. Section 4.4 reviews various photocathode materials and technologies. And in Section 4.5 we present the design and experimental capabilities of the newly built PBBL, as well as some early results coming out of the lab.

4.3 Brightness Limiting Factors

In order to improve the performance of current and next generation linear accelerator sources, it is essential that we have a complete understanding of the factors that impact the electron beam brightness. From Eq. 4.2 and Eq. 4.3 we know that for all photoinjector applications, the key figure in determining the brightness from the photocathode is the MTE. Hence this section largely focuses on factors that affect the MTE and ways of mitigating them. MTE is governed by 4 primary factors: 1.

Excess energy, 2. Surface non-uniformities, 3. Band-structure, and 4. Non-linear photoemission effects. Below we discuss each of these factors in detail:

4.3.1 Excess Energy

Excess energy is defined as the difference between the photon energy and the work function. Typically a fraction of the excess energy is converted into the transverse energy during emission. Thus, usually larger excess energies result in larger MTEs. Exceptions to the rule of thumb can occur during photoemission from single crystal surfaces where effects of band structure (Karkare *et al.* (2017)) and many-body scattering processes (Nangoi *et al.* (2021)) can dominate when the surface is comprised of two or more phases with significantly different work functions (Pierce *et al.* (2021)). The relationship between MTE and excess energy was first identified by Dowell and Schmerge (Dowell and Schmerge (2009)) and explained based on the Spicer's 3 step model. More recently, Saha *et al* proposed a simpler explanation of the relationship (Saha *et al.* (2023a)). Assuming that the electrons upon excitation do not scatter before emission and are distributed uniformly into the free electron parabola, the MTE is given by MTE = $E_{excess}/3$. For small excess energies comparable to the thermal energy k_BT or lower, the MTE gets limited to k_BT due to electrons being emitted from the Fermi tail of the distribution. A general relationship between MTE and excess energy can be given using the following expression:

$$\text{MTE} = k_BT\frac{\text{Li}_3[-\exp(E_{excess})]}{\text{Li}_2[-\exp(E_{excess})]} \tag{4.5}$$

where Li_2 and Li_3 are polylogarithm functions of the 2nd and 3rd order respectively (Vecchione *et al.* (2013)). Figure 4.1 shows the MTE transition from $E_{excess}/3$ to the room temperature thermal limit of 25 meV for a Cu(110) surface coated with graphene (Knill *et al.* (2023b)). This thermal limit has also been demonstrated for

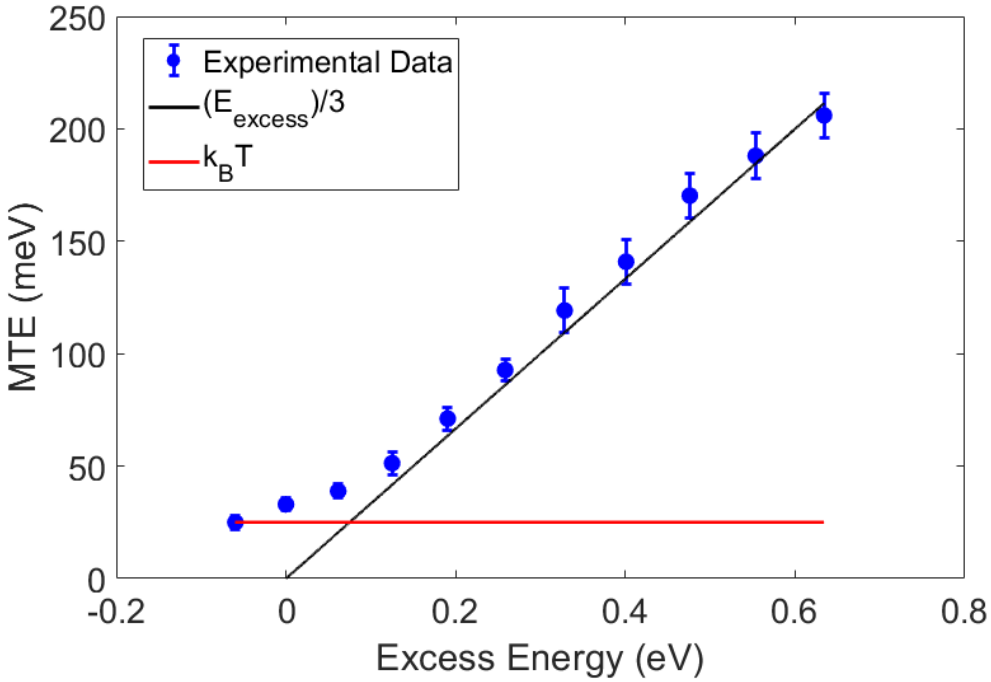

Figure 4.1: Experimental Data from Knill *et al.* (2023b) Compared with MTE = $E_{excess}/3$ and the Thermal Limit at Room Temperature.

the Cu(100) (Karkare *et al.* (2020)) surface and for thin Sb films (Feng *et al.* (2017)).

For small laser fluences sub-25 meV MTEs can be attained by cooling down the photocathode to cryogenic temperatures. Such MTEs have been demonstrated from several systems like 22 meV from thin films of alkali antimonide at 90 K (Cultrera *et al.* (2015)), 5 meV from a Cu(100) single crystal at 30 K (Karkare *et al.* (2020)), and 9 meV from a graphene-coated Cu(110) single crystal at 77 K (Knill *et al.* (2023b)). While these three results represent some of the lowest MTEs ever measured, none of them reached the thermal limit for their respective photocathode temperatures. For the sub-10 meV Cu single crystal measurements, it is suspected that the low transmission probability for low-kinetic-energy electrons near the photoemission threshold is what lead to these MTEs being slightly larger than the thermal limit (Schroeder

and Adhikari (2019); Karkare *et al.* (2020)). For the alkali antimonide thin films, the 22 meV MTE that was measured is significantly larger than thermal limit. In this case it was suspected that the MTE was limited by the surface nonuniformities of physical and chemical roughness due to the polycrystalline surface of the photocathode (Karkare and Bazarov (2015); Feng *et al.* (2017)). However, recent measurements of the work function of Cs_3Sb films show that this higher-than-k_BT-MTE was likely due to a larger excess energy (Saha *et al.* (2023b)). Furthermore, several of these near-threshold measurements have a very low quantum efficiency which will result in increased MTE due to non-linear photoemission effects when extracting large charge densities.

4.3.2 Surface Non-uniformities

The surface non-uniformities of physical roughness and chemical roughness play a significant role in the photoemission process (Karkare and Bazarov (2015)). Physical roughness refers to the nano-scale peaks and valleys that can exist on a photocathode surface. These features lead to localized transverse electric fields that cause the photoemitted electrons to accelerate transversely and therefore increase the MTE. This increase in MTE due to physical roughness ($\mathrm{MTE_{pr}}$) can be given by:

$$\mathrm{MTE_{pr}} = \frac{\pi^2 A^2 E e}{2\lambda} \tag{4.6}$$

where A is the amplitude of the surface roughness, E is the applied accelerating electric field, e is the charge of the electron, and λ is the spatial period of the surface roughness (Feng *et al.* (2017)).

The chemical roughness refers to work function variations that can occur across the surface of the photocathode. This leads to transverse electric field regions between the work function variations which can also increase the MTE. However unlike the

physical roughness, the chemical roughness impact on the MTE decreases with an increasing accelerating field. For sinusoidal work function variations in a high electric field ($E \gg \frac{2\pi\sqrt{2}h}{a}$) the increase in MTE has been modeled by Karkare and Bazarov (Karkare and Bazarov (2015)). This increase in MTE due to chemical roughness ($\mathrm{MTE_{cr}}$) obeys the following relation:

$$\mathrm{MTE_{cr}} = \frac{\pi^2 h^2 e}{4\sqrt{2}aE} \tag{4.7}$$

where h is the amplitude and a is the period of the work function variations (Karkare and Bazarov (2015)). For lower electric fields it remains constant with electric field. Hence the effects of the combined surface nonuniformities on MTE leads to a non-monotonic dependence on the accelerating electric field. One investigation showed that the contribution to the MTE from these combined effects can be calculated using a spectral expansion of electric fields close to the surface and tracking the trajectory of electrons with the results shown in Fig. 4.2 (Gevorkyan *et al.* (2018)). Recently it has been shown that it is possible to obtain a nearly atomic smooth polycrystalline surface of photoemissive Cs_3Sb thin films with negligible contributions to the MTE from surface roughness (Saha *et al.* (2022)). However in order to completely eliminate the contribution to the MTE from surface nonuniformities it is essential that electrons are emitted from atomically ordered single crystalline surfaces (Karkare *et al.* (2017)).

4.3.3 Band Structure

In addition to being free from the MTE-degrading surface nonuniformities, single crystalline photocathodes also benefit from the conservation of transverse momentum during photoemission (Karkare *et al.* (2017)). By selecting photocathode materials which have a band structure that restricts the electron emission to low transverse energy states, we can take advantage of the conservation of transverse momentum

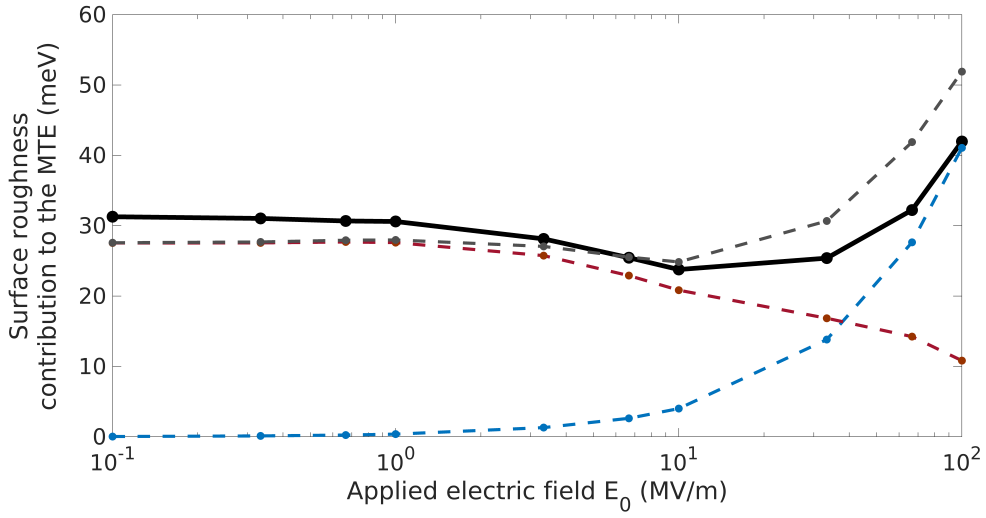

Figure 4.2: Plot Showing the Contributions to the MTE from Surface Roughness (Blue Dashed Line) and Chemical Roughness (Red Dashed Line) as Well as Their Combined Effects (Black Solid Line) at Electric Fields That Can Be Found in Photoinjectors (Gevorkyan *et al.* (2018)).

and emit electrons with smaller MTEs (Musumeci *et al.* (2018)). In general these photocathode materials will have narrow energy dispersion bands with low effective masses localized around the Gamma point in the Brillouin zone.

For example emission from Ag(111) can produce both low MTE and high QE simultaneously due to the low effective mass of the surface state (Karkare *et al.* (2017)). Another investigation in this regard is that of PbTe(111). Here, although the band structure is suitable with the relevant band having a small effective mass as low as $0.02m_e$, it was found that the many-body electron-phonon scattering affects excited electrons into higher transverse momentum states before emission (Nangoi *et al.* (2021)).

4.3.4 Non-linear Photoemission

Multi-photon emission occurs when an electron absorbs more than one photon in order to emit into vacuum, and it can be categorized as below threshold multi-photon emission and above threshold multi-photon emission. Below threshold multi-photon emission occurs at negative excess energies, and therefore the electron needs to absorb at least two photons in order to emit. This is a common experimental technique for pump-probe experiments, whereby an electron is excited into a higher energy state by a photon with energy less than the work function, and then that excited energy state is probed by a second photon which emits the electron.

Above threshold multi-photon emission occurs when high laser fluences are used with positive excess energies near the photoemission threshold. At laser fluences larger than 10^{-4} mJ/cm^2 the photoemission process transitions from purely single photon emission to a mix of single and multi-photon emission (Bae *et al.* (2018a)). While the overall fraction of electrons emitted via multi-photon emission is small, their contribution to the MTE is significant in comparison to single-photon emission. In both above and below multi-photon emission the electrons can be emitted with several eVs of excess energy and will therefore have very large MTEs.

Electron heating, also known as ultrafast laser heating, is an effect that occurs when high laser fluences are delivered by ultrafast (sub-10-ps) laser pulses which causes the temperature of the electron distribution to increase to several thousand Kelvin. At sub-10-ps timescales the electron distribution is thermally isolated from the lattice due to small electron-phonon coupling. The large difference in heat capacities between the electron distribution and the lattice leads to the electron heating effect (Anisimov *et al.* (1974); Elsayad-Ali *et al.* (1987)). It has been shown theoretically that at high fluences and small excess energies this effect plays a large role in

limiting the minimum achievable MTE (Maxson *et al.* (2017)).

Recently there have also been several experimental investigations that measured the impact that non-linear effects have on the MTE and emittance from polycrystalline Cu (Pasmans *et al.* (2016); An *et al.* (2018)) and single crystalline Cu (Knill *et al.* (2021, 2023a)) photocathodes. These experimental and theoretical findings show that non-linear effects make it impossible to utilize low QE metallic photocathodes to obtain sub-25 meV MTEs for high charge density applications. While they showed that non-linear effects can be partially mitigated at longer laser pulse lengths, the only way to ensure that the MTE is not impacted by non-linear effects is to use photocathodes that have QEs larger than 10^{-4} at the photoemission threshold like those found in alkali-antimonide photocathodes.

4.3.5 Selecting a Photocathode

When it comes to selecting a photocathode for an accelerator application, all of the above factors must be considered. In general the ideal photocathode would have the smallest possible MTE, the highest possible QE to mitigate the non-linear photoemission effects, and a fast response time. It turns out that these are all competing photocathode characteristics and are all coupled to the excess energy. From Sec. 4.3.1 we know that in order to minimize the MTE we must emit as close to threshold as possible. However the QE is proportional to the square of the excess energy and so it drops significantly near threshold (Dowell and Schmerge (2009)). In addition as we approach zero excess energy the response time increases to tens of picoseconds which which makes it unsuitable for applications that require ultrashort electron bunches (Musumeci *et al.* (2018)). In general we want photocathodes that have low MTE, QEs that are larger than 10^{-2} in the visible range, and a prompt sub-ps response time. However there currently are no photocathodes that simultaneously satisfy this

criteria, hence trade-offs must be made.

In addition there are a few more properties that must be considered when selecting photocathode materials like the work function, the robustness of the photocathode, and the lifetime of the photocathode. The work function of the photocathode is an important property due to limitations of modern laser technology. Typically modern ultrafast lasers generate in the IR or NIR range, and UV light is produced using harmonic generation crystals. However this method of UV generation is not very efficient and the power that is delivered by ultrafast UV laser pulses is significantly less than the power delivered by visible and IR laser pulses. The power of the drive laser limits the total charge that can be extracted from a photocathode. Therefore for applications that require high repetition rates (MHz - GHz), photocathodes should have a work function in the visible range in order to efficiently extract large currents. (Dowell *et al.* (2010)). In addition the transverse beam profile quality deteriorates during UV generation which makes UV pulse shaping inefficient due to the non-uniformity of the beam (DOE (2016); Musumeci *et al.* (2018)). Hence great efforts have gone into identifying photocathodes with small band gaps and low electron affinity in order to efficiently photoemit in the visible and IR range (Dowell *et al.* (2010); Musumeci *et al.* (2018)).

Since photoemission is a surface sensitive process the QE and the MTE depend heavily on the condition of the surface. In a high field and high laser fluence photoinjector environment the surface of the photocathode is susceptible to degradation from various mechanisms like chemical poisoning from residual gas (Chanlek *et al.* (2014)), laser heating (Anisimov *et al.* (1974)), and ion back-bombardment (Aulenbacher (2011)). Hence photocathodes need to be robust to photoinjector environments to ensure that they have a long lifetime.

4.4 Commonly Used Photocathode Materials

In this section we give a brief review of the photocathode materials that are commonly used and that are being investigated. Photocathode materials can generally be characterized into two types: High Electron Affinity and Low Electron Affinity. Electron affinity is defined as the difference between the conduction band minima and the vacuum level. High electron affinity materials are those in which the electron affinity is larger than the band gap, whereas low electron affinity materials are those in which the electron affinity is smaller than the band gap. Metals have zero band-gap and hence fall under the high electron affinity category. This classification is important for photocathodes as the photoemission process in these two kinds of materials is significantly different.

In High Electron Affinity materials the excited electrons are allowed to interact with the unexcited electrons and this scattering process is the most dominant. It also causes the excited electrons to lose energy very rapidly and hence very few of the excited electrons are emitted, making their QE at threshold in the 10^{-9} to 10^{-6} range.

Low electron affinity materials have a work function close to the band gap. Electrons excited to near-band-gap energies do not experience a large electron-electron scattering as there is no energy state for the electrons to go into post-scattering. Thus the excited electrons interact only with phonons, plasmons, and lattice defects all of which cause them to lose energy slowly in comparison to the electron-electron scattering process. As the work function is close to the band-gap, a large fraction of these excited electrons reaching the surface have sufficient energy to get emitted. Thus the QE for such low-electron-affinity materials is usually significantly higher in the range of 10^{-5} to 10^{-2} near threshold. Most semiconductor cathodes that are used

as electron sources (alkali-antimonides, Cs_2Te, NEA-GaAs) fall under this category.

Below we briefly describe the various metallic and semiconductor cathodes that have been used in photoinjectors along with their advantages, disadvantages, and drawbacks.

4.4.1 Metallic Photocathodes

Metallic photocathodes are popular choices for many electron sources like RF photoinjectors (Jongewaard *et al.* (2012)), wakefield accelerators Khachatryan *et al.* (2004), and stroboscopic UED/UEM (Grinolds *et al.* (2006); Barwick *et al.* (2008); Silva *et al.* (2018); Ji *et al.* (2019)). The main reason they are popular in RF guns is due to convenience. While semiconductors have significantly larger QEs than metals, their surface degrades in atmospheric conditions. Hence they require the ability to transfer the photocathode in UHV to the RF gun, and the gun itself requires a UHV loadlock. Metals are much more stable and due to their convenience of use, often times the back plate of the RF gun acts like a photocathode. In addition their surface is very robust against degradation from vacuum conditions, heating effects, and high electric fields. Therefore metals can provide long term stable performance in RF photoinjectors where very high fields are needed to extract large currents from the photocathode (Jongewaard *et al.* (2012)). Metallic photocathodes also have a very fast (sub-50 fs) response time in comparison to semiconductors. Hence they are well suited to applications that require ultrashort electron bunches like laser wakefield accelerators (Khachatryan *et al.* (2004)).

Atomically clean and ordered surfaces of single crystal metal also show promise. They can achieve very low MTEs with the record low MTE of 5 meV coming from a Cu(100) single crystal. However due to frequent electron-electron scattering during photoemission, these photocathodes suffer from a very low QE. Hence their low MTE

and low QE makes them suitable for low charge density applications like stroboscopic UEM/UEM (Grinolds *et al.* (2006); Barwick *et al.* (2008); Silva *et al.* (2018); Ji *et al.* (2019)). Single crystal metal surface states of Ag(111) have also been used for demonstrating low MTE along with high (10^{-4}) QE near threshold. Thus using the band-structure of single crystalline metals can potentially lead to obtaining low MTE and high QE simultaneously. Such surfaces have to be atomically clean and ordered, and hence they require UHV and are not stable for extended periods of time. Recent studies show that Gr coatings on such surfaces can help extend their lifetime (Liu *et al.* (2017)).

4.4.2 Semiconductor Photocathodes

Semiconductor photocathodes that are used include the family of alkali-antimonides, Cs2Te, and NEA-GaAs. All of them are low electrons affinity cathodes and hence demonstrate a significantly larger quantum efficiency compared to metal cathodes. Due to their high QE, they are already used for high average current applications. They are also being investigated as candidates for achieving extremely low MTEs at large charge densities due to their relatively high QE near threshold. The high QE near threshold helps mitigate MTE increasing effects of non-linear photoemission making these cathodes attractive for low MTE applications.

Negative Electron Affinity Gallium Arsenide

P-doped GaAs when coated with one monolayer of Cs/O results in a work function smaller than the bulk band gap resulting in negative electron affinity. In such a situation, a very large fraction of the electrons excited into the conduction band get emitted resulting in QE as high as 10^{-2} even at threshold. Furthermore, circularly polarized light preferentially excites electrons with one spin resulting in spin polarized

electron emission. Currently GaAs has the unique position of being the only photocathode capable of producing spin polarized electron beams. Spin polarized beams are essential for investigating nuclear phenomena at facilities like the future Electron-Ion Collider (EIC) (Aulenbacher (2011); Accardi *et al.* (2016)). While GaAs itself has a low QE, by activating GaAs to NEA electrons can be emitted exclusively from the top of the valence band which is necessary to generate spin-polarized beams (Bae *et al.* (2020)). Typically NEA has been achieved by activating p-doped GaAs with Cs which has resulted in strongly polarized beams with QEs as high as 10^{-1} (Dowell *et al.* (2010)). However the activated Cs surface is highly susceptible to various degradation mechanisms like ion-back bombardment and thermal desorption which can limit the operating lifetime of the photocathode to hours (Bae *et al.* (2018b)). Hence it is essential that these photocathodes are operated in the Xtreme high Vacuum (10^{-11} Torr), which limits them to DC applications (Musumeci *et al.* (2018); Bae *et al.* (2018b)). Recently there have been efforts to achieve NEA with a more robust activation layer than Cs. One such method used Cs_2Te as the activation layer which improved the lifetime by a factor of 5 when operating with green light (Bae *et al.* (2018b)). Another method used co-deposited Cs-Sb-0_2 which increased the lifetime by a factor of 6.8 at threshold and a factor of 10 at green light (Bae *et al.* (2020)). The thermal limit of 25 meV can be achieved from GaAs near the photoemission threshold (IR light), however at these IR photon energies GaAs has a very long response time of 100 ps which makes them unsuitable for photoinjectors. However by operating GaAs at higher photon energies in the visible range the response time reduces to a more useful 1-2 ps, although this comes at the cost of an increase in MTE to 120 meV (Bazarov *et al.* (2008)).

Alkali-Antimonides

Alkali-antimonide thin films are a family of PEA semiconductor photocathodes that are commonly used in photoinjectors. Several materials in the alkali-antimonide family exhibit low, but positive electron affinity which gives them high QEs that are comparable to NEA semiconductors. At threshold ($\sim$ 1.9 eV) alkali-antimonides like Cs_3Sb, K_2CsSb, and Na_2KSb have QEs as high as 10^{-1} at room temperature and 10^{-4} even when cryo-cooled down to 90 K (Dowell *et al.* (2010); Cultrera *et al.* (2015)). At these high QEs, large currents can be extracted without the use of high laser fluences that lead to the MTE-degrading non-linear photoemission effects. Hence these photocathodes can be operated right near the photoemission threshold allowing the MTE to be limited by the thermal limit rather than the excess energy. In addition the small band gap ($\sim$ 1 eV) and low electron affinity ($\sim$ 1 eV) of alkali-antimonides allows these photocathodes to be operated at visible photon energies thereby avoiding inefficient UV laser pulses (Dowell *et al.* (2010); Musumeci *et al.* (2018)). As a result alkali-antimonides have been utilized in photoinjectors for high brightness and high charge density applications (Vecchione *et al.* (2011); Dunham *et al.* (2013); Schmeißer *et al.* (2018)). However as of yet there are no detailed response time measurements from alkali-antimonide thin films. Although due to their small thickness the response time is expected to be in the sub-ps to 1 ps range near the photoemission threshold (Cultrera *et al.* (2015)).

One major challenge with alkali-antimonide photocathodes is their relatively short operational lifetimes due to sensitivity to vacuum conditions. Recently there have been several groups that have investigated the use of graphene protective layers on alkali-antimonide thin films in order to protect the photocathode surface from contamination, thus prolonging its lifetime (Yamaguchi *et al.* (2017, 2018); Liu *et al.*

(2022)).

Another major challenge with alkali-antimonides is that they are typically grown as polycrystalline thin films with very rough surfaces that limit the minimum attainable MTE. This has lead to a lot of effort in growing smooth alkali-antimonide thin films in order to minimize the contributions to MTE from these rough surfaces (Feng *et al.* (2017); Xie *et al.* (2017); Saha *et al.* (2022)). Recently by growing Cs_3Sb on a lattice matched 3C-SiC(001) substrate, the first ever alkali antimonide epitaxial growth was demonstrated with a $Cs_3Sb(001)$ single crystal (Parzyck *et al.* (2022)). This $Cs_3Sb(001)$ single crystal photocathode represents a major step forward towards the use of single crystal photocathodes in high charge density photoinjectors. However further MTE and response time measurements as well as high field testing is necessary before such photocathodes will realistically be utilized in photoinjectors.

Cesium Telluride

Cs_2Te is another popular PEA semiconductor photocathode which tends to offer a compromise between metallic and semiconductor photocathodes. It has very robust surfaces and long operating lifetimes like metals, and it has the high QEs of semiconductors (Kong *et al.* (1995a,b)). Cs_2Te provides several advantages over alkali-antimonide photocathodes like longer operating lifetimes and a robust surface while still maintaining a high QE, however it comes with the drawback of operating in the UV range which leads to both inefficient laser pulse generation and laser pulse shaping. In particular Cs_2Te can reach QEs as high as 10^{-1} when illuminated with UV light, and it can maintain these high QEs for up to a month under realistic photoinjector operating conditions. This is due to its robustness to damage from surface contamination, the driving laser, and high fields. Hence Cs_2Te is well suited to operating in RF photoinjectors where very high fields are used to extract large charge

densities (Kong *et al.* (1995b); Fry *et al.* (1998); Sertore *et al.* (2000)).

4.4.3 Nanotechnology and Photocathodes

Several recent advancements in nanotechnology have lead to the consideration of photonic-integrated and plasmonic-enhanced photocathodes for use in generating bright electron beams. It has been proposed that utilizing photonic structures like waveguides can enhance electron emission from photocathodes by breaking the trade-off that exists between the excitation photon energy, the MTE, the QE, and response time. One such method utilized a waveguide nano-fabricated underneath an ultra-thin high QE semiconductor photocathode (Blankemeier *et al.* (2019)). By irradiating the photocathode through the waveguide, the photons are absorbed at a very shallow depth which can break the trade-off that exists between the MTE and response time of the photocathode. Monte-Carlo simulations were performed on this configuration which showed that in addition to breaking the trade-off between MTE and response time, it also decouples the QE so that low MTEs, prompt response times, and high QEs can be achieved simultaneously (Blankemeier *et al.* (2019)). While these photonic-integrated structures offer a great deal of promise to photoinjectors, engineering such photocathodes has proven to be technologically challenging. One recent experimental investigation was able to engineer a photonic-integrated structure onto a photocathode and demonstrated photoemission confined by a waveguide on a 40 nm thick Cs activated GaAs photocathode (Kachwala *et al.* (2022a)). However this investigation was a proof-of-principle experiment and further studies are needed to demonstrate simultaneously achieving low MTE, low response times, and high QE from photonic-integrated photocathodes.

One example of plasmonic enhanced photocathodes makes use of nano-sized plasmonic structures which can greatly increase the quantum efficiency for specific wave-

lengths (Perchec *et al.* (2008)). By creating nanosized rectangular grooves arranged in a sub-wavelength array on the photocathode, the grooves act as surface plasmon resonance cavities which trap the incident laser light and dramatically increase the electron yield for a resonant wavelength. The resonant wavelength can be selected by designing the nano-structure array with different groove depths, widths, and periods. This method was demonstrated using a nano-structure array that was designed for a resonant wavelength of 720 nm. By irradiating it with a 800 nm center wavelength laser they observed an electron yield that was 6 orders of magnitude larger (Polyakov *et al.* (2013)).

4.4.4 Novel Materials

Since the discovery of Dirac materials there has been a lot of interest in implementing them into photocathode technology due to their multitude of unique and useful properties. For example graphene is already being utilized as a protective gas barrier for vacuum sensitive photocathodes (Yamaguchi *et al.* (2017, 2018); Liu *et al.* (2017, 2022); Knill *et al.* (2023b)). But there has also been interest in using Dirac materials like topological insulators and Dirac semi-metals as photocathodes themselves. These materials have a Dirac cone at the center of the Brillioun Zone which makes the effective mass of photo-emitted electrons around the Dirac point nearly zero. Therefore they offer the promise of low MTE (sub-10 meVs) even when operating with excess energies as large as 0.25 eV (Pan *et al.* (2011); Liu *et al.* (2014a,b); Xu *et al.* (2017); Tian *et al.* (2018)). In addition angle-resolved photoemission spectroscopy (ARPES) studies of the topological insulator Bi_2Se_3 have shown that it can even produce spin-polarized electrons which points to a path where a photocathode other than GaAs can generate spin-polarized beams (Pan *et al.* (2011)). However these photocathode materials still require detailed characterization and testing before they

can be considered realistic photocathode candidates.

4.5 Photocathode and Bright Beams Lab

In the last section we have seen that there are a wide variety of photocathode materials and technologies that can potentially improve the brightness of electron beams. In order to translate this research into improving electron beams it is critical that such photocathodes are tested in photoinjectors to see how they withstand the high field and high fluence environment. However most photoinjector are developed with the intention of operating continuously, and therefore they do not have the ability to test a wide variety of photocathodes. Instead they rely on the photocathodes that have already been well studied and choose the one that best suits their application. This process does not lead to a lot of novel photocathode testing, and hence there needs to be photoinjectors that are specifically designated to photocathode testing in order to really drive the photocathode field forward. In order to address this need we have recently commissioned the Photocathode and Bright Beams Lab (PBBL) at Arizona State University (ASU) as shown in Fig. 4.3. The PBBL has been designed to be the most comprehensive photocathode research facility to-date with a photocathode materials science focus.

The PBBL contains two growth chambers that are designated to growing alkali-antimonide photocathodes as well as other novel photocathode materials. Since photoemission is a surface sensitive process we have a variety of surface diagnostic capabilities that can map the physical features as well as the work function variations on the surface. We have photoemission experiments which allow us to measure the 3-D energy and momentum distributions of photoemitted electrons. In addition these experiments allow us to study the fundamentals of the photoemission process itself which is essential to identifying new photocathode materials and technologies. For

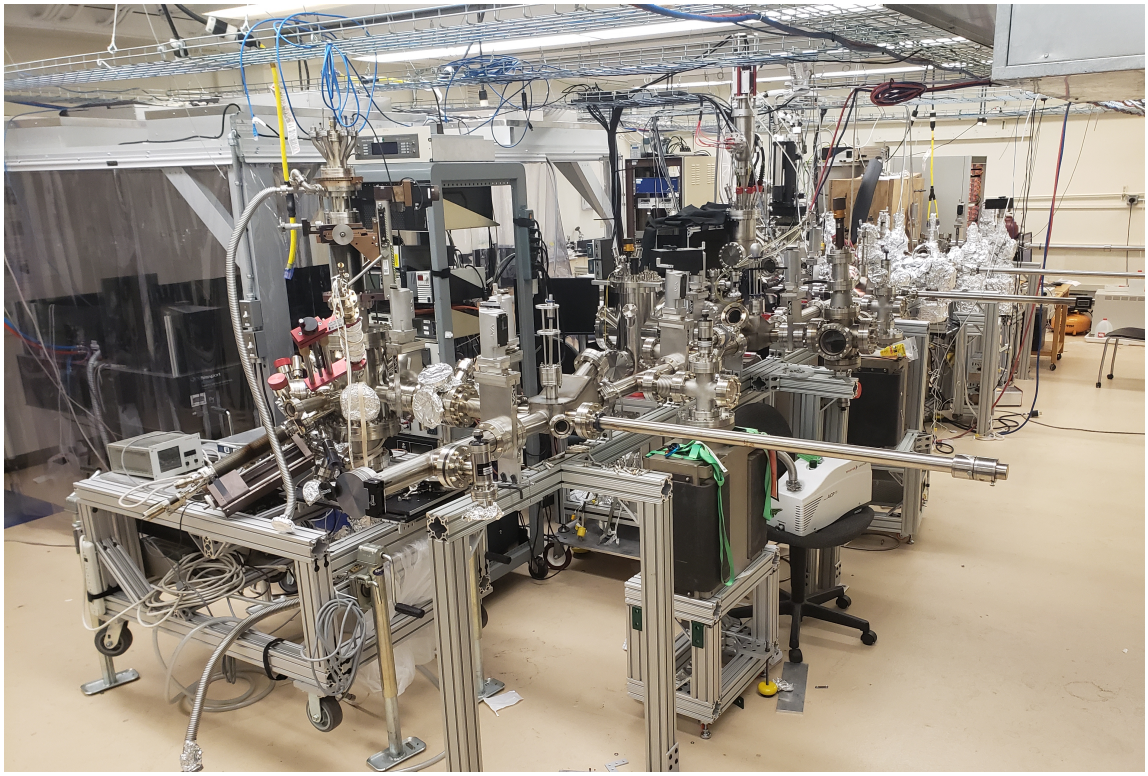

Figure 4.3: Picture of the Recently Commissioned Photocathode and Bright Beams Lab (PBBL). The PBBL Has Been Designed to Be a Comprehensive Photocathode Research Facility Equipped to Tackle Many Outstanding Challenges in Photocathode Characterization and Development.

testing photocathodes in a high field and high fluence environment we have the ASU DC electron gun. Figure 4.4 shows a 3-D model of the PBBL with all of these experimental capabilities connected by a single UHV transfer line. Every experimental chamber in the lab is compatible with omicron flag-style sample holders. This allows us to grow, characterize, and test photocathodes by rapidly transferring them between the various chambers without the need of vacuum suitcases. Transfers between vacuum suitcases can be time consuming and have the possibility of contamination, and so such a transfer line is essential for photocathodes with short lifetimes. In this chapter we discuss the experimental capabilities of the PBBL as well as some of the

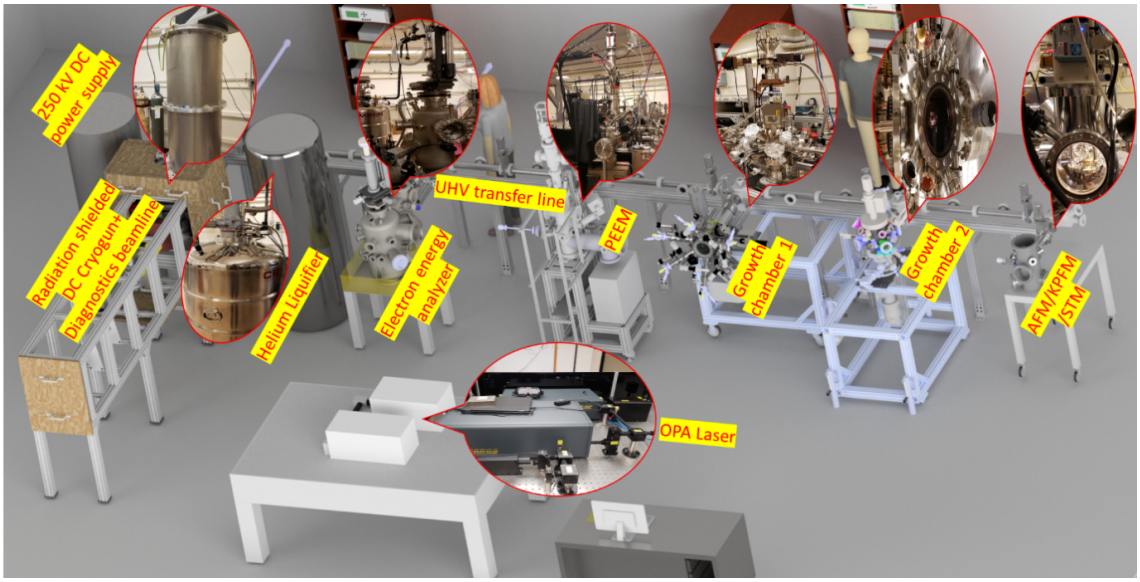

Figure 4.4: Schematic of the Photocathode and Bright Beams Lab (PBBL). While This Schematic Shows Two Growth Chambers Attached to the Transfer Line, We Plan to Only Have One Growth Chamber Attached at a Time. This Leaves Space for the Future Addition of Another Experimental Chamber Which Can Enhance the Lab.

work that has already been coming out of the lab.

4.5.1 Transfer Line

The transfer line consists of a stainless steel cart with stainless steel bearings that sits on an aluminium track as shown in Fig. 4.5. The cart has two steel pucks attached to the bottom on either end which allows an external handheld magnet to grab onto the cart and move it across the transfer line. The cart can hold up to 8 photocathodes mounted onto omicron flag-style sample holders which are compatible with every chamber in the lab. This allows for multiple photocathode materials to be tested simultaneously throughout the lab, and it also offers the possibility of long term photocathode storage.

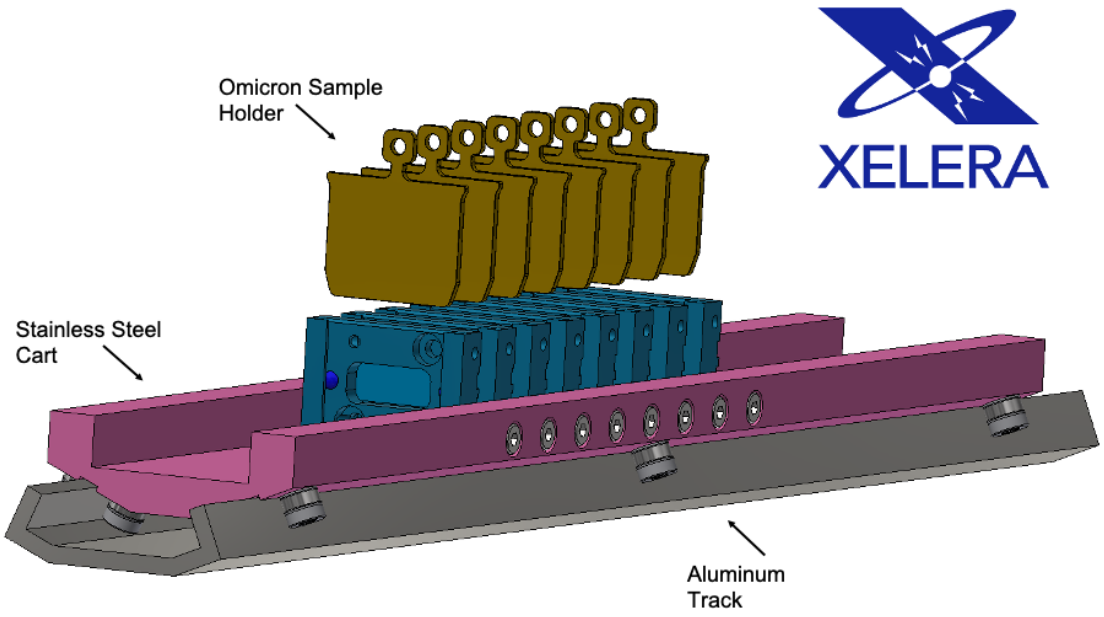

Figure 4.5: 3-D Model of the Stainless Steel Cart on a Section of the Aluminum Track. The Cart Can Hold 8 Photocathodes Mounted to Omicron Flag-style Sample Holders Which Are Compatible with Every Chamber in the Lab. This Allows for Testing of Multiple Photocathodes at Once as Well as Long Term Photocathode Storage.

The transfer line is $\sim$ 8 m long and it is made up of two different types of half-meter sections which are all connected by 4.5" CF flanges. The first intermediate section shown in Fig. 4.6 is located between the various experimental chambers and it consists of a track mounted to a 2.75" stainless steel tube. There is a 4.5" ConFlat (CF) port at the midway point which is used to connect various vacuum pumps and vacuum diagnostics to the transfer line. The second sample-transfer section shown in Fig. 4.7 is located at the junction between the transfer line and the experimental chambers. This section is where the sample is transferred between the cart and the various experimental chambers. It features a vertical wobblestick which is used to remove photocathodes from the cart and hand them to a linear transfer arm, with the

Figure 4.6: The Intermediate Section of the UHV Transfer Line. This Section Is Connected Between the Junctions of the Transfer Line to the Various Experimental Chambers. The Middle CF Port Is Used to Attach Various RGAs, Ion Gauges, Ion Pumps, and NEG Pumps.

transfer arm then placing the photocathodes in the experimental chambers. There are 3 viewports placed around this section which allow us to observe the sample transfer and ensure no samples are dropped. This method allows us to perform rapid photocathode transfers which is essential for testing materials with short lifetimes. For example, a photocathode can be grown in the growth chamber at one end of the transfer line, and moved to the other end of the transfer line and loaded into the DC electron gun in $\sim$ 15 minutes.

The transfer line was designed to operate at a base pressure of 10^{-10} Torr or lower. It is being pumped down by 5 large ion pumps with pumping speeds ranging from 75 l/s to 350 l/s as well as 4 non-evaporable getter (NEG) pumps with a pumping speed of 1000 l/s. Simulations performed using Molflow (Fig. 4.8) estimate that the pressure ranges between 4×10^{-11} Torr and 1.2×10^{-10} Torr. The only major spikes in pressure occur at the sample-transfer sections where there is a long linear transfer arm

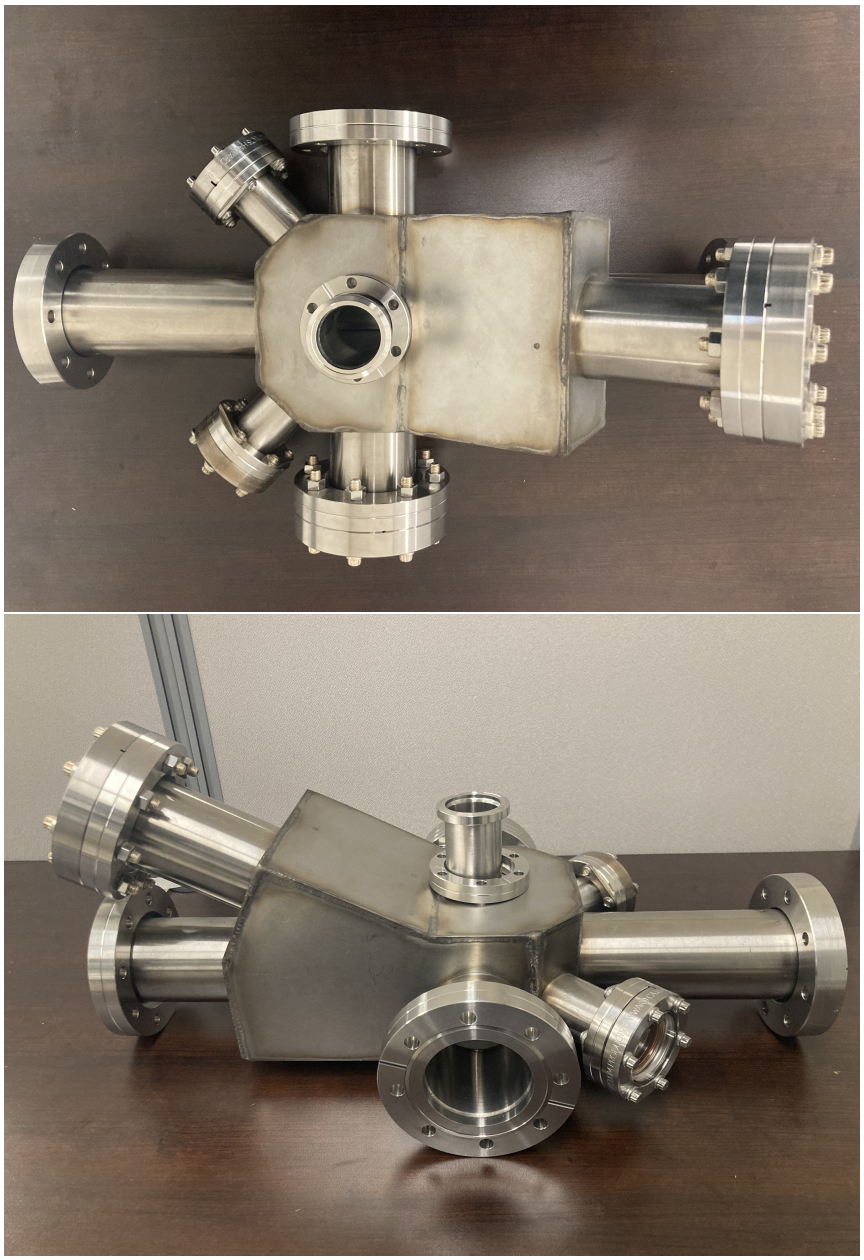

Figure 4.7: The Sample Transfer Section of the UHV Transfer Line. This Section Connects the Various Experimental Chambers to the Transfer Line.

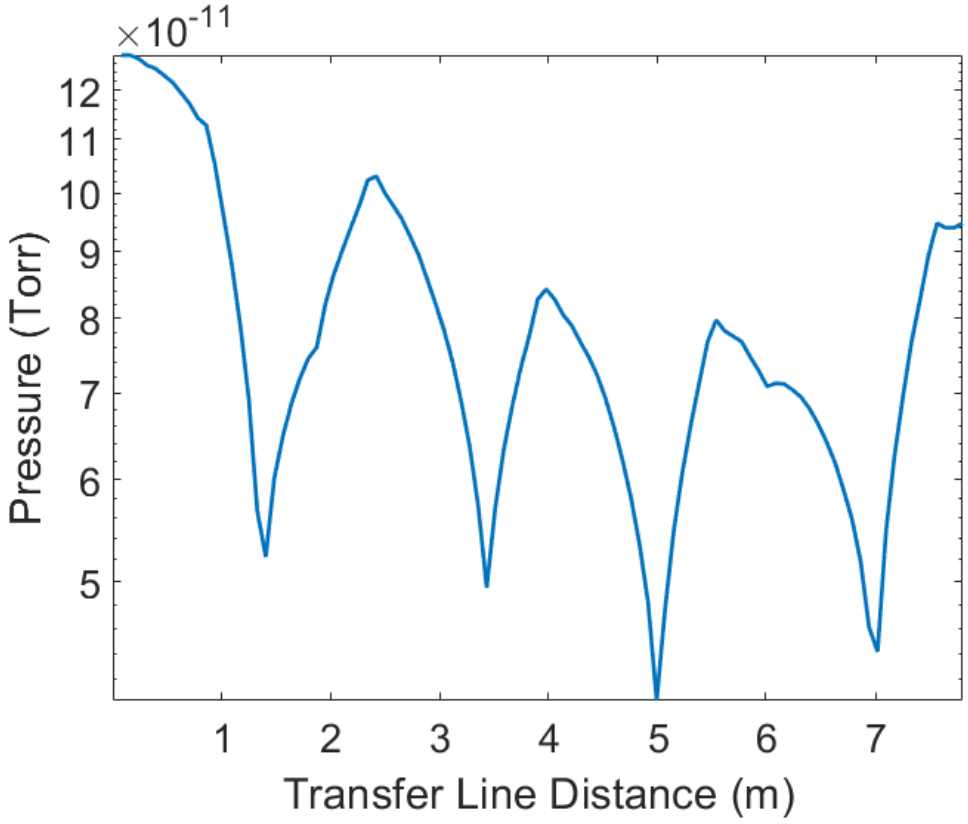

Figure 4.8: Simulations Were Performed Using Molflow Which Show the Pressure along the Transfer Line. The Pressure Remains Relatively Stable Between 4×10^{-11} Torr and 1.2×10^{-10} Torr. The Only Major Spikes in Pressure Occur at Locations Where There Is a Sample-transfer Section and a Long Transfer Arm Attached to the Transfer Line.

attached to the transfer line. In general this simulation suggested that the pressure will remain relatively stable around the low 10^{-10} Torr range. Ion pressure gauges and residual gas analyzers placed along the transfer line confirm that the pressure is indeed stable in the 10^{-10} Torr range.

4.5.2 Photocathode Growth

The lab will house two growth chambers which use thermal evaporators to grow thin films using molecular beam epitaxy. In order to avoid cross contamination one chamber will be dedicated to growing alkali-antimonide thin films while the other will be dedicated to growing novel photocathode materials. Although Fig. 4.4 shows both growth chambers attached to the transfer line, only one will be connected to the transfer line at any given time. This was done in order to allow enough space for the addition of another experimental chamber in the future. However both chambers are designed such that they can be quickly swapped out for each other.

The first growth chamber is dedicated to growing alkali-antimonide thin films and investigating new growth techniques. The sources are contained in effusion cells which are isolated from the rest of the growth chamber using manual gate valves and thin films are grown using molecular beam epitaxy. In addition this growth chamber has the capability of performing spectral response measurements across a broad range of wavelengths from 200 nm to 2 μm. Recently this growth chamber was used to grow a Cs_3Sb thin film on a lattice-matched STO substrate which resulted in physically and chemically smooth surfaces (Saha *et al.* (2022)). This photocathode represented a factor of 4 smoother surface in comparison to thin films of Cs_3Sb grown on Si substrates. The photocathode was transferred into the AFM/KPFM where the surface was measured and compared with Cs_3Sb on Si substrates as shown in Fig. 4.9.

The second growth chamber is currently being built and it will be dedicated to growing novel single crystal materials like the topological insulators and Dirac semimetals that were described in Sec. 4.4.4. This chamber will also have the capability of performing Energy-Dispersive X-ray Spectroscopy (EDX) and Reflection High Energy Electron Diffraction (RHEED) diagnostics. EDX will allow us to determine the

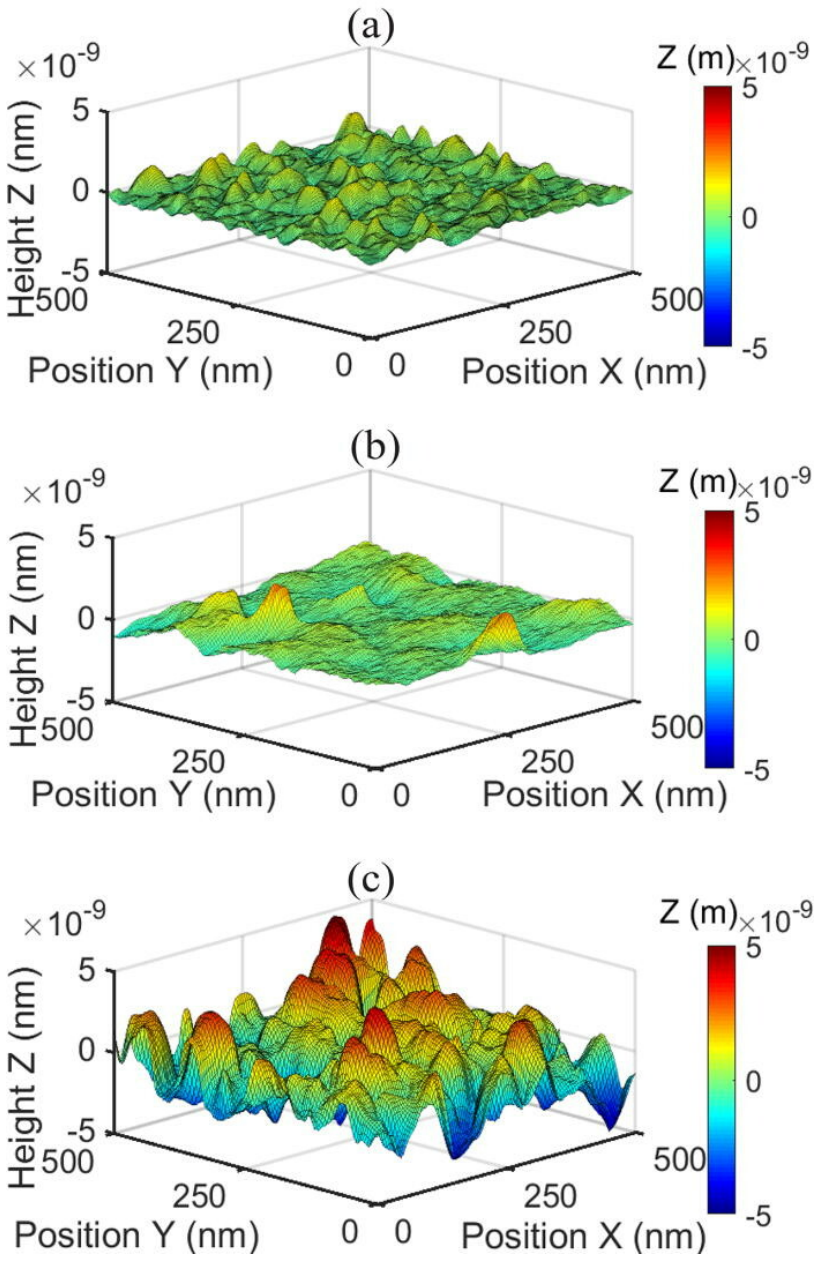

Figure 4.9: AFM Images Which Show the Physical Roughness of the Surface From Cs_3Sb Grown on a Lattice-matched STO Substrate.

precise chemical composition of the photocathode while RHEED will allow us to determine the crystal structure of the photocathode surface. In addition we have a surface preparation chamber attached to the transfer line which contains argon ion bombardment and high temperature annealing capabilities. Such surface preparation techniques are essential to achieving atomically ordered single-crystalline surfaces. Hence with appropriate single crystal growth, diagnostics, and surface preparation capabilities we will be able to obtain atomically ordered single crystal topological insulators and Dirac semi-metals with relative ease.

4.5.3 Surface Diagnostics

Since photoemission is a highly surface sensitive process, it is essential that reliable measurements are performed on the surface morphology of the photocathode. For that the PBBL has a variety of atomic scale surface diagnostics like Auger Electron Spectroscopy (AES), Low Energy Electron Diffraction (LEED), Atomic Force Microscopy (AFM), Kelvin Probe Force Microscopy (KPFM), Scanning Tunneling Microscopy (STM), and the EDX and RHEED capabilities described in the previous section. AES and EDX allow us to determine the chemical composition of the photocathode, LEED (Fig. 4.10) and RHEED allow us to determine the crystal structure of the photocathode surface, AFM and STM allow us to determine the physical roughness of the surface, and KPFM allows us to determine the work-function variations across the surface of the photocathode. Since photoemission characteristics like the work function and MTE are strongly dependant on the top-most layer of atoms of the photocathode, having the ability to perform such a detailed and complete characterization is essential to photocathode research and testing.

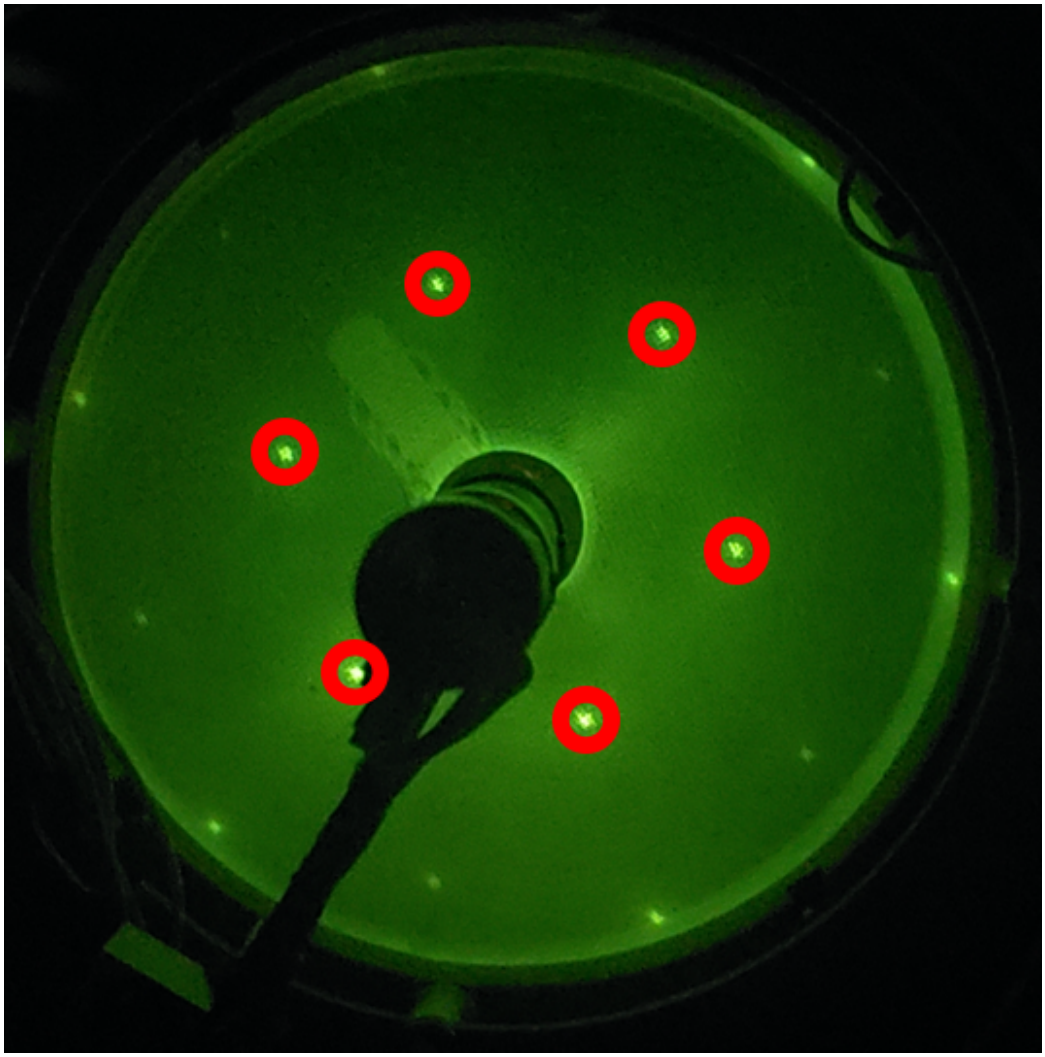

Figure 4.10: A LEED Pattern from a GaN Photocathode Showing a Sharp Hexagonal Pattern. The Red Circles Highlight the First Order Pattern Although Higher Order Spots Are Also Present.

4.5.4 Photoemission Diagnostics

Photoemission characterization is critical to understanding the emitted electron distribution for photocathodes as well as identifying promising photocathode materials. In the PBBL photoemission characterization experiments will be performed using a unique electron energy analyzer as well as a photoemission electron microscope (PEEM). These experiments will allow us to measure the MTE, energy spectra, longitudinal energies, and the QE from a wide variety of photocathode materials. In addition to directly investigating photocathodes, we will also perform investigations on the photoemission process itself by studying mechanisms like non-linear photoemission and limitations like the sudden approximation. This will allow us to gain a deeper understanding of the physics of photoemission which is essential to engineering novel materials that can improve the brightness of current and future photoinjectors.

The electron energy analyzer is a unique instrument that measures the 3-D energy and momentum distributions of meV electrons with sub-meV resolution (Karkare *et al.* (2019)). It features a time-of-flight based delayline detector arranged in a parallel plate configuration with the photocathode and separated by $\sim$ 4 cm. The photo-electrons are accelerated towards the detector by a voltage ranging from 4 V - 72 V depending on the application. The detector records the x- and y- positions of the photo-emitted electrons and from that the transverse and longitudinal energies and momenta can be calculated in a straightforward manner. The sample is connected to a liquid helium (LHe) cryostat and can be cooled to 30 K indefinitely using the helium re-circulation line detailed later in this chapter. This unique design makes the electron energy analyzer the most precise near-threshold photoemission diagnostics experiment in the world. And in fact it holds the record for the lowest MTE ever measured which was 5 meV from Cu(100) operated near threshold and cryo-cooled

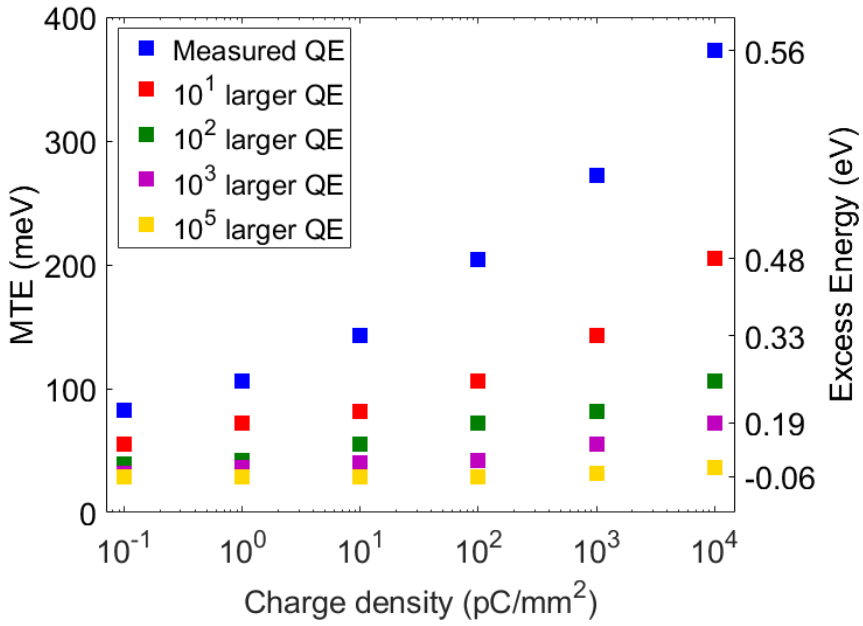

Figure 4.11: Results from an Investigation into the Effects of Non-linear Photoemission on Metallic Photocathodes Using the Electron Energy Analyzer.

to 30 K (Karkare *et al.* (2017)). Recently it has been used to study linear and non-linear photoemission from graphene-coated Cu(110) with some of the results shown in Fig. 4.1 (Knill *et al.* (2022, 2023b) and Fig. 4.11 (Knill *et al.* (2023a)). However one major limitation of the energy analyzer is that it is best suited to precise near-threshold measurements and therefore it must be operated in low field and under low laser fluence conditions. Therefore photocathodes which show promise in the energy analyzer under low fields and lower laser fluences will then be tested further in the ASU DC electron gun under high fields and high laser fluences.

The PBBL also houses a commercially available photoemission electron microscope (PEEM) which has 40 nm spatial resolution, sub-8 mÅ^{-1} k-space resolution, and 62 meV energy resolution (FOCUS (2023)). It can be used to measure the MTE, energy spectra, QE, spatial variations, and work function variations of the photo-

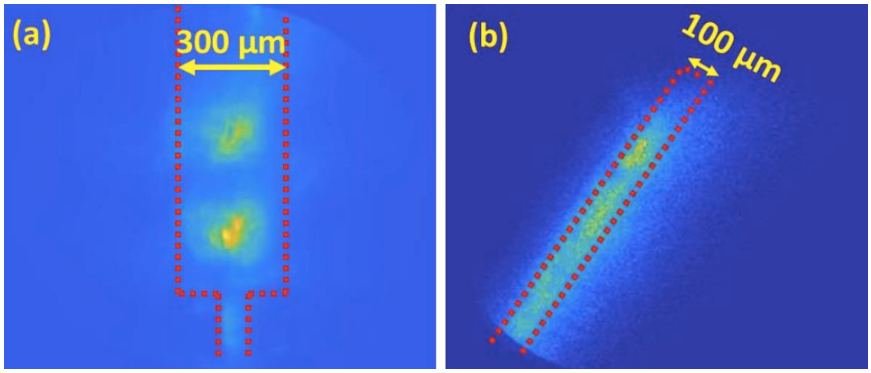

Figure 4.12: Image from the Peem Showing Confined Non-linear Emission From: (a) Graphene Using a Tapered Waveguide, and (b) Carbon Contaminants Using a Straight Waveguide.

cathode. In addition it can be used to investigate novel photocathode technologies like nano-scale electron sources, photonic-integrated photocathodes, and plasmonic-enhanced photocathodes. Recently it has been used to demonstrate proof-of-principle measurements of nitrogen-incorporated ultra-nano-crystalline diamond ((N)UNCD) (Kachwala *et al.* (2022b)) and photonic-integrated photocathodes using waveguides (Kachwala *et al.* (2022a)).

4.5.5 High Field Testing

In order to translate photocathode research into improving the performance of bright electron sources, it is critical that photocathodes are tested in high field and high laser fluence conditions in photoinjectors. To perform high field and high fluence photocathode testing in the PBBL, we have built the ASU 200-kV DC electron gun (Gevorkyan *et al.* (2019)). It was modeled after the Cornell electron gun with a few modifications (Lee *et al.* (2018); Li *et al.* (2022)). First instead of using a closed-cycle refrigeration system like the Cornell gun, the ASU gun is cooled by an LHe

cryostat which allows it to reach temperatures of 30 K with minimal vibrations during cryo-cooling. Second the ASU gun is designed to use photocathodes mounted to omicron flag-style sample holders which are compatible with all of the experimental capabilities detailed in this chapter. This allows us to not only test a wide variety of photocathode materials with different shapes and sizes, but it also allows us to characterize the photocathodes using the various UHV diagnostic tools in the PBBL. And lastly it has multiple laser input ports which allow us to test the performance of the photocathode at various angles of incidence.

Attached to the ASU gun is a diagnostic beamline which consists of two solenoids, a 3 GHz RF bunching cavity, and a 3 GHz RF deflection cavity. The RF cavities are synchronized to the laser system with a sub-30 fs jitter. This allows for accurate response time measurements across a wide range of wavelengths (200 nm - 2 μm). The emittance of the electron beam can be measured using a solenoid scan technique with a knife edge to measure the spot size, and from that the MTE can be deduced. The ASU gun and the beamline can measure the MTE, QE, and response time of the photocathode at high fields and high laser fluences. Currently it is being used to perform such measurements on physically and chemically smooth alkali-antimonides. And although the ASU gun and diagnostic beamline has been designed to investigate photocathode materials, it also has the capability of operating as a UED beamline.

4.5.6 Additional Features

In addition to the experimental capabilities discussed in this chapter, there are a few other components which make the PBBL unique like single crystal surface preparation techniques, a closed loop LHe plant, and a tunable wavelength laser system.

Since atomically ordered single-crystalline photocathodes offer the best path to low

MTEs by eliminating the MTE-degrading surface nonuniformities, it is essential that we have the tools to achieve these surfaces. In order to achieve an atomically ordered single-crystalline surface, the photocathode typically needs to undergo repeated cycles of Argon ion bombardment and high temperature annealing. While these surface preparation techniques are well known, no photoinjector in the world has the ability to perform them in-situ and therefore single crystalline photocathodes have not been yet utilized in photoinjectors. Adding the capability to perform such surface preparation would require significant financial investment as well as down time from operation. As previously mentioned, most photoinjectors are designed to operate continuously and therefore adding these surface preparation techniques is not practical unless single crystalline photocathodes are guaranteed to offer improved performance under high fields and high laser fluences.

In order to cryo-cool the electron energy analyzer and the DC electron gun we have a Cryomech LHe plant with a 150 L Dewar in our lab. The LHe plant uses a pulse-tube compression system in order to cool the cold-head down to 4 K, and it is capable of liquefying ultra-high purity He gas into LHe at a rate of 24 L/day. The Dewar feeds two extraction lines which are each connected to the electron energy analyzer and DC electron gun. The disconnect between the cryo-cooling mechanism and experimental chambers themselves is essential for operating our experiments in a vibration free environment. When cooling these two chambers, the LHe boil off is collected and fed into a He re-circulation line which pumps the He gas back into the Dewar for liquefaction. A flow rate monitor tracks the He gas flow rate and ensures that our LHe extraction does not exceed the maximum liquefaction rate of the LHe plant. This allows us to cryogenically cool the electron energy analyzer and the DC electron gun for indefinite periods of time without any loss of He.

Perhaps the most important piece of equipment in any photoemission lab is the

driving laser. The PBBL uses a tunable wavelength LightConversion ORPHEUS optical parametric amplifier (OPA) pumped by LightConversion PHAROS solid-state laser. The PHAROS is a 20 W laser with a 1030 nm center wavelength, 130 fs pulse duration, and 500 kHz repetition rate. At the output of the laser 10 W is directed towards the OPA using a beam splitter while the other 10 W is sent to a beam dump. The OPA uses a series of lenses, crystals, and mirrors in order to generate wavelengths between 200 nm and 2 μm. At the output of the OPA the beam can be directed towards the PEEM, the energy analyzer, the DC electron gun, or the growth chamber. This allows us to perform very detailed MTE, QE, emittance, energy distribution, and response time measurements in a wide range of vacuum environments. In addition since many different photoinjectors use pulse lengths ranging from sub-ps to 10 ps, we have built a pulse stretcher that utilizes a pair of diffraction gratings to stretch the laser from its natural pulse length of 130 fs to laser pulse lengths between 1 ps and 10 ps.

4.6 Summary

In this chapter we reviewed various photocathode materials and technologies, the factors that impact the brightness of an electron beam, and outlined the experimental capabilities and work being performed in the Photocathode and Bright Beams Lab at Arizona State University. While the review presented in Sec. 4.3 and Sec. 4.4 is far from comprehensive and there are notable omissions like disorder induced heating and nano-blade photocathode technology, it does provide a strong foundation for the presentation of the PBBL in Sec. 4.5.

In Sec. 4.5 we outlined the PBBL and its broad range of experimental capabilities. It has the capabilities of growing alkali-antimonide and novel Dirac metal photocathodes. It has numerous surface diagnostic techniques which are essential for surface

characterization and preparation. It has unique photoemission diagnostics with the most precise near-threshold photoemission diagnostics in the world. And It has a photoinjector which is capable of testing various photocathode materials over a wide range of photon energies and at temperatures as low as 30 K. Lastly it has all of these capabilities connected by a single UHV environment which allows for samples to be rapidly transferred between experimental chambers. This puts the PBBL in the position as the most comprehensive photocathode research facility in the world.

Chapter 5

CONCLUSION

In order to improve the performance of linear accelerator applications like XFELs, UED, and UEM it is essential that we generate electron beams from low-MTE photocathodes. The lowest MTE ever measured was from a Cu(100) single crystalline surface that was cooled to 30 K and operated near the photoemission threshold (Karkare *et al.* (2020)). However this photocathode has two major drawbacks: 1. Poor surface stability and 2. Low QE which leads to MTE-degrading non-linear effects when extracting large charge densities. Coating the photocathode surface with graphene protective barriers has been investigated as a method of improving surface stability (Liu *et al.* (2017); Yamaguchi *et al.* (2017, 2018); Liu *et al.* (2022)). However it is not known if a graphene layer affects the MTE. Non-linear photoemission effects have been the subject of several theoretical and experimental investigations which suggest that these effects can increase the MTE significantly (Pasmans *et al.* (2016); Maxson *et al.* (2017); Bae *et al.* (2018); An *et al.* (2018)). However there has not yet been an experimental investigation which provided measurements of non-linear photoemission effects in their entirety.

In this dissertation we first experimentally investigated the two main issues surrounding low-MTE metallic photocathodes: stability and non-linear photoemission. In Ch. 2 we investigated the impact that a graphene protective coating has on the MTE from a Cu(110) single crystalline photocathode. We performed MTE measurements near the photoemission threshold at room and cryogenic temperatures. We demonstrated MTEs at the thermal limit (25 meV) for room temperature and sub-10 meV for cryogenic temperatures. The thermal limit at room temperature was mea-

sured for 7 days indicating that a graphene protective coating results in an extremely stable photocathode surface. Furthermore LEED and AES indicated that a graphene protective coating significantly reduces the surface preparation required to achieve an atomically ordered single crystalline surface. Thus making graphene protective coatings viable options for protecting the surface of single crystalline photocathodes without impacting the photoemission properties.

In Ch. 3 we investigated the non-linear photoemission effects that arise when extracting large current densities from low QE metallic photocathodes. In particular we measured the contribution that non-linear photoemission effects have on the MTE of a graphene-coated Cu(110) single crystal over a wide range of laser fluences, excess energies, and laser pulse lengths. We demonstrated that non-linear effects can be significantly mitigated at 10 ps pulse lengths, which suggests that a significant change in the photoemission process occurs at 10-ps timescales. Using our measured data we devised an extrapolation scheme which allows us estimate the contribution to MTE from non-linear effects at realistic photoinjector fluence and charge density conditions. Our results show that for low QE metallic photocathodes there needs to be a balance between contributions from the excess energy and non-linear effects in order to achieve the minimum MTE at high charge densities. The only way to ensure that the MTE is not impacted by non-linear effects is to use photocathodes that have QEs larger than 10^{-4} at threshold like alkali antimonides.

Chapter 4 presents a brief review of photocathode physics and the brightness limiting factors that impact electron emission from photocathodes. In particular we review the MTE-limiting factors of excess energy, surface nonuniformities, band structure, and non-linear photoemission and discuss ways of mitigating them. We review various photocathode materials and technologies that have been used along with their advantages, disadvantages, and drawbacks. Novel photocathode materials and tech-

nologies were discussed with a focus on their advantages as well as challenges that are associated with utilizing them in photoinjectors. We then presented the experimental capabilities of the recently commissioned Photocathode and Bright Beams Lab (PBBL). The PBBL has been designed to be a comprehensive photocathode research facility equipped to tackle many outstanding challenges in photocathode characterization and development, and is required to develop photocathode technologies which will enable overcoming the practical limitations of metallic photocathodes.

Accardi, A., J. Albacete, M. Anselmino, N. Armesto, E. Aschenauer, A. Bacchetta, D. Boer, W. Brooks, T. Burton, N.-B. Chang, W.-T. Deng, A. Deshpande, M. Diehl, A. Dumitru, R. Dupré, R. Ent, S. F. d, H. Gao, V. Guzey, H. Hakobyan, Y. Hao, D. Hasch, R. Holt *et al.*, "Electron-ion collider: The next qcd frontier: Understanding the glue that binds us all", Eur. Phys. J. A **52**, 268 (2016).

Ago, H., K. Kawahara, Y. Ogawa, S. Tanoue, M. A. Bissett, M. Tsuji, H. Sakaguchi, R. J. Koch, F. Fromm, T. Seyller, K. Komatsu and K. Tsukagoshi, "Epitaxial growth and electronic properties of large hexagonal graphene domains on Cu(111) thin film", Appl. Phys. Exp **6**, 075101 (2013).

Akre, R., D. Dowell, P. Emma, J. Frisch, S. Gilevich, G. Hays, P. Hering, R. Iverson, C. Limborg-Deprey, H. Loos, A. Miahnahri, J. Schmerge, J. Turner, J. Welch, W. White and J. Wu, "Commissioning the linac coherent light source injector", Phys. Rev. ST Accel. Beams **11**, 030703 (2008).

Akturk, S., X. Gu, M. Kimmel and R. Trebino, "Extremely simple single-prism ultrashort-pulse compressor", Optics Express **14**, 21 (2006).

An, C., R. Zhu, J. Xu, Y. Liu, X. Hu, J. Zhang and D. Yu, "Increase of intrinsic emittance induced by multiphoton photoemission from copper cathodes illuminated by femtosecond laser pulses", AIP Adv. **8**, 055225 (2018).

Anisimov, S. I., B. L. Kapeliovich and T. L. Perel'Man, "Electron emission from metal surfaces exposed to ultrashort laser pulses", Zh. Eksp. Teor. Fiz. **66(2)**, 375 (1974).

APE, "pulseCheck", `https://www.ape-berlin.de/en/autocorrelator/pulsecheck/` (2023).

Armstrong, M. R., K. Boyden, N. D. Browning, G. H. Campbell, J. D. Colvin, W. J. DeHope, A. M. Frank, D. J. Gibson, F. Hartemann, J. S. Kim, W. E. King, T. B. LaGrange, B. J. Pyke, B. W. Reed, R. M. Shuttlesworth, B. C. Stuart and B. R. Torralva, "Four-dimensional ultrafast electron microscopy", Ultramicroscopy **107**, 356 (2007).

Aseyev, S. A., E. A. Ryabov, B. N. Mironov and A. A. Ischenko, "The development of ultrafast electron microscopy", Crystals **10(6)**, 452 (2020).

Aulenbacher, K., "Polarized beams for electron accelerators", Eur. Phys. J. Special Topics **198**, 361 (2011).

Bae, J. K., I. Bazarov, P. Musumeci, S. Karkare, H. A. Padmore and J. Maxson, "Brightness of femtosecond nonequilibrium photoemission in metallic photocathodes at wavelengths near the photoemission threshold", J. Appl. Phys. **124**, 244903 (2018a).

Bae, J. K., L. Cultrera, P. DiGiacomo and I. Bazarov, "Rugged spin-polarized electron sources based on negative electron affinity gaas photocathode with robust Cs_2Te coating", Appl. Phys. Lett. **112**, 154101 (2018b).

Bae, J. K., A. Galdi, L. Cultrera, F. Ikponmwen, J. Maxson and I. Bazarov, "Improved lifetime of a high spin polarization superlattice photocathode", J. Appl. Phys. **127**, 124901 (2020).

Bainbridge, A. R., C. W. B. Myers and W. A. Bryan, "Femtosecond few-to single-electron point-projection microscopy for nanoscale dynamic imaging", Struct. Dyn. **3**, 023612 (2016).

Barwick, B., H. S. Park, O.-H. Kwon, J. S. Baskin and A. H. Zewail, "4D imaging of transient structures and morphologies in ultrafast electron microscopy", Science **322**, 1227 (2008).

Bazarov, I., D. M. Dunham, Y. Li, X. Liu, D. G. Ouzounov, C. K. Sinclair, F. Hannon and T. Miyajima, "Thermal emittance and response time measurements of negative electron affinity photocathodes", J. Appl. Phys. **103**, 054901 (2008).

Bazarov, I. V., B. M. Dunham and C. K. Sinclair, "Maximum achievable brightness from photoinjectors", Phys. Rev. Lett. **102**, 104801 (2009).

Blankemeier, L., F. Rezaeifar, A. Garg and R. Kapadia, "Integrated photonics for low transverse emittance, ultrafast negative electron affinity gaas photoemitters", J. Appl. Phys. **126**, 033102 (2019).

Bunau, O. and Y. Joly, "Self-consistent aspects of x-ray absorption calculations", J. of Phys: Cond. Mat. **21**, 34 (2009).

Carbone, F., O. Kwon and A. H. Zewail, "Dynamics of chemical bonding mapped by energy-resolved 4d electron microscopy", Science **325**, 181 (2009).

Chanlek, N., J. D. Herbert, R. M. Jones, L. B. Jones, K. J. Middleman and B. L. Militsyn, "The degradation of quantum efficiency in negative electron affinity gaas photocathodes under gas exposure", J. Phys. D: Appl. Phys. **47**, 055110 (2014).

Chatelain, R. P., V. R. Morrison, C. Godbout and B. J. Siwick, "Ultrafast electron diffraction with radio-frequency compressed electron pulses", Appl. Phys. Lett. **101**, 081901 (2012).

Cultrera, L., S. Karkare, H. Lee, X. Liu, I. Bazarov and B. Dunham, "Cold electron beams from cryocooled, alkali antimonide photocathodes", Phys. Rev. ST Accel. Beams **18**, 113401 (2015).

da Silva, N. R., M. Moller, A. Feist, H. Ulrichs, C. Ropers and S. Schafer, "Nanoscale mapping of ultrafast magnetization dynamics with femtosecond lorentz microscopy", Phys. Rev. X **8**, 031052 (2018).

DOE, "Basic energy sciences workshop on the future of electron sources", (2016).

Dowell, D. H., I. Bazarov, B. Dunham, K. Harkay, C. Hernandez-Garcia, R. Legg, H. Padmore, T. Rao, J. Smedley and W. Wan, "Cathode R&D for future light sources", Nucl. Instrum. Meth. A **622**, 685 (2010).

Dowell, D. H., F. K. King, R. E. Kirby, J. F. Schmerge and J. M. Smedley, "In situ cleaning of metal cathodes using a hydrogen ion beam", Phys. Rev. ST Accel. Beams **9**, 063502 (2006).

Dowell, D. H. and J. Schmerge, "Quantum efficiency and thermal emittance of metal photocathodes", Phys. Rev. ST Accel. Beams **12**, 074201 (2009).

Dunham, B., J. Barley, A. Bartnik, I. V. Bazarov, L. Cultrera, J. Dobbns, G. Hoffstaetter, B. Johnson, R. Kaplan, S. Karkare, V. Kostroun, Y. Li, M. Liepe, X. Liu, F. Loehl, J. M. Maxson, P. Quigley, J. Reilly, D. Rice, D. Sabol, E. Smith, K. Smolenski, M. Tigner, V. Vesherevich, D. Widger and Z. Zhao, "Record high-average current from a high-brightness photoinjector", Appl. Phys. Lett. **102**, 034105 (2013).

Elsayad-Ali, H. L., T. B. Norris, M. A. Pessot and G. A. Mourou, "Time-resolved observation of electron-phonon relaxation in copper", Phys. Rev. Lett. **58**, 1212 (1987).

Emma, P., R. Akre, J. Arthur, R. Bionta, C. Bostedt, J. Bozek, A. Brachmann, P. Bucksbaum, R. Coffee, F.-J. Decker, Y. Ding, D. Dowell, S. Edstrom, A. Fisher, J. Frisch, S. Gilevich, J. Hastings, G. Hays, P. Hering, Z. Huang, R. Iverson, H. Loos, M. Messerschmidt, A. Miahnahri, S. Moeller, H.-D. Nuhn, G. Pile, D. Ratner, J. Rzepiela, D. Schultz, T. Smith, P. Stefan, H. Tompkins, J. Turner, J. Welch, W. White, J. Wu, G. Yoecky and J. Galayda, "First lasing and operation of an ångstrom-wavelength free electron laser", Nat. Photonics **4**, 641 (2010).

Feng, J., S. Karkare, J. Nasiatka, S. Schubert, J. Smedley and H. A. Padmore, "Near atomically smooth alkali antimonide photocathode thin films", J. Appl. Phys. **121**, 044904 (2017).

Feng, J., J. Nasiatka, W. Wan, S. Karkare, J. Smedley and H. A. Padmore, "Thermal limit to the intrinsic emittance from metal photocathodes", Appl. Phys. Lett. **107**, 134101 (2015).

Ferrario, M., "Overview of FEL injectors", Proceedings of EPAC, Edinburgh, Scotland (2015).

Ferrini, G., F. Banfi, C. Giannetti and F. Parmigiani, "Non-linear electron photoemission from metals with ultrashort pulses", Nucl. Instrum. Meth. A **601**, 123 – 131 (2009).

Filippetto, D., J. Grames, C. Hernandez-Garcia, S. Karkare, P. Piot, J. Power, Y. Sun and E. Wang, "Electron sources for accelerators", arXiv:2207.08875 [physics.acc-ph] (2022).

FOCUS, "PEEM", `https://www.focus-gmbh.com/%20peem-nanoesca/peem/` (2023).

Fry, A., E. Hahn, W. Hartung and M. Kuchnir, "Experience at fermilab with high quantum efficiency photo-cathodes for RF electron guns", Dept. of Energy. Office of Energy Research (1998).

Gevorkyan, G., S. Karkare, S. Emamian, I. V. Bazarov and H. A. Padmore, "Effects of physical and chemical surface roughness on the brightness of electron beams from photocathodes", Phys. Rev. ST Accel. Beams **21**, 093401 (2018).

Gevorkyan, G. S., S. S. Karkare, I. V. Bazarov, L. Cultrera, A. Galdi, W. H. Li and J. M. Maxson, "Design of a 200 kV DC cryocooled photoemission gun for photocathode investigations", Proceedings of NAPAC2019, **MOPLM16** (2019).

Grinolds, M. S., V. A. Lobastov, J. Weissenrieder and A. H. Zewail, "Four-dimensional ultrafast electron microscopy of phase transitions", Proc. Natl. Acad. Sci. **103**, 18427–18431 (2006).

Hohlfeld, J., S.-S. Wellershoff, J. Güdde, U. Conrad and E. M. V. Jähnke, "Electron and lattice dynamics following optical excitation of metals", Chemical Physics **251**, 237 (2000).

Ibsen, `https://ibsen.com/product/uv-2847-916/` (2022).

Ischenko, A. A., P. M. Weber and R. J. D. Miller, "Capturing chemistry in action with electrons: Realization of atomically resolved reaction dynamics", Chem. Rev. **117**, 11066 (2017).

Ji, F., D. Durham, A. Minor, P. Musumeci, J. Navaroo and D. Filippetto, "Ultrafast relativistic electron nanoprobes", Nat. Comm. Phys. **2**, 54 (2019).

Jongewaard, E., R. Akre, A. Brachmann, J. Corbett, S. Gilevich, K. Grouev, P. Hering, P. Krejcik, J. Lewandowski, H. Loos, T. Montagne, J. C. Sheppard, P. Stefan, A. Vlieks, S. Weathersby and F. Zhou, "Rf gun photocathode research at slac", Proceedings of IPAC2012, **MOPPP046** (2012).

Kachwala, A., O. Chubenko, S. Karkare, R. Ahsan, H. U. Chae and R. Kapadia, "On-chip photonics integrated cathodes", Proceedings of the 3rd North American Particle Acclerator Conference, **WEPA65** (2022a).

Kachwala, A., O. Chubenko, D. Kim, E. I. Simakov and S. Karkare, "Quantum efficiency, photoemission energy spectra, and mean transverse energy of ultrananocrystalline diamond photocathode", J. Appl. Phys. **132**, 224901 (2022b).

Karkare, S., G. Adhikari, W. A. Schroeder, J. K. Nangoi, T. Arias, J. M. Maxson and H. A. Padmore, "Ultracold electrons via near-threshold photoemission from single-crytal Cu(100)", Phys. Rev. Lett. **125**, 054801 (2020).

Karkare, S. and I. Bazarov, "Effects of surface nonuniformities on the mean transverse energy from photocathodes", Phys. Rev. Appl. **4**, 024015 (2015).

Karkare, S., J. Feng, X. Chen, W. Wan, F. J. Palomares, T.-C. Chiang and H. A. Padmore, "Reduction of intrinsic electron emittance from photocathodes using ordered crystalline surfaces", Phys. Rev. Lett. **118**, 164802 (2017).

Karkare, S., J. Feng, J. Maxson and H. A. Padmore, "Development of a 3-D energy-momentum analyzer for mev-scale energy electrons", Rev. Sci. Instrum. **90**, 053902 (2019).

Khachatryan, A. G., F. A. v. Goor, K.-J. Boller, A. J. W. Reitsma and D. A. Jaroszynski, "Extremely short relativistic-electron-bunch generation in the laser wakefield via novel bunch injection scheme", Phys. Rev. ST Accel. Beams **7**, 121301 (2004).

Knill, C. J., S. Douyon and S. Karkare, "Effects of non-linear photoemission on MTE from metal photocathodes", Manuscript under preparation (2023a).

Knill, C. J., H. A. Padmore and S. S. Karkare, "Near-threshold nonlinear photoemission from Cu(100)", Proceedings of the 12th International Particle Accelerator Conference, Sao Paulo, Brazil p. WEPAB099 (2021).

Knill, C. J., H. Yamaguchi, K. Kawahara, G. Wang, E. Batista, P. Yang, H. Ago, N. Moody and S. Karkare, "Near-threshold photoemission from graphene-coated Cu(110)", Phys. Rev. Appl. **19**, 014015 (2023b).

Knill, C. J., H. Yamaguchi, K. Kawahara, G. Wang, E. Batista, P. Yang, H. Ago, N. A. Moody and S. S. Karkare, "Near threshold photoemission from graphene coated cu single crystals", Proceedings of the 3rd North American Particle Acclerator Conference, **WEPA66** (2022).

Kong, S. H., J. Kinross-Wright, D. C. Nguyen and R. L. Sheffield, "Photocathodes for free electron lasers", Nucl. Instrum. Meth. A **358**, 272 (1995a).

Kong, S. H., J. Kinross-Wright, D. C. Nguyen, R. L. Sheffield and M. E. Weber, "Performance of cesium telluride photocathodes as an electron source for the Los Alamos Advanced FEL", Nucl. Instrum. Meth. A **358**, 284 (1995b).

Lee, H., X. Liu, L. Cultrera, B. Dunham, V. O. Kostroun and I. V. Bazarov, "A cryogenically cooled high voltage dc photoemission electron source", Rev. Sci. Instrum. **89**, 083303 (2018).

Li, W. H., C. J. R. Duncan, M. B. Andorf, A. C. Bartnik, E. Bianco, L. Cultrera, A. Galdi, M. Gordon, M. Kaemingk, C. A. Pennington, L. F. Kourkoutis, I. V. Bazarov and J. M. Maxson, "A kiloelectron-volt ultrafast electron micro-diffraction apparatus using low emittance semiconductor photocathodes", Structural Dynamics **9**, 024302 (2022).

Liu, F., L. Guo, J. DeFazio, V. Pavlenko, M. Yamamoto, N. A. Moody and H. Yamaguchi, "Photoemission from bialkali photocathodes through an atomically thin protection layer", ACS Appl. Mater. Inter. **14**, 1710 (2022).

Liu, F., N. A. Moody, K. L. Jensen, V. Pavlenko, C. W. N. Villarrubia, A. D. Mohite and G. Gupta, "Single layer graphene protective gas barrier for copper photocathodes", Appl. Phys. Lett. **110**, 041607 (2017).

Liu, Z. K., J. Jiang, B. Zhou, Z. J. Wang, Y. Zhang, H. M. Weng, D. Prabhakaran, S.-K. Mo, H. Peng, P. Dudin, T. Kim, M. Hoesch, Z. Fang, X. Dai, Z. X. Shen, D. L. Feng, Z. Hussain and Y. L. Chen, "A stable three-dimensional topological dirac semimetal Cd_3As_2", Nature Materials **13**, 667 (2014a).

Liu, Z. K., B. Zhou, Y. Zhang, Z. J. Wang, H. M. Weng, D. Prabhakaran, S.-K. Mo, Z. X. Shen, Z. Fang, X. Dai, Z. Hussain and Y. L. Chen, "Discovery of a three-dimensional topological dirac semimetal, Na_3Bi", Science **343**, 864 (2014b).

Lobastov, V. A., R. Srinivasan and A. H. Zewail, "Four-dimensional ultrafast electron microscopy", PNAS **102**, 7069 (2005).

Maxson, J. M., P. Musumeci, L. Cultrera, S. Karkare and H. A. Padmore, "Ultrafast laser pulse heating of metallic photocathodes and its contribution to intrinsic emittance", Nucl. Instrum. Meth. A **865**, 99 (2017).

Minitti, M. P., J. M. Budarz, A. Kirrander, J. S. Robinson, D. Ratner, T. J. Lane, D. Zhu, J. M. Glownia, M. Kozina, H. T. Lemke, M. Sikorski, Y. Feng, S. Nelson, K. Saita, B. Stanks, T. Northey, J. B. Hastings and P. M. Weber, "Imaging molecular motion: femtosecond x-ray scattering of an electrocyclic chemical reaction", Phys. Rev. Lett. **114**, 255501 (2015).

Musumeci, P., J. T. Moody, C. Scoby, M. S. Gutierrez, H. A. Bender and N. S. Wilcox, "High quality single shot diffraction patterns using ultrashort mega-electron volt electron beams from a radio frequency photoinjector", Rev. Sci. Instrum. **81**, 013306 (2010).

Musumeci, P., J. Navarro, J. az. Rosenzweig, L. Cultrera, I. Bazarov, J. Maxson, S. Karkare and H. Padmore, "Advances in bright electron sources", Nucl. Instrum. Meth. A **907**, 208 (2018).

Nangoi, J. K., S. Karkare, R. Sundararaman, H. A. Padmore and T. A. Arias, "Importance of bulk excitations and coherent electron-photon-phonon scattering in photoemission from PbTe(111): *Ab initio* theory with experimental comparisons", Phys. Rev. B **204**, 115132 (2021).

Pan, Z.-H., E. Vescovo, A. V. Fedorov, D. Gardner, Y. S. Lee, S. Chu, G. D. Gu and T. Valla, "Electronic structure of the topological insulator Bi_2Se_3 using angle-resolved photoemission spectroscopy: Evidence for a nearly full surface spin polarization", Phys. Rev. Lett. **106**, 257004 (2011).

Parzyck, C. T., A. Galdi, J. K. Nangoi, W. J. I. DeBenedetti, J. Balajka, B. D. Faeth, H. Paik, C. Hu, T. A. Arias, M. A. Hines, D. G. Schlom, K. M. Shen and J. M. Maxson, "Single-crystal alkali antimonide photocathodes: High efficiency in the ultrathin limit", Phys. Rev. Lett. **128**, 114801 (2022).

Pasmans, P. L. E. M., D. C. van Vugt, J. P. van Lieshout, G. J. H. Brussaard and O. J. Luiten, "Extreme regimes of femtosecond photoemission from a copper cathode in a DC electron gun", Phys. Rev. ST Accel. Beams **19**, 103403 (2016).

Perchec, J. L., P. Quémerais, A. Barbara and T. López-Ríos, "Why metallic surfaces with grooves a few nanometers deep and wide may strongly absorb visible light", Phys. Rev. Lett. **100**, 066408 (2008).

Pierce, C. M., J. K. Bae, A. Galdi, L. Cultrera, I. Bazarov and J. Maxson, "Beam brightness from Cs–Te near the photoemission threshold", Appl. Phys. Lett. **118**, 124101 (2021).

Polyakov, A., C. Senft, K. F. Thompson, J. Feng, S. Cabrini, P. J. Schuck and H. A. Padmore, "Plasmon-enhanced photocathode for high brightness and high repetition rate x-ray sources", Phys. Rev. Lett. **110**, 076802 (2013).

Rosenzweig, J. B., N. Majernik, R. R. Robles, G. Andonian, O. Camacho, A. Fukasawa, A. Kogar, G. Lawler, J. Miao, P. Musumeci, B. Naranjo, Y. Sakai, R. Candler, B. Pound, C. Pellegrini, C. Emma, A. Halavanau, J. Hastings, Z. Li, M. Nasr, S. Tantawi, P. Anisimov, B. Carlsten, F. Krawczyk, E. Simakov, L. Faillace, M. Ferrario, B. Spataro, S. Karkare, J. M. Maxson, Y. Ma, J. Wurtele, A. Murokh, A. Zholents, A. Cianchi, D. Cocco and S. B. van der Geer, "An ultra-compact x-ray free electron laser", New J. Phys. **22**, 093067 (2020).

Ruan, C.-Y., V. A. Lobastov, R. Srinivasan, B. M. Goodson, H. Ihee and A. H. Zewail, "Ultrafast diffraction and structural dynamics: The nature of complex molecules far from equilibrium", PNAS **98**, 7117 (2001).

Saha, P., O. Chubenko, G. Gevorkyan, A. Kachwala, C. Knill, C. Sarabia-Cardenas, E. Montgomery, S. Poddar, J. T. Paul, R. G. Hennig, H. A. Padmore and S. Karkare, "Physically and chemically smooth cesium-antimonide photocathodes on single crystal strontium titanate substrates", Appl. Phys. Lett. **120**, 194102 (2022).

Saha, P., O. Chubenko, J. K. Nangoi, T. Arias, E. Montgomery, S. Poddar, H. Padmore and S. Karkare, "Theory of photoemission from cathodes with disordered surfaces", J. Appl. Phys. **133**, 053102 (2023a).

Saha, P., A. Kachwala and S. Karkare, "Thermal limit to the mean transverse energies from alkali antimonide photocathodes", Manuscript under preparation (2023b).

Schmeißer, M. A. H., S. Mistry, H. Kirschner, S. Schubert, A. Jankowiak, T. Kamps and J. Kuhn, "Towards the operation of cs-k-sb photocathodes in superconducting rf photoinjectors", Phys. Rev. Accel. Beams ST **21**, 113401 (2018).

Schroeder, W. A. and G. Adhikari, "Evaluation of photocathode emission properties in an electron gun: one-step photoemission from bulk band to vacuum states", New J. Phys. **21**, 033040 (2019).

Sertore, D., S. Schreiber, K. Floettmann, F. Stephan, K. Zapfe and P. Micehlato, "First operation of cesium telluride photocathodes in the TTF injector rf gun", Nucl. Instrum. Meth. A **445**, 422 (2000).

Silva, N. R. D., M. Möller, A. Feist, H. Ulrichs, C. Ropers and S. Schäfer, "Nanoscale mapping of ultrafast magnetization dynamics with femtosecond lorentz microscopy", Phys. Rev. X **8**, 031052 (2018).

Siwick, B. J., J. R. Dweyer, R. E. Jordan and R. J. D. Miller, "Ultrafast electron optics: Propagation dynamics of femtosecond electron packets", J. Appl. Phys. **92**, 1643 (2002).

SLAC, "Annual laboratory plan", (2012).

Spicer, W. and A. Herrera-Gomez, "Modern theory and applications of photocathodes", Proc. SPIE Int. Soc. Opt. Eng: Photodetectors and Power Meters **2022**, 18 (1993).

Tian, Y., G. Gu, P. Johnson, T. Rao, T. Tsang and E. Wang, "Topological insulators for the generation of electron beams", App. Phys. Lett. **113**, 233504 (2018).

Vecchione, T., I. Ben-Zvi, D. H. Dowell, J. Feng, T. Rao, J. Smedley, W. Wan and H. A. Padmore, "A low emittance and high efficiency visible light photocathode for high brightness accelerator-based x-ray light sources", Appl. Phys. Lett. **99**, 034103 (2011).

Vecchione, T., D. Dowell, W. Wan, J. Feng and H. A. Padmore, "Quantum efficiency and transverse momentum from metals", Proceedings of FEL2013, Geneva, Switzerland p. 424 (2013).

Wilson, N. R., A. J. Marsden, M. Saghir, C. J. Bromley, R. Schaub, G. Costantini, T. W. White, C. Partridge, A. Barinov, P. Dudin, A. M. Sanchez, J. J. Mudd, M. Walker and G. R. Bell, "Weak mismatch epitaxy and structural feedback in graphne growth on copper foil", Nano. Res. **6(2)**, 99 (2013).

Xie, J., M. Demarteau, R. Wagner, S. Schubert, M. Gaowei, K. Attenkofer, J. Walsh, J. Smedley, J. Wong, J. Feng, H. Padmore, M. Ruiz-Oses, Z. Ding, X. Liang, E. Muller and I. Ben-Zvi, "Synchrotron x-ray study of a low roughness and high efficiency k2cssb photocathode during film growth", J. Phys. D: Appl. Phys. **50**, 205303 (2017).

Xu, C.-Z., Y.-H. Chan, Y. Chen, P. Chen, X. Wang, C. Dejoie, M.-H. Wong, J. A. Hlevyack, H. Ryu, H.-Y. Kee, N. Tamura, M.-Y. Chou, Z. Hussain, S.-K. Mo and T.-C. Chiang, "Elemental topological dirac semimetal: α-Sn on InSb(111)", Phys. Rev. Lett. **118**, 146402 (2017).

Yamaguchi, H., F. Liu, J. DeFaxio, M. Gaowei, C. W. N. Villarrubia, J. Xie, V. Pavlenko, K. L. Jensen, J. Smedley, A. D. Mohite and N. A. Moody, "Free-standing bialkali photocathodes using atomically thin substrates", Adv. Mater. Inter. **5**, 1800249 (2018).

Yamaguchi, H., F. Liu, J. DeFaxio, C. W. N. Villarrubia, D. Finkenstadt, A. Shabaev, K. L. Jensen, V. Pavlenko, M. Mehl, S. Lambrakos, G. Gupta, A. D. Mohite and N. A. Moody, "Active bialkali photocathodes on free-standing graphene substrates", npj 2D Mater. Appl. **1**, 12 (2017).

Zhong, Z., W. Gong, H. Jiang, H. Gu., X. Chen and S. Liu, "Investigation of spatial chirp induced by misalignments in a parallel grating pair pulse stretcher", Appl. Sci. **10(5)**, 1584 (2020).

APPENDIX A

DISCLAIMER

The work presented in Ch. 2 was originally published as Knill *et al.* (2023). The work presented in Ch. 3 and Ch. 4 are manuscripts that are currently under preparation with plans to submit them to a journal. For all three chapters I have obtained permission from all co-authors to use these works as chapters of my dissertation.